Non-Born-Oppenheimer Dynamics of Hydrogen Molecules in Strong Laser-Fields

Dissertation

zur Erlangung des akademischen Grades eines
Doktors der Naturwissenschaften (Dr. rer. nat.)
im Fachbereich Naturwissenschaften der Universität Kassel

vorgelegt von

Stefan Pieper

Tag der Disputation:
15. April 2009

Erstgutachter: Prof. Dr. Manfred Lein
Zweitgutachter: Prof. Dr. Martin Garcia

Contents

Introduction

The study of matter has been the most interesting and also one of the most important topics of physics ever since. Matter is what surrounds us all, matter is what we are made of. Matter, that is—basically—atoms and molecules in terms of our modern understanding. Composed of (partially) charged quantum particles with different masses. Their Coulomb interactions define stable compositions of atoms. They also define the stability of chemical bonds and hence of molecules. Therefore, the interactions also define the possibilities and outcomes of chemical reactions. And with this, the interactions of the constituents of matter define practically everything from simple atoms to complex organisms in our world. What starts as quantum physics, quickly leads to atomic and molecular physics, quantum chemistry, reaction dynamics and chemical equilibria, biochemistry, cells, organisms, and life.

All this can be further influenced from "outside", i.e., by different conditions like temperature, electromagnetic fields of static or oscillating character of arbitrary frequency and even by Coulomb interaction with additional particles. Usually, most interesting are manipulations from outside directly influencing the Coulomb interactions between the matter constituents. Since scattering processes with particles usually involve large accelerator machines, this technique is usually applied in the area of high-energy physics. Also, not as many parameters as in the case of laser systems are accessible. This technique is mainly used for investigations of *nuclear* structure. Static fields influence the level structure of atoms and allow for the analysis of symmetries and degeneracies of electronic states.

Oscillating continuous-wave laser fields instead correspond to mono-energetic photons. These directly interact with the charged particles depositing energy there. Parameters like frequency and phase, polarisation and to a certain extent intensity of the laser light can be controlled in today's labs in a very accurate way. Also, today's laser systems are strong enough in terms of intensity to ionise atoms even in the low-frequency regime, where many photons are needed to deposit enough energy for ionisation events to take place.

If the laser is pulsed, it can be used to investigate the nuclear dynamics of molecules, since ionisation at different configurations of nuclear positions will lead to different Coulomb repulsions if the system is forced to dissociate. The picture of the laser pulse is that of a shutter from a camera. The shorter the pulse, the higher the temporal resolution of the dynamics of the investigated system. All this is only possible because in pulsing the laser, the energy is concentrated in very short instances, while the laser is otherwise dark most of the time. With this technique, electric fields strengths comparable to those found in atomic hydrogen can be produced! This means, the laser is

able to compete in field strength with what is found inside the system itself. The laser is no perturbation any more, but acts on an equal footing upon electrons and protons.

To avoid handling with unsuitable units, the *atomic units* have been introduced, scaling the physical quantities to values found in atoms and molecules. This is not only useful for comparisons of (external) quantities with those found in the system itself, but also allows one to work with numbers of the order of unity, which is always important when delegating work to computers. The scales are defined as the following:

- Masses are measured in multiples of the electron mass, i.e., $m_e = 1$.
- Actions are measured in multiples of $\hbar$, i.e., $\hbar = 1$.
- Charge is scaled with the elementary charge, i.e., $|e| = 1$.
- As four scales are needed, finally the electric permittivity is scaled as $4\pi\epsilon_0 = 1$.

This leads to values for the speed of light of $c = 1/\alpha$ in atomic units, where α is Sommerfeld's fine-structure constant. The charge of the electron is $e_0 = -1$. One length unit corresponds to the radius of the first Bohr orbit $a_0 = 0.529177 \times 10^{-10}$m. Energy is measured in units of one Hartree, which is twice the energy of the first Bohr level in atomic hydrogen, i.e., 1 Hartree= 27.2114 eV. Basically, everything is scaled according to what is found in atomic hydrogen. This gives a good estimate of how large a physical quantity really is in atomic dimensions. From now on, all formulae and expressions will be given in atomic units. In particular, no $\hbar$ will appear where it usually would. No masses will appear, where electron masses usually would. Electron charges manifest as minus signs only. This may lead to some confusion first, since the dimensions of two sides of the same equation seem not to match. After getting used to it, life is much easier.

With this at hand, we are able to investigate the intrinsic motion of matter (e.g., nuclear vibration). As pulses get shorter, reaching the femto-second timescale, and stronger ($\lesssim 1$ a.u. of field amplitude), more and more interesting effects can be observed, leading to a detailed understanding of electronic behaviour and electro-nuclear interaction. In field-ionisation of atoms, electrons can be promoted directly into the continuum, they can be driven back to the ionic core and re-scatter elastically or inelastically, or even not re-scatter at all. Re-scattering inelastically, they can excite or even knock out further electrons. This strongly enhances the double-ionisation rates. They can also recombine, sending out high-harmonic radiation up to very high order. Simple theoretical models such as Franck-Condon factors or ionisation rates can be scrutinised. Nowadays, where even attosecond laser pulses can be generated, the timescale of electronic motion is reached. It is in principle possible now to investigate moving electrons. This is surely the most important missing piece for a full understanding of the intrinsic dynamics of matter.

All these processes exist in molecules, too, but are harder to explore since more degrees of freedom are involved into the dynamics. Molecular alignment is the first hurdle to be taken when the laser polarisation direction is important. For linear molecules, this is usually not a problem, since they can be aligned in strong laser fields, and the rotational periods are orders of magnitude longer than electronic or nuclear motion,

which are mainly studied within those systems nowadays and are also the main topic of this work.

The simplest molecule we have is that composed of two hydrogen atoms, H_2. Two electrons, two protons. A mononuclear, linear, lightweight system with vibrating nuclei.[1] This introduces exactly one additional degree of freedom to a purely electronic system, namely the vibrational motion of the nuclei along the inter-nuclear axis. This motion is of course coupled to the electronic motion, and energy is transferred back and forth between these two very different dynamics. This is exactly the point of observation of this thesis.

Usually, the motions of electrons and nuclei are treated separately. This stems from the fact that the nuclear motion is *much* slower than the electronic motion. Hence, from the viewpoint of an electron, the situation it finds itself in changes only adiabatically. This can be compared to a fly whirring around a snail. The rotation of the earth could stand for the rotation of a molecule in this picture. The *separation of scales* is a very powerful tool of theoretical physics to isolate parts of a system that only weakly influence each other. Since this approach assumes adiabatic assimilation of the electron to each new situation, i.e., each new configuration of ionic cores, it only works as long as the electron does not undergo excitations or, even worse, ionisation. Because then state transitions would come up, whereas in the adiabatic picture, the electronic state *changes* according to the changes outside, but the population stays constant and *follows* the deformation. For very strong laser fields this is surely not the case. Therefore, we have to give up what is called the famous *Born-Oppenheimer Approximation*, explained in detail within the first chapter of this work.

If the laser field strength is modest, i.e., small compared to inner-atomic or inner-molecular field strengths, in can be treated as a perturbation to the system. The system without laser field is solved and corrections are calculated under the influence of a perturbative laser field. We certainly don't reside in this regime. The laser fields treated within this work are *non-perturbative*. For *extremely strong* laser fields, the atomic or molecular Coulomb potential can be treated as a perturbation to a free electron in a laser field. This is also not possible here, since such high laser field strengths would immediately destroy the system under investigation, which is not of interest either within the scope of this work.

For the case where there is no possibility to distinguish between a *system* and a *perturbation*, where excitation and ionisation will take place, and where the coupling between electronic and nuclear motion is to be studied, there is no other way of obtaining reasonable results than to start at the very basics and integrate the Time-Dependent Schrödinger Equation. Only these *ab-initio* calculations allow for a thorough investigation of the system, since everything not explicitly excluded from the simulation (like complicated details of interactions, spin, magnetic fields) will be contained in the final results. The result of the calculation is a wave function, containing all the information possible to obtain for a quantum system. This procedure will be explained in detail in the second chapter of this work.

A focus is laid upon single ionisation of H_2 and D_2. Therefore, to not lose any data, extremely large extensions of the computational grid are needed in the direction of elec-

[1] Rotation is not taken into account, since we assume aligned molecules from now on.

tronic motion. A special technique is applied for this. In detail, spectral enhancements within the kinetic-energy spectra of photo-electrons due to a change in the effective ionisation threshold are examined. The effect is known from atoms and already deeply investigated, experimentally as well as theoretically. The same effect is presented for small molecules, involving the nuclear degree of freedom and therefore avoiding the need to change the laser intensity to observe the effect. The findings are put in context with electro-nuclear correlations also found within the data. On this topic, two articles [1, 2] have been published together with Manfred Lein. All this is presented in the third chapter of this work.

Finally, a way to optimise kinetic-energy spectra is presented. It takes the Coulomb energy of photo electrons into account, which is usually neglected in the Fourier method. It could be shown that, for low-energy electrons, the error is substantial and therefore the corresponding kinetic-energy peaks are significantly shifted. The key idea is to make use of the Wigner distribution function instead of simple Fourier transformations, which yields position-resolved spectra and hence allows for position-dependent Coulomb corrections. This can be found in the fourth and last chapter of this work.

Zusammenfassung

Die vorliegende Arbeit befasst sich mit der theoretischen, rechnergestützten Beschreibung des Wasserstoffmoleküls H_2 und seines schweren Bruders, dem Deuteriummolekül D_2 in kurzen, starken Laserfeldern. Da im Bereich von Laserfeldern, deren Kräfte auf die Elektronen in der gleichen Liga wie die der inneratomaren Kräfte spielen, Näherungsmethoden nicht mehr greifen, wird in dieser Arbeit eine (allerdings stark vereinfachte) zweidimensionale Schrödingergleichung numerisch integriert. Dabei wird im Rahmen der Einfachionisation besonderes Augenmerk auf den Prozess der *above threshold ionisation* (ATI) gelegt, d.h. der Ionisation unter Absorbtion von mehr Photonen als nötig, um die Ionisationsbarriere zu überschreiten. Dabei entstehen charakteristische Energiespektren des Photoelektrons, deren Struktur interessante Abhängigkeiten von der Laserintensität zeigt.

Das erste Kapitel behandelt die im Bereich der Molekülphysik sonst häufig bemühte Born-Oppenheimer-Näherung, die allerdings im vorliegenden Falle nicht geeignet ist, da durch die Induzierung mannigfaltiger nichtlinearer Prozesse bis hin zur Ionisation von einer Separation von Elektron- und Kernbewegung abgesehen werden muss, da adiabatische Bewegung nicht mehr gegeben ist.

Im zweiten Kapitel werden die verwendeten numerischen Methoden vorgestellt. Dabei wird das Wasserstoffmolekül durch einen effektiven, eindimensional vibrierenden $H_2{}^+$-Rumpf und ein aktives, eindimensionales Elektron modelliert. Um Energiespektren hoher Güte zu erhalten, wurde eine Splittingtechnik benutzt, bei der die Wellenfunktion für Bereiche großer Elektronkoordinaten in spezielle Produktzustände, die sogenannte kanonische Basis, entwickelt wird. Dadurch kann in diesem äußeren Gitterbereich entkoppelt und für jede Koordinate separat eindimensional gerechnet werden. Das ermöglicht eine deutlich höhere Anzahl von Gitterpunkten in Richtung der Elektronkoordinate, was wiederum hohe spektrale Auflösung sowie vernachlässigbaren Datenverlust in Bezug auf die Energiespektren bedeutet.

Ein im Bereich der Einfachionisation von Atomen beobachteter Effekt, der eine deutliche Erhöhung der Ausbeute von gestreuten Elektronen vorhersagt, wenn die Laserintensität bestimmte Werte annimmt, wird im Dritten Kapitel für das Wasserstoffmolekül nachgewiesen. Der Effekt beruht auf der Abhängigkeit des Ponderomotivpotentials von der Laserintensität und somit einer variablen effektiven Ionisationsschwelle. Es konnte gezeigt werden, dass dieser Effekt für den Fall von Mokekülen, die durch die Kernvibration eine zweite, intrinsische Energieskala bereitstellen, zu beobachten ist, *ohne* die Laserintensität zu variieren. Die effektive Ionisationsschwelle hängt hier vom Vibrationsniveau des produzierten Ions ab, so dass bei Separation der Energiespektren in Bezug auf die Vibrationsniveaus des produzierten Ions der gleiche Effekt intrinsisch

beobachtet werden kann. Er entspricht qualitativ den Erwartungen, weicht quantitativ jedoch von dem einfachen Mechanismus der Energieerhaltung ab, der bemüht wurde, um die Vorgänge anschaulich zu beschreiben. Dies ist von dem atomaren Pendant her bekannt. Der durchgeführte Vergleich zwischen Wasserstoff und Deuterium entspricht jedoch auch quantitativ den Erwartungen. Die Resultate dieser Rechnungen konnten in zwei Artikeln publiziert werden [1, 2]. Schließlich wurde versucht, die Korrelation von Elektron und Ion quantitativ zu untersuchen. Ein in der Fachliteratur bereits vorgeschlagenes Maß für diese Größe wurde im Impulsraum impulsaufgelöst berechnet. Dabei konnte eine deutliche Struktur indentifiziert werden, deren genauer Ursprung aber Spekulation bleiben muss.

Im letzten Kapitel wurde eine neue Methode untersucht, Energiespektren von Photoelektronen zu berechnen. Das übliche Problem besteht darin, dass wesentliche Teile der Wellenfunktion sich zum Zeitpunkt der Berechnung des Spektrums noch in Raumgebieten befinden, wo das Coulombpotential des Ions wesentlich von Null verschieden ist. Durch diesen Umstand werden die Energien solcher Elektronen systematisch überschätzt, wenn man lediglich die Fourieranalyse bemüht, da sie auf den Weg zu einem Detektor weiter Energie verlieren würden, liefen sie den Coulomb-Berg weiter hinauf. Der übliche Weg aus dieser Misere besteht darin, die Elektronen weiter auswärts propagieren zu lassen, was längere Simulationszeiten sowie noch größere Gitter bedeutet. Es ist jedoch möglich, die ortsabhängige Coulombenergie korrigierend abzuziehen, indem man die Impulse der Elektronen ortsaufgelöst über die Wignerfunktion berechnet. Aus den auf diesem Wege korrigierten effektiven Impulsen können dann korrigierte Energiespektren berechnet werden, die es erlauben, auch Elektronen korrekt spektral zu erfassen, die sich noch sehr nah am Ion befinden. Die Qualität dieser Spektren ist erstaunlich gut und entspricht in den entsprechenden Bereichen quantitativ den erwarteten Abweichungen zu herkömmlichen, dort fehlerbehafteten Fourier-Spektren.

Chapter 1

The starting point

In the beginning there was nothing but a very complicated Schrödinger Equation,

$$i\hbar\frac{\partial}{\partial t}|\psi\rangle = \widehat{H}|\psi\rangle. \tag{1.1}$$

This holds for almost everything appearing in nature[1], even for simple molecules. The best solver of Time-(In-)Dependent Schrödinger Equations is nature itself. But since the "description" of a system nature gives us at hand is just the realization itself, this does not help us in understanding the laws of motion and interaction valid under certain aspects of life. Therefore we have to introduce simplifications if possible to extract the very core of a certain problem or system under consideration. Helpful tools in this aspect are the separation of energy scales, the reduction of dimensionality, or the approximative decoupling of weakly interacting parts of the system.

Still doing all of this might not be enough in certain cases to thoroughly describe a quantum system. Experiments have to be done to confirm expectations. But as always, certain experiments are either not (yet) feasible or just not promising enough to justify the effort needed to obtain results. This is where an important intermediate step comes into play: Numerical simulation. In fact, a numerical simulation is, in some sense, an experiment. If there is no chance for a closed calculation, one can only fall back on general rules of behaviour and laws of nature. What one does is to prepare the initial state of the system and to watch it evolve in time under the influence of the prescribed laws and rules and interactions, i.e., to solve the Time Dependent Schrödinger Equation. Certain kinds of "measurements" are taken out at the end or during the simulation of the system which allow us to extract information about the characteristics of the system under consideration. All this is basically identical to what is done in a laboratory. The only differences are the limited dimensionality of a simulation, the discreteness of the numbers on a computer and the simplifications used. On the winning side, the "experiment" is dramatically cheaper and simpler. It can also be redone arbitrarily many times without big effort, it will always keep its accuracy and one can strongly expect a speedup of the simulation in the future, since computers usually obey an exponentially increasing power with time. Of course all this only holds as long as all components of the system and its influences upon each other are known. The result

[1] as long as only mid-energy physics are considered and spin is not important

of their interplay is then given by the calculation. One must not leave out important physics within the simulation, otherwise it will not reflect what really happens in a real system. What *is* important, has to be investigated carefully. But this is also valid for every real experiment, where not everything can be measured, where the system can necessarily not be completely decoupled from the environment and where systematic errors may as well occur as statistical ones. The demands are different but high in both worlds.

The first chapter deals with the Born-Oppenheimer Approximation. It will be introduced in detail and discussed in terms of its limitations. In the end it will come out that for H_2, within this work, one has to go beyond the Born-Oppenheimer approximation. It will however be employed for $H_2{}^+$, calculating an effective nuclear repulsion and vibrational states of the molecular ion. The intention of this introductory chapter is to understand why this approximation does not suit our needs for the full calculation.c This is important since the Born-Oppenheimer approximation is a legitimate and powerful tool in theoretical molecular physics, and vastly used in quantum chemistry as well.

1.1 The Born-Oppenheimer Approximation

The following illustration of the Born-Oppenheimer approximation follows closely [3] and [4]. The Born-Oppenheimer (BO) approximation was first introduced by Born and Oppenheimer in 1927. It is ubiquitous in quantum chemical calculations[2] of molecular wave functions and was also frequently used for quantum molecular calculations in physics ever since its appearance. It will be applied to a molecular system described by the Time-Independent Schrödinger Equation (TISE)

$$H\Psi(\mathbf{r},\mathbf{R}) = E\Psi(\mathbf{r},\mathbf{R}), \tag{1.2}$$

where $\mathbf{r}$ and $\mathbf{R}$ denote all electronic and nuclear coordinates, respectively. It consists of two steps. In the first step the nuclear kinetic energy is neglected, that is, the corresponding operator T_n is subtracted from the total molecular Hamiltonian

$$H(\mathbf{r},\mathbf{R}) = T_n(\mathbf{R}) + \underbrace{T_\mathrm{e}(\mathbf{r}) + V_\mathrm{n}(\mathbf{R}) + V_\mathrm{e}(\mathbf{r}) + V_\mathrm{en}(\mathbf{r},\mathbf{R})}_{H_\mathrm{e}(\mathbf{r};\mathbf{R})}. \tag{1.3}$$

In the remaining electronic Hamiltonian $H_\mathrm{e}(\mathbf{r};\mathbf{R})$, containing the electronic kinetic energy operator, and the potentials describing inter-electronic, inter-nuclear and electron-nuclear interactions, the nuclear positions $\mathbf{R}$ enter only as parameters and represent no dynamic variables any more. The electron-nucleus interactions are not removed and the electrons still "feel" the Coulomb potential of the nuclei clamped at certain positions in space. (This first step of the BO approximation is therefore often referred to as the clamped nuclei approximation.) The electronic Schrödinger equation

$$H_\mathrm{e}(\mathbf{r};\mathbf{R})\phi(\mathbf{r};\mathbf{R}) = E_\mathrm{e}(\mathbf{R})\phi(\mathbf{r};\mathbf{R}) \tag{1.4}$$

[2] By this, calculations involving a rather large number of atoms are meant.

is solved (out of necessity approximately) with a fixed nuclear geometry as input. Obviously, the electronic energy eigenvalue E_e depends on the chosen positions $\mathbf{R}$ of the nuclei. Varying these positions $\mathbf{R}$ in small steps and repeatedly solving the electronic Schrödinger equation, one obtains $E_\mathrm{e}(\mathbf{R})$ being called the potential energy surface (PES) of the system. Because this procedure of recomputing the electronic wave functions as a function of an infinitesimally changing nuclear geometry is reminiscent of the conditions for the adiabatic theorem [5], this manner of obtaining a PES is often referred to as the adiabatic approximation, and the PES itself is called an adiabatic surface.[3]

In the second step of the BO approximation the nuclear kinetic energy $T_\mathrm{n}(\mathbf{R})$ (containing partial derivatives with respect to the components of $\mathbf{R}$) is reintroduced and the Schrödinger equation for the nuclear motion

$$[T_\mathrm{n}(\mathbf{R}) + E_\mathrm{e}(\mathbf{R})]\,\chi(\mathbf{R}) = E\,\chi(\mathbf{R}), \tag{1.5}$$

containing the electronic energies $E_e(\mathbf{R})$ obtained before, is solved. This second step of the BO approximation involves separation of vibrational and rotational motion. The real number E is the total energy of the molecule, including contributions from electrons, nuclear vibrations, and rotations.

It will be discussed how the BO approximation may be derived and under which conditions it is applicable. At the same time we will show how the BO approximation may be improved by including vibronic coupling. To that end the second step of the BO approximation is generalised to a set of coupled eigenvalue equations depending on nuclear coordinates only. Off-diagonal elements in these equations are shown to be nuclear kinetic energy terms. It will be shown that the BO approximation can be trusted whenever the PESs, obtained from the solution of the electronic Schrödinger equation, are well separated: $E_0(\mathbf{R}) \ll E_1(\mathbf{R}) \ll E_2(\mathbf{R}), \ldots$ for all $\mathbf{R}$. We start from the exact time-independent molecular Hamiltonian,

$$H(\mathbf{r}, \mathbf{R}) = H_\mathrm{e}(\mathbf{r}; \mathbf{R}) + T_\mathrm{n}(\mathbf{R}), \tag{1.6}$$

where in general

$$H_\mathrm{e}(\mathbf{r}; \mathbf{R}) = -\sum_i \frac{\hbar^2}{2m_e}\Delta_i - \sum_{i,A} \frac{Z_A}{r_{iA}} + \sum_{i>j} \frac{1}{r_{ij}} + \sum_{A>B} \frac{Z_A Z_B}{R_{AB}} \tag{1.7}$$

and

$$T_\mathrm{n} = -\sum_A \frac{\hbar^2}{2M_A}\Delta_A. \tag{1.8}$$

The position vectors $\mathbf{r} \equiv \{\mathbf{r}_i\}$ of the electrons and the position vectors $\mathbf{R} \equiv \{\mathbf{R}_A = (R_{Ax},\, R_{Ay},\, R_{Az})\}$ of the nuclei are with respect to a Cartesian inertial frame. Distances between particles are written as $r_{iA} \equiv |\mathbf{r}_i - \mathbf{R}_A|$ (distance between electron i and nucleus A) and similar definitions hold for r_{ij} and R_{AB}. The constants explicitly entering the

[3] It is assumed, in accordance with the adiabatic theorem, that the same electronic state (for instance the electronic ground state) is obtained upon small changes of the nuclear geometry, i.e., small changes in the potential make the system follow the changes without populating other states. The method could give a non-continuous PES if electronic state-switching would occur.

formula are Z_A and M_A, the atomic number and charge of nucleus A, the electron mass m_e, and Planck's constant $\hbar$. It is useful to rewrite the nuclear kinetic energy operator as follows:

$$T_{\rm n} = \sum_A \sum_{\alpha=x,y,z} \frac{P_{A\alpha}^2}{2M_A} \quad \text{with} \quad P_{A\alpha} = -i\hbar \frac{\partial}{\partial R_{A\alpha}}. \tag{1.9}$$

Suppose we have K electronic eigenfunctions $\phi_k(\mathbf{r};\mathbf{R})$ of $H_{\rm e}(\mathbf{r};\mathbf{R})$, that is, we have solved

$$H_{\rm e}(\mathbf{r};\mathbf{R})\phi_k(\mathbf{r};\mathbf{R}) = E_k(\mathbf{R})\phi_k(\mathbf{r};\mathbf{R}) \quad \text{for} \quad k = 1,\ldots,K. \tag{1.10}$$

The electronic wave functions $\phi_k(\mathbf{r};\mathbf{R})$ will be taken to be real, which is possible when there are no magnetic or spin interactions. The parametric dependence of the functions $\phi_k(\mathbf{r};\mathbf{R})$ on the nuclear coordinates is indicated by the $\mathbf{R}$ symbol after the semicolon. This indicates that, although $\phi_k(\mathbf{r};\mathbf{R})$ is a real-valued function of $\mathbf{r}$, its functional form depends on $\mathbf{R}$. We will assume that the parametric dependence is continuous and differentiable, so that it is meaningful to consider

$$P_{A\alpha}\phi_k(\mathbf{r};\mathbf{R}) = -i\hbar \frac{\partial \phi_k(\mathbf{r};\mathbf{R})}{\partial R_{A\alpha}} \quad \text{for} \quad \alpha = x,y,z, \tag{1.11}$$

which in general will not be zero. The total wave function $\Psi(\mathbf{r},\mathbf{R})$ is expanded in terms of $\phi_k(\mathbf{r};\mathbf{R})$,

$$\Psi(\mathbf{r},\mathbf{R}) = \sum_{k=1}^{K} \chi_k(\mathbf{R})\phi_k(\mathbf{r};\mathbf{R}), \tag{1.12}$$

with

$$\langle\, \phi_{k'}(\mathbf{r};\mathbf{R}) \,|\, \phi_k(\mathbf{r};\mathbf{R})\rangle_{(\mathbf{r})} = \delta_{k'k} \tag{1.13}$$

and where the subscript $(\mathbf{r})$ indicates that the integration, implied by the bra-ket notation, is over electronic coordinates only. The expansion coefficients $\chi_k(\mathbf{R})$, suggestively already looking like wave functions, only depend on $\mathbf{R}$ and can be interpreted as nuclear wave functions.

After multiplication by $\phi_{k'}^*(\mathbf{r};\mathbf{R})$ from the left and integration over the electronic coordinates $\mathbf{r}$, the total Schrödinger equation (1.2) is turned into a set of K coupled eigenvalue equations depending on nuclear coordinates only,

$$[\mathbb{H}_{\rm n}(\mathbf{R}) + \mathbb{H}_{\rm e}(\mathbf{R})]\,\boldsymbol{\chi}(\mathbf{R}) = E\boldsymbol{\chi}(\mathbf{R}), \tag{1.14}$$

where, by definition, the matrix with general element

$$\big(\mathbb{H}_{\rm e}(\mathbf{R})\big)_{k'k} \equiv \langle \phi_{k'}(\mathbf{r};\mathbf{R})|H_{\rm e}|\phi_k(\mathbf{r};\mathbf{R})\rangle_{(\mathbf{r})} = \delta_{k'k}E_k(\mathbf{R}) \tag{1.15}$$

is diagonal. The column vector $\boldsymbol{\chi}(\mathbf{R})$ has elements $\chi_k(\mathbf{R})$, $k = 1,\ldots,K$. The nuclear Hamilton matrix $\mathbb{H}_{\rm n}(\mathbf{R})$ is non-diagonal with the following off-diagonal (vibronic coupling) terms,

$$\big(\mathbb{H}_{\rm n}(\mathbf{R})\big)_{k'k} = \langle \phi_{k'}(\mathbf{r};\mathbf{R})|\, T_{\rm n}\, |\phi_k(\mathbf{r};\mathbf{R})\rangle_{(\mathbf{r})}. \tag{1.16}$$

The vibronic coupling in this approach is through nuclear kinetic energy terms. Solution of these coupled equations gives an approximation for energy and wave function that goes beyond the BO approximation. Unfortunately, the off-diagonal kinetic energy

terms are usually difficult to handle. (This is why often a diabatic transformation is applied, which retains part of the nuclear kinetic energy terms on the diagonal, removes the kinetic energy terms from the off-diagonal and creates coupling terms between the adiabatic PESs on the off-diagonal.)

If we can neglect the off-diagonal elements the equations will uncouple and simplify drastically. In order to show when this neglect is justified, we write, leaving out functional arguments, by applying the Leibniz rule for differentiation, the matrix elements of T_n as

$$H_\mathrm{n}(\mathbf{R})_{k'k} \equiv \left(\mathbb{H}_\mathrm{n}(\mathbf{R})\right)_{k'k} = \delta_{k'k} T_\mathrm{n} + 2\sum_{A,\alpha} \frac{\hbar^2}{2M_A} \langle \phi_{k'} | P_{A\alpha} \phi_k \rangle_{(\mathbf{r})} P_{A\alpha} + \langle \phi_{k'} | T_\mathrm{n} \phi_k \rangle_{(\mathbf{r})}. \tag{1.17}$$

The diagonal ($k' = k$) matrix elements $\langle \phi_k | P_{A\alpha} \phi_k \rangle_{(\mathbf{r})}$ of the operator $P_{A\alpha}$ vanish, because this operator is Hermitian and purely imaginary. The off-diagonal matrix elements satisfy

$$\langle \phi_{k'} | P_{A\alpha} \phi_k \rangle_{(\mathbf{r})} = \frac{\langle \phi_{k'} | [P_{A\alpha}, H_\mathrm{e}] | \phi_k \rangle_{(\mathbf{r})}}{E_k(\mathbf{R}) - E_{k'}(\mathbf{R})}. \tag{1.18}$$

The matrix element in the numerator is

$$\langle \phi_{k'} | [P_{A\alpha}, H_\mathrm{e}] | \phi_k \rangle_{(\mathbf{r})} = i\hbar Z_A \sum_i \left\langle \phi_{k'} \middle| \tfrac{(\mathbf{r}_{iA})_\alpha}{r_{iA}^3} \middle| \phi_k \right\rangle_{(\mathbf{r})} \quad \text{with} \quad \mathbf{r}_{iA} \equiv \mathbf{r}_i - \mathbf{R}_A. \tag{1.19}$$

The matrix element of the one-electron operator appearing on the right hand side is finite. When the two surfaces come close, $E_k(\mathbf{R}) \approx E_{k'}(\mathbf{R})$, the nuclear momentum coupling term becomes large and is no longer negligible. This is the case where the BO approximation breaks down and a coupled set of nuclear motion equations must be considered, instead of the one equation appearing in the second step of the BO approximation. Conversely, if all surfaces are well separated, all off-diagonal terms can be neglected and hence the whole matrix of P_α^A is effectively zero. The third term on the right hand side of Eq. 1.17 can approximately be written as the matrix of P_α^A squared and, accordingly, is then negligible also. Only the first (diagonal) kinetic energy term in this equation survives in the case of well-separated surfaces and a diagonal, uncoupled set of nuclear motion equations results,

$$\left[T_\mathrm{n}(\mathbf{R}) + E_k(\mathbf{R})\right] \chi_k(\mathbf{R}) = E\chi_k(\mathbf{R}) \quad \text{for} \quad k = 1, \ldots, K, \tag{1.20}$$

which are the normal second-step of the BO equations discussed above. We reiterate that when two or more potential energy surfaces approach each other, or even cross, the BO approximation breaks down and one must fall back on the coupled equations.

1.2 Going Beyond the Born-Oppenheimer Approximation

Calculations of molecules involving the Born-Oppenheimer approximation usually (details follow) yield quite reasonable results, but of course the validity of every approximation is limited. In section 1.1, the BO approximation was introduced and also its

limitations were pointed out: As soon as two or more coupling[4] PES (i.e., total potential energy surfaces as functions of the nuclear positions for different electronic states) of the system in question closely approach each other, or even cross, the adiabatic picture is no longer valid. Electrons do not just follow the moving nuclei adiabatically, but instead may change their state into other levels, without changing the nuclear configuration. When the electrons are strongly driven from outside, the potential curves are significantly bent and it may easily happen that for some nuclear distance the ignored energy corrections stemming from the electro-nuclear coupling exceed the energy gaps between neighbouring PESs. As soon as ionisation plays a role, the BO approximation is definitely over-challenged. In the situation of this work, where the connection between strong-field single ionisation and nuclear motion shall be investigated, a different approach has to be taken.

In our case, a laser electric field drives the electron(s). For simplicity we start our considerations with a single-mode laser of infinite pulse duration, i.e., a continuous wave (CW), and frequency ω_L. The dressed-states picture can help understanding the situation. Now, the electric field is treated quantum-mechanically, and due to the limitations set upon the laser field, all photons have the same energy $\hbar\omega_L$. Each electronic state can now be "dressed" with photons, i.e., electrons can absorb photons from the laser. This rises the energy $E_e(\mathbf{R})$ an electron can have by some integer multiple of the photon energy $\hbar\omega_L$ to $E_e(\mathbf{R}) + n\hbar\omega_L$. Transferred into the PES picture, this means that each PES has to be repeated n times, shifted by $\hbar\omega_L$ respectively. This way, otherwise well distinct PESs are now able to approach or even cross each other, this being introduced by a sufficiently strong laser field. Correction terms can grow large in these cases. Non-adiabatic motion in induced. In this situation, the BO approximation may reach its limits. Depending on the intensity of the laser, the probability to absorb many photons can be quite large. Hence even for photon energies *well below* the gap of two PESs an intense field is still able to couple these two states by absorption of many photons.

In the present situation of this work, the intensity of the laser is strong enough to reliably treat the laser electric field completely classically. This fact is associated with a high photon density. Hence, even for well-separated PESs as is the case for the hydrogen molecular ion, multi-photon effects can easily induce transitions between ground and first excited state. For the H_2^+ ion this already means dissociation. In fact, the interplay of avoided crossings and their dynamics due to the oscillating laser field leads to important effects in H_2^+ like bond-hardening, bond-softening etc. Bond-softening is the complex interplay of avoided multiphoton crossings and nuclear wave packet dynamics in the course of an oscillating laser field. Due to changing avoided crossings of PESs during a laser cycle, the nuclear wave packet can under certain conditions easily travel onto a dissociating PES at one time, there being further accelerated towards larger R at a later time, finally dissociating. This interplay leads to unexpectedly strong dissociation dynamics and is therefore referred to as *bond-softening* [6, 7]. This periodic mechanism is akin to a conventional pump. Bond-hardening on the other hand comes up when due to an avoided crossing a potential well builds up, gathering part of an

[4]Because with the absorption of every photon the parity of the molecular state has to change, the coupling depends on the number of photons needed for the transition and the symmetry of the states in question.

otherwise dissociating wave packet as some vibrationally excited state, which is later released back into a bound state. This way, dissociation is diminished. This process of vibrational trapping is also referred to as *bond hardening*[8, 6, 7].

Yet it is possible to diminish couplings between PESs induced by strong laser fields via choosing specific polarisations, such that the corresponding dipole does not mediate between the states in question.

If it is not advisable to make use of the BO approximation, one has to go beyond it. This means we have to take direct interactions between electrons and nuclei into account. Further common approximations like perturbation theory do not apply here as well, since the forces of the laser field upon electron compete with the inner-molecular forces on equal level.

For monochromatic laser light, the Floquet theory [9] is a good access to the system. Due to the strict periodicity of the laser field and hence the time dependence of the Hamiltonian, the restrictions on the wave functions are quite strong. For example, they can be written as a product of a plane wave and a time-periodic amplitude, which will obey the same periodicity as the laser field. The formalism is similar to the Bloch formalism for space-periodic potentials.

Even if the laser is pulsed, in the case of adiabatic pulse ramps one can make use of the Floquet picture, in combination with the adiabatic theorem [10]. If the laser pulse is long compared to the laser period, and the pulse envelope is rather flat, i.e., it goes on and off slowly compared to the laser frequency, another separation of scales is possible. The Floquet picture is possible even then through separation of time scales. The fast oscillation and the slow envelope of the laser are treated separately and the system can be solved as in the Floquet picture, with the second time scale treated parametrically.

Still, none of the above-mentioned techniques will suffice, since the laser fields within this work are comparably strong (no perturbation), the pulses are comparably short and hence the envelopes are steep (no adiabatic Floquet). The spectrum is comparably broad and hence neither monochromaticity nor adiabaticity of the laser pulse can be assumed. Energy scales lie close, time scales lie close. The full interaction has to be taken into account. Therefore, the only way to gain access to the system under consideration is via solving the TDSE explicitly. Of course, simplifications will have to be introduced since a four-partite molecule in a laser field cannot be fully treated even today in full dimensionality. These aspects will be addressed in the following chapter.

Chapter 2

Numerics

This chapter contains sections about the numerical techniques used to obtain the presented results. Examined is single ionisation of the hydrogen and deuterium molecules. As the previous chapter clearly pointed out, none of the usual approximations can be made to analytically investigate the systems(s) considered. We have to go back to the very basis of Quantum Mechanics, i.e., basically all data is produced by solving the Time Dependent Schrödinger Equation (TDSE). This is done on a 2D grid, representing one electronic and one nuclear degree of freedom. Obviously, this is a severe simplification. Nevertheless, the model is capable of yielding definite effects. Since 3D calculations are computationally still demanding, especially if the electronic motion stretches out over several thousands of atomic units, for a first investigation of molecular channel closing effects calculations with reduced dimensionality suffice our needs.

First of all the properties of the grid are discussed. Propagation schemes follow, continued by a detailed explanation of how parts of the wave function are extracted for further analysis. A grid splitting technique is presented that allows for huge grid extensions in one dimension of the problem. A decomposition of the wave function into sums of products states is also discussed as a way of reducing computational effort.

2.1 Grid construction

All computations contained in this work have been done on a simple rectangular, regularly spaced grid in each dimension. The size of the grid (in atomic units) is determined by the calculation that has to be done, i.e., by the strength of the laser field, the length of the laser pulse and the amount of data that is wanted to be kept. The simulation time certainly has influence on this parameter, since strong laser fields are capable of driving electrons hundreds or even thousands of atomic units away from their nuclear core even in ultra-short few-cycle pulses. If additionally further time of propagation without laser field is wanted to allow for the escape of the electrons from the central parts of the Coulomb well, the fastest electrons will still move on outwards without deceleration. This enhances the need for large grid sizes further. If loss of electronic probability is intolerable, an additional security buffer should be appended. For 2D simulations, numbers of about 10^6-10^7 grid points are easily reached, combined with long propagation times.

The grid *spacing* on the other hand is chosen according to the momenta that can occur during a calculation. The highest frequency that can be displayed on a discrete grid is

$$\omega_{\max} = \frac{2\pi}{2\Delta} = \frac{\pi}{\Delta}, \tag{2.1}$$

where Δ is the grid spacing. This is clear because the fastest oscillation detectable on a discrete grid would be two values changing back and forth grid point after grid point. This oscillation has exactly the above mentioned frequency $\omega_{\max}$. The sampling theorem reflects exactly this fact, since it says that one always has to sample a continuous function with at least twice the highest occurring frequency to uniquely represent it in Fourier space. Therefore, a careful investigation of the system and an estimation of the momenta possible within the dynamics during propagation has to be done first. In particular, the two degrees of freedom appearing in this thesis behave quite differently due to the large difference in mass and acceleration and have to be treated separately within this estimation.

For this work, we chose a grid spacing of $\Delta z = 0.36$ a.u. for the electronic coordinate and $\Delta R = 0.05$ a.u. for the nuclear coordinate. This reflects the very different momenta due to the three orders of magnitude of difference in mass of electron and nuclei. This obviously dominates over the driving of the laser field, which only affects the electron, while the nuclei oscillate in a Born-Oppenheimer potential with practically no dissociation.

2.2 Propagating the Wave function

To propagate the wave function $\psi(\mathbf{x}, t)$ in time, i.e., to solve the TDSE

$$i\frac{\partial}{\partial t}\psi(\mathbf{x}, t) = \widehat{H}(\mathbf{x}, t)\psi(\mathbf{x}, t), \tag{2.2}$$

the Split-Operator technique is used. Within this approach, the time-evolution operator

$$\widehat{U}(t', t) = \widehat{\Theta}\, \exp\left(-i \int_t^{t'} \widehat{H}(\tau)\, \mathrm{d}\tau\right), \tag{2.3}$$

where $\widehat{\Theta}$ is the time-ordering operator reflecting the fact that $\widehat{H}$ will not commute with itself at differnt times, is decomposed in the following way: The Hamilton operator consists of potential and kinetic parts, i.e., parts that contain only derivatives with respect to coordinates, and parts that contain only coordinates,

$$\widehat{H}(\mathbf{x}, t) = \widehat{T}(\partial_{\mathbf{x}}) + \widehat{V}(\mathbf{x}, t), \tag{2.4}$$

where the vector $\mathbf{x}$ stands for all coordinates of the system. If we consider an infinitesimal time step $\mathrm{d}t$, the above equation (2.3) simplifies to

$$\widehat{U}(t + \mathrm{d}t, t) = \exp\big[-i\widehat{H}(t)\mathrm{d}t\big], \tag{2.5}$$

where we assume that the time dependence within the Hamiltonian itself is in a sense slow. In fact, the meaning of "slow" can be clearly expressed as soon as numerical

application of this method takes place, for then the infinitesimal time step dt has to be replaced by some finite time step δt. The necessary condition is then that the Hamiltonian changes only negligibly within a time change δt. Assuming all these conditions are met, propagating a wave function from time t to time $t + \delta t$ reduces to the application of the time evolution operator,

$$\psi(\mathbf{x}, t + \delta t) = \exp\big[-i\widehat{H}(t)\delta t\big]\psi(\mathbf{x}, t). \tag{2.6}$$

Splitting the Hamiltonian as in Eq. (2.4) gives

$$\exp\Big(-i(\widehat{T} + \widehat{V})\delta t\Big) = \exp(-i\widehat{T}\delta t)\exp(-i\widehat{V}\delta t)\exp\Big(-i[\widehat{T}, \widehat{V}]\delta t^2/2 + \mathcal{O}(\delta t^3)\Big) \tag{2.7}$$

according to the Baker-Hausdorff formulae, and in general $[\widehat{T}, \widehat{V}] \neq 0$. We will ignore terms above square order in δt from now on. But still, leaving out the term containing the commutator will introduce a large error proportional to δt^2. However, if we further split the central term into $\exp(-i\widehat{V}\delta t/2)\exp(-i\widehat{V}\delta t/2)$, and then change order with the first term, we introduce a phase, such that

$$\begin{aligned}\exp(-i\widehat{T}\delta t)\exp(-i\widehat{V}\delta t/2)\exp(-i\widehat{V}\delta t/2) = \\ \exp(-i\widehat{V}\delta t/2)\exp(-i\widehat{T}\delta t)\exp(-i\widehat{V}\delta t/2)\exp(i[\widehat{V}, \widehat{T}]\delta t^2/2),\end{aligned} \tag{2.8}$$

where the phase exactly compensates for the above term of order $\mathcal{O}(\delta t^2)$. So, if the Hamiltonian is symmetrically split, the time evolution operator reduces to

$$\exp\Big(-i\widehat{H}(t)\delta t\Big) = \exp\left(-i\frac{\widehat{V}}{2}\delta t\right)\exp\Big(-i\widehat{T}\delta t\Big)\exp\left(-i\frac{\widehat{V}}{2}\delta t\right)\exp\big(\mathcal{O}(\delta t^3)\big). \tag{2.9}$$

The last factor is now close enough to unity to be ignored. This form of the time evolution operator is now easily applicable. The two factors containing the potential operator act on the (coordinate-space) wave function by simple multiplication, since they are diagonal in coordinate space. An alternative approach would be the application of the Crank-Nicolson algorithm, an implicit scheme working with finite differences to express the time and space derivatives. In this thesis, the Fourier transform was used instead: In momentum space, the kinetic factor is also diagonal. The clear payoff is that Fourier transforms cannot be efficiently parallelised. But since this was never wanted, the existence of an efficient discrete Fourier transform algorithm (FFTW) was rated higher than possible parallelisation. Altogether, time evolution now results in

$$\psi(\mathbf{x}, t + \delta t) = \exp\left(-i\frac{\widehat{V}}{2}\delta t\right)\mathcal{F}^{-1}\exp\Big(-i\widehat{\widetilde{T}}\delta t\Big)\mathcal{F}\exp\left(-i\frac{\widehat{V}}{2}\delta t\right)\psi(\mathbf{x}, t), \tag{2.10}$$

where $\widehat{\widetilde{T}}$ is the kinetic energy operator in momentum representation, $\mathcal{F}$ is the Fourier transform operator, defined by

$$\mathcal{F}\psi(\mathbf{x}, t) \equiv \widetilde{\psi}(p_{\mathbf{x}}, t) = \frac{1}{2\pi}\iint \mathrm{d}\mathbf{x}\exp(-ip_{\mathbf{x}}\mathbf{x})\psi(\mathbf{x}, t), \tag{2.11}$$

transforming from coordinate space to momentum space, and $\mathcal{F}^{-1}$ is the inverse Fourier transform operator transforming back from momentum to coordinate space. No derivatives have to be performed, all operators act by simple multiplication, because they are diagonal in their application domain. Instead, though, time evolution now contains two Fourier transforms. The accuracy of this method obviously depends strongly on the size of the time step δt. The time step has to be chosen in such a way that no significant change within the Hamiltonian takes place during a time δt. In our case, this means that the laser field must not change significantly during a time δt. This, and the energies appearing within the simulation, determines the actual size of the time step.

As another advantage of this method, the applied operator is unitary, therefore the norm of the wave function stays constant. No re-normalisation during the propagation is necessary.

2.3 The Time-step

As just mentioned in the previous section, the size of the time step δt is crucial for the accuracy of the propagation operator. In principal, there exists a method to increase the time step via introduction of another splitting of the Hamiltonian into five terms [11]. This could reduce computational effort since a larger time step means lesser propagation steps for the same time period. But the size of the time step also comes into play when looking at the energies within the system, since in quantum mechanics, energy converts to temporal oscillation within the wave function. Of course, it is always possible to expand a wave function into energy eigenstates of the system,

$$\psi(\mathbf{x}, t) = \sum_n \psi_n(\mathbf{x}) \exp(-iE_n t). \tag{2.12}$$

The stationary eigenstates $\psi_n(\mathbf{x})$ will rotate in complex space with frequencies ω_n proportional—and in the system of atomic units identical—to their eigen-energy E_n. The size of the time step now determines the maximum frequency of rotating energy eigenstates that can be represented within the simulation. Hence, the time step sets an upper limit to energies that will be treated correctly during the simulation according to

$$E_{\max} = \frac{\pi}{\delta t}. \tag{2.13}$$

Therefore, a careful estimation of energies appearing during the simulation has to be carried out. In our case, the maximum energy investigated within the kinetic-energy spectra of photo-electrons reaches up to 80 eV corresponding to approximately 3 a.u. of energy. This alone would allow for a time-step of about $\delta t \approx 1$ a.u., which is too large in any case. Here, obviously the split operator method sets the restrictions. We chose a time-step of $\delta t = 0.0276$ a.u. which was confirmed to be sufficiently small to yield correct results.

2.4 Finding the Ground State

There exist different techniques to calculate numerically the ground state of a given Hamiltonian. Only one of them is used in this present work. Anyway, another famous one shall at least be mentioned, because it is quite elegant and fruitful for situations where the other one fails. This method is called *Spectral Method*. In contrast to this, the method of *Imaginary-Time Propagation* is used exclusively throughout this work, because it was found to be very reliable, and the major payoffs it brings along with it did not gravely advise against it in this particular case.

The results for the 2D ground states of H_2 and D_2 as modelled in this work are plotted in Fig. 3.11. Also, the vibrational ground and excited states of $H_2{}^+$ and $D_2{}^+$ have been calculated with this method. The results of vibrational energies can be found in the Appendix, Tab. A.1. The ground-state energies of the neutral systems came out as $E_0^{H_2} = -1.164536$ a.u. and $E_0^{D_2} = -1.167439$ a.u., respectively.

2.4.1 The Spectral Method

The Spectral Method utilises the spectrum of the autocorrelation function of a wave function propagating under the influence of the Hamiltonian in question. It is not important to choose a specific wave function for this method to work. The only thing one has to do is propagate the chosen wave function in time. Since this is wanted in later calculations anyway, there has so far no extra work to be done.

It is generally possible to decompose a wave function into a superposition of energy eigenstates of the Hamiltonian H under consideration. (For the sake of simplicity, we will discuss here only the one-dimensional case.) Let us assume we know the energy eigenstates $\psi_n(x)$ of the system,

$$H\psi_n(x) = E_n\psi_n(x), \tag{2.14}$$

and hence the decomposition of our initially chosen wave function $\psi(x)$ into these eigenstates, namely

$$\psi(x) = \sum_n a_n\psi_n(x), \quad a_n = \int \psi_n^*(x)\psi(x)\,\mathrm{d}x. \tag{2.15}$$

Then we also know the time evolution of the wave function under the Hamiltonian in question,

$$\psi(x,t) = \exp\big[-iHt\big] \sum_n a_n\psi_n(x) \tag{2.16}$$

$$= \sum_n a_n\psi_n(x)\exp(-iE_nt), \tag{2.17}$$

where the second equality only holds for time-independent Hamiltonians. This represents the well-known fact, that the energy eigenstates $\psi_n(x)$ of a Hamiltonian system only gain a phase under time evolution, which is proportional to the energy E_n of the eigenstate in question. In other words, all the different energy eigenstates 'rotate' in the complex plane, having all different angular frequencies $\omega_n = E_n$. (Of course they

are only all different if the system shows no degeneracy.) Now we have easy access to the eigenenergies of the system, which are proportional to the rotation frequencies of the energy eigenstates under time evolution. Let us assume that there is only a finite number N of eigenenergies available for the system. Obviously, each energy eigenstate $\psi_n(x)$ oscillates with its specific eigenfrequency $\omega_n \equiv E_n$. Hence, after a time $2\pi\omega_n^{-1}$, the eigenstate revives for the first time. In other words, $\psi_n(x,0) = \psi_n(x, 2\pi\omega_n^{-1})$. This is of course true for all n. If this process happens several times, a structure in the time propagated wave function builds up. To get access to this structure, we calculate the autocorrelation function of $\psi(x,t)$, namely

$$C(t) = \int \psi^*(x,0)\,\psi(x,t)\mathrm{d}x. \tag{2.18}$$

This yields information about when in time $\psi(x,t)$ resembles its structure of time $t = 0$. One can easily estimate that there are not only similarities within the wave function for full revivals after time Ω^{-1}, but also partial revivals after each time ω_n^{-1} when only one of the energy eigenstates resembles its structure from time $t = 0$. This can be seen by using the wave function expansion (2.15) in the definition of the autocorrelation function,

$$C(t) = \sum_n |a_n|^2 \exp(-iE_n t). \tag{2.19}$$

All coefficients being real now, the frequencies involved in the change of the wave function are clearly identified as $\omega_n = E_n$. To obtain the eigenenergies of the system, we therefore calculate the spectrum of the autocorrelation function,

$$\widetilde{C}(E) = \frac{1}{2\pi}\int C(t)\exp(iEt)\,\mathrm{d}t \tag{2.20}$$

$$= \sum_n |a_n|^2 \delta(E - E_n). \tag{2.21}$$

The spectrum is peaked at the eigenenergies of the system. This result is of course only the ideal limiting case for infinitely long propagation, which in practise can never be reached. Nevertheless, it makes good sense to propagate for a time $T = N\,2\pi\omega_0^{-1}$, $N \gg 1$, where ω_0 is the ground-state frequency, or alternatively the lowest frequency of interest. Depending on the propagation time, we can now calculate the eigen-energies up to arbitrary accuracy. Obviously, the high frequencies will appear already for short propagation times, while the lowest eigenenergies will only show up if they cycle often enough and hence leave their marks in the autocorrelation function.

With the eigenenergies at hand, we can now calculate the energy eigenstates of the system. To accomplish this, we multiply the initial wave-function $\psi(x, t = 0)$ with the complex conjugate of the phase factor that belongs to the energy in question,

$$\widetilde{\psi}_{n'}(x,t) = \psi(x,t)\exp(iE_{n'}t), \tag{2.22}$$

containing the eigenenergy $E_{n'}$ picked from the autocorrelation spectrum. This leads to the expansion

$$\widetilde{\psi}_{n'}(x,t) = \sum_n a_n\psi_n(x)\exp(-iE_{nn'}t), \quad E_{nn'} = E_n - E_{n'}. \tag{2.23}$$

For $n = n'$, the exponential vanishes, hence $\psi_{n'}(x)$ is the only function in the expansion with constant phase 1. All other contributors oscillate in time and therefore average out under a time integration,

$$\psi_{n'}(x) \propto \int_0^T \widetilde{\psi}_{n'}(x,t)\,\mathrm{d}t = \int_0^T \psi(x,t)\exp(iE_{n'}t)\,\mathrm{d}t. \tag{2.24}$$

With this method, any energy eigenstate from the spectrum is directly accessible. This is the major difference between this technique and the following one.

2.4.2 Imaginary-Time Propagation

This method was used to calculate the initial states for all simulations within this work. The major limitation is the necessity of the Hamiltonian to be bound from below, because this technique will always drive a wave function towards the energetically lowest-lying accessible state. If there is now lower bound, the method will not converge. Therefore, it is e.g. not suited for ground states of Dirac calculations, which contain negative energy states of arbitrary depth.

The idea of this method is based on a simple mathematical trick: Again we assume to know all energy eigenstates $\psi_n(x)$ of the system under consideration. Then, again, we also know the time evolution of a given wave function,

$$\psi(x,t) = \sum_n a_n\psi_n(x)\exp(-iE_nt), \quad a_n = \int \psi_n^*(x)\psi(x,t=0)\,\mathrm{d}x. \tag{2.25}$$

But changing time from t to $-i\tau$, i.e. propagating (backwards) in *imaginary time*, we replace the oscillating phases $\exp(-iE_nt)$ of the energy eigenstates by an exponential damping $\exp(-E_n\tau)$, the damping factor being the respective eigenenergy E_n, assuming only positive energies so far. Hence, higher energies lead to stronger damping of the respective eigenstate in the composition of the total wave function. In other words, the state with lowest energy is least damped during time evolution and will gain dominance over all others within the expansion. In the case of negative eigen-energies, the method still works, but the lowest-lying state is now the one *gaining* most of all states in the expansion. This also shows, why a system has to be bound from below. If this were not the case, this would imply infinitely growing exponentials in this step. Unbound systems simply do not converge.

After several time steps of propagation, one has to re-normalise the wave function and to continue propagating in imaginary time. As the method obviously converges towards the energetically lowest-lying eigenstate *contained in the initial wave-function* $\psi(x,t=0)$, one has to take care that the desired state (usually the ground state of the system) is present in the initial wave function, which is otherwise arbitrary. Starting with a constant function $\psi(x,0) = \mathrm{C}$ (gerade function of x) or $\psi(x,0) = x$ (ungerade function of x) as initial wave function is a good starting point to guarantee a nonzero overlap with any state in question. Anyway, usually small numerical errors always lead to a small occupation of the ground state level, so that any wave function should fit as a starting point.

It is also possible to converge to other states than the ground state of the system, as long as there is a possibility to select it. One example would be to relax to the

energetically lowest-lying state of a certain symmetry, which need not necessarily be the ground state. By repeatedly projecting out the symmetric fraction of the wave function,

$$\psi_-(x,t) = \psi(x,t) - \int \psi_+^*(x,t)\psi(x,t)\,\mathrm{d}x, \quad \psi_+(x,t) := \frac{1}{2}[\psi(x,t) + \psi(-x,t)], \quad (2.26)$$

which will due to numerical errors usually be slightly populated again and again, one will finally relax to the lowest antisymmetric state contained in the initially chosen wave function, and vice versa. Higher excited states can also be calculated in the same way by projecting out all lower-lying states in the process of damping. Obviously, one needs to know them before. It is *not* possible to selectively calculate an energy eigenstate somewhere in the middle of the spectrum, in contrast to the Spectral Method mentioned above. One always has to climb the ladder starting from the lowest accessible state of the system.

The eigenenergy $E_{n'}$ of the just found state can easily be calculated from the norm of the wave function, as soon as the relaxation has completed and only one energy eigenstate is occupied. Then, the damping acquired during one 'propagation step' is known and contains the energy wanted. After normalisation of $\psi(x,\tau)$, we apply one final 'propagation' step and arrive at

$$\psi(x,\tau - id\tau) = \psi(x,\tau)\exp(-E_{n'}d\tau) = a_{n'}\psi_{n'}(x)\exp(-E_{n'}d\tau), \quad (2.27)$$

all the other states being successfully suppressed, i.e. in particular $|a_{n'}| = 1$. The norm of this wave function reduces to

$$\|\psi(x,\tau - id\tau)\| = \int |a_{n'}\psi_{n'}(x)\exp(-E_{n'}d\tau)|^2\,\mathrm{d}x \quad (2.28)$$

$$= |a_{n'}|^2\exp(-2E_{n'}d\tau) \quad (2.29)$$

$$= \exp(-2E_{n'}d\tau). \quad (2.30)$$

Therefore,

$$E_{n'} = -\frac{1}{2d\tau}\ln\|\psi(x,\tau - id\tau)\|\,. \quad (2.31)$$

This method is also very easy to implement, because again nothing more than simple propagation in (imaginary) time is needed.

2.5 Masking

To avoid reflections at the grid boundaries, masking functions are used to force the wave function smoothly down to zero before the grid borders are reached. In a simulation such as those used in this thesis, it is hardly possible to prevent tiny fractions of the wave function from hitting the grid boundaries. A grid size which would guarantee this is by far too large in terms of physically significant effects. The exact amount of loss can be checked via this technique, and the procedure is absolutely safe as long as the masking region x_m is large enough,

$$x_m > \frac{p_x^{\max}}{m_x}\Delta t, \quad x = z, R, \quad (2.32)$$

where $p_x^{\max}$ is the largest momentum present in the x-coordinate, m_x is the mass of the corresponding particle and Δt is the time step used within the calculations. As a good estimate, the maximum momenta representable on the grid in each direction can be taken as $p_x^{\max}$, see section 2.1. This way it is impossible for the wave function to reach one of the grid boundaries before being damped out.

Also when analyzing the wave function with respect to ionisation, only certain parts of the grid will be used as a basis for further calculations such as spectral analysis. To obtain reasonable results after application of, say, Fourier transforms, one should take care that the grid part in question is masked out with a smooth window function, such that the function under investigation will smoothly run to zero within this area. This avoids artifacts in the spectra due to abrupt changes of the wave function at the ends of the examined intervals, which would lead to high frequency contributions not present in the data itself.

The mask functions used are simple (halves of) Hanning windows,

$$w_{\pm}^{\mathrm{H}}(x) = 0.5 \pm 0.5 \cos\left(\frac{x}{x_m}\,\pi\right), \quad x \in [0, x_m], \tag{2.33}$$

where the sign of the second term determines the orientation of the mask, i.e., distinguishes rising and falling mask functions.

2.6 Fourier Transformations

The propagation scheme applied in this work, as well as spectral analysis, calculation of the Wigner distribution function and even convolution of a function with a kernel involve applications of Fourier transforms. If Fourier transformations are applied numerically, usually we automatically speak about Fast Fourier Transforms (FFTs). A huge amount of literature can be found on this topic. This work will only contain a brief overview of important facts and details necessary to follow the steps done to obtain the presented results.

Every part of a wave-function that has been Fourier-transformed within this work has beforehand been masked with a smooth mask function. We refer to Section 2.5 for details. This is important to avoid artifacts stemming from abrupt changes at the boundaries of the grid. They are easily produced when cutting somewhere in the middle of the grid. This way, extremely high frequency components are introduced artificially, later spoiling the spectrum. Additionally, one has to take into account that an FFT is always a circular Fourier transform, i.e., the data is bent 'round the corner such that the array loops within itself. In other words, the data is repeated periodically. Therefore, if the data is not really periodic but limited, as is the case for grid snippets, padding zeros at the end will lead to an interpretation of the data by the FFT algorithm that matches reality better. Zero-padding of course lengthens the data array, but it only corresponds to ideal band-limited interpolation in the frequency domain, but it does *not* increase the resolution of the spectrum, since no further data is added.

All FFTs necessary for this work have been done with the routines provided by the FFTW package, version 3.0.1, which is available in the Internet.

2.7 Canonical Basis State Expansion and Correlation

2.7.1 Canonical Basis States

Let $\psi(z, R, t)$ be a time dependent two coordinate wave-function. In the context of this work, one shall interpret z and R as the electron coordinate and the core separation, respectively. Then, there naturally exists a decomposition of $\psi(z, R, t)$ into products of orthonormal single particle wave-functions,

$$\psi(z, R, t) = \sum_{i,j} a_{ij}(t)\widetilde{\phi}_i(z, t)\widetilde{\chi}_j(R, t). \tag{2.34}$$

This expansion is exact, as long as the double sum runs to infinity for both indices, i.e., the basis is complete for both degrees of freedom. If one particularly chooses the so-called *canonical basis* $\{\phi_n(z, t)\chi_n(R, t)\}$, the above double sum reduces to a single sum [12],

$$\psi(z, R, t) = \sum_{j} a_j(t)\phi_j(z, t)\chi_j(R, t), \tag{2.35}$$

and in contrast to the double sum this representation is *unique*. Still it is exact, as long as an infinite summation is applied. Under the condition that $\psi(z, R, t)$ be normalised, i.e.,

$$\iint |\psi(z, R, t)|^2 \, \mathrm{d}z \, \mathrm{d}R \equiv \iint \psi(z, R, t)\psi^*(z, R, t) \, \mathrm{d}z \, \mathrm{d}R = 1, \tag{2.36}$$

it immediately follows

$$\sum_{j} |a_j(t)|^2 = 1, \tag{2.37}$$

as is usual for an orthonormal expansion. A simple example that shows the possibility to reduce the decomposition (2.34) to a single summation is to make use of the *relative state formalism* [13],

$$\begin{aligned} \psi(z, R, t) &= \sum_{i,j} a_{ij}(t)\widetilde{\phi}_i(z, t)\widetilde{\chi}_j(R, t) && (2.38)\\ &= \sum_{i} \widetilde{\phi}_i(z, t) \sum_{j} a_{ij}\widetilde{\chi}_j(R, t) && (2.39)\\ &\equiv \sum_{i} \widetilde{\phi}_i(z, t)\widetilde{\widetilde{\chi}}_i(R, t), && (2.40) \end{aligned}$$

where $\widetilde{\widetilde{\chi}}_i(R, t)$ is the state relative to $\widetilde{\phi}_i(z, t)$, the system being in the two-particle state $\psi(z, R, t)$. This way, to each given state, the state relative to it in terms of $\psi(z, R, t)$ can be given. Of course, they are not orthogonal in the R domain owing to the arbitrariness of the chosen basis. Still, the picture of relatives states also holds for the canonical basis states: If the state within domain z is known, for a given two-particle state the state within domain R is immediately given. It is worth keeping this in mind.

2.7.2 Single-Particle Density Matrices

Now we define the reduced or single-particle density matrices

$$\rho_e(z, z', t) := \int \psi(z, R, t)\psi^*(z', R, t)\, \mathrm{d}R, \tag{2.41}$$

$$\rho_n(R, R', t) := \int \psi(z, R, t)\psi^*(z, R', t)\, \mathrm{d}z, \tag{2.42}$$

where one coordinate is integrated out respectively, and which are obviously hermitian, i.e.,

$$\rho_e(z, z', t) = \rho_z^*(z', z, t), \tag{2.43}$$

$$\rho_n(R, R', t) = \rho_R^*(R', R, t). \tag{2.44}$$

Another obvious feature of the single-particle density matrices is their unit trace,

$$\int \rho_e(z, z, t)\mathrm{d}z = \int \rho_n(R, R, t)\mathrm{d}R = 1, \tag{2.45}$$

which is identical to—and thus follows from—the normalisation condition (2.36) of the wave function. The trace is also equal to the sum of eigenvalues. This is another reason for the unity of the trace, because the sum over the eigenvalues equals unity. This is because the eigenstates of the single-particle density matrices are just the single particle orbitals $\phi_j(z, t)$ and $\chi_j(R, t)$ of the canonical decomposition (2.35),

$$\int \rho_n(R, R', t)\chi_j(R', t)\mathrm{d}R' = |a_j(t)|^2\, \chi_j(R, t), \tag{2.46}$$

$$\int \rho_e(z, z', t)\phi_j(z', t)\mathrm{d}z' = |a_j(t)|^2\, \phi_j(z, t), \tag{2.47}$$

with corresponding eigenvalues $|a_j(t)|^2$. The above relations are readily verified by inserting the decomposition of $\psi(z, R, t)$ and making use of the orthonormality of the single particle orbitals. Consequently, one gets the weights $|a_j(t)|^2$ of the canonical decomposition of $\psi(z, R, t)$ in product states of single particle orbitals as eigenvalues of the two single particle density matrices ρ_e and ρ_n. We have *the same* eigenvalues for both matrices ρ_e *and* ρ_n![1] In retrospective, the fact that any two-particle state can be decomposed into a single sum of product states stems from the possibility to diagonalise the respective single-particle density matrices. This is also nicely explained in [14]. The canonical basis states have been computed as eigenvectors of the single-particle density matrices with the help of the LAPACK package, version 3.0, for this work.

2.7.3 A Correlation Measure

As a measure of the correlation between the two contributing particles, it turns out to be sensible choosing the "amount of non-pureness" of the respective single-particle states. By this is meant that in case of a perfectly uncorrelated state, the corresponding

[1] Due to this fact, from now on only *the* single particle density matrix (in the sense of being one of the two) is spoken of.

single-particle states would be pure, leading to a product two-particle state. This in turn is identical to a single eigenvalue $\left|a_{j'}(t)\right|^2$ of the single particle density matrix being equal to one, all other eigenvalues being simply zero,

$$|a_j(t)| = \delta_{jj'}. \tag{2.48}$$

In other words, only one single particle orbital is occupied. In this case we know that the (single particle) density matrix becomes *idempotent*, i.e. $\rho^2 = \rho$, or in other words, becomes a *projector*. In the case of a non-pure, i.e., mixed state, other orbitals are also occupied, leading to the fact that squaring the density matrix (as a side effect) reduces the size of its trace, because it is *no projector* any more. The more states are involved, the less the trace of the squared density matrix gets. Thus, a sensible measure for the lack of correlation is the sum of the squared eigenvalues of the density matrix,

$$\sum_j \left(|a_j(t)|^2\right)^2 \equiv \sum_j |a_j(t)|^4 , \tag{2.49}$$

and the reciprocal of it,

$$K := \left[\sum_j |a_j(t)|^4\right]^{-1}, \tag{2.50}$$

is a measure for correlation. This quantity is equal to 1 for the case that only one product state of the canonical expansion is occupied, i.e. for a pure single particle state. In all other cases, it grows, having a maximum[2] of N. This maximum is a numerical artifact, as there are infinitely many possible product states in the expansion of the two particle wave-function. So in fact, theoretically, K—and thus the correlation—can increase without limit.

An easy way to see that the quantity K reflects the amount of correlation between the two degrees of freedom can be asking the following question: If one knows the state of one particle, does one gain information about the state of the second? If there is only one product state in the expansion, the answer is surely no. As before, we know the states of both particles *exactly*, and we don't learn anything by measuring one of them. But the more single-particle states involved in the expansion, the more we know about the second particle when measuring the first one. We can determine one of the N states in the expansion as the one the second particle *must* be in. This means lots of information gain, going down from N possibilities to only one. Therefore it is clear, that the more states are involved, the higher the correlation, and the more information is gained about one particle if one measures the other. If, e.g., one imagines all the states of both particles being Gaussians, highly localised in position space with pairwise little overlap, then we could easily estimate the position of one particle by measuring the position of the other, which is not possible beforehand. This example was taken from [15].

[2]This maximum is easily calculated if you consider the "most unpure state" you can think of, i.e., all possible product states—there being N of them—populated equally by a fraction of $1/N$. In this case, the sum of squares is simply $\sum_{j=1}^{N} N^{-2} = N^{-1}$, so $K = N$.

2.7.4 Numerical Access to the Correlation

The numerical calculation of K is quite easy due to a few facts from linear algebra. We know from above section that we need to calculate the sum of the squared eigenvalues of the single particle density matrix. How to obtain them? Of course there exist lots of numerical methods to calculate the eigenvalues of a matrix, which we only need to square before summation. The more sophisticated approach should instead be the following: Consider the density matrix ρ in diagonalised form, ρ^{diag}. We can achieve this by performing a similarity transform to ρ, which reads

$$U^\dagger \rho U = \rho^{\mathrm{diag}}. \tag{2.51}$$

Now, if we square the whole diagonal matrix, $(\rho^{\mathrm{diag}})^2 = \rho^{\mathrm{diag}}\rho^{\mathrm{diag}}$, the result will still be a diagonal matrix, with the diagonal elements being the squared diagonal elements, i.e. the squared eigenvalues, of the initial matrix. Its trace would therefore simply be the sum of the squared eigenvalues, which is what we were looking for,

$$\mathrm{tr}\big[(\rho^{\mathrm{diag}})^2\big] = \sum_j |a_j(t)|^4 . \tag{2.52}$$

For makings things even easier, remember that the similarity transform involves the matrix U, which is unitary, i.e., $UU^\dagger = U^\dagger U = 1$. Therefore one gets

$$(\rho^{\mathrm{diag}})^2 = U^\dagger \rho U U^\dagger \rho U = U^\dagger \rho^2 U, \tag{2.53}$$

which means that also the square of ρ is transformed in the same manner. Remembering finally that the trace of a matrix is independent of its particular representation, i.e., the trace is invariant under unitary transformations of the matrix, such that we get

$$\mathrm{tr}\big[(\rho^{\mathrm{diag}})^2\big] = \mathrm{tr}(U^\dagger \rho^2 U) = \mathrm{tr}\,\rho^2, \tag{2.54}$$

which gives us the possibility to calculate the sum of the squared eigenvalues simply by tracing out the square of the single particle density matrix. This does not even involve a whole matrix multiplication, because we are only interested in the diagonal elements of the squared matrix. In this new situation, the correlation parameter reads

$$K = \big[\mathrm{tr}\,\rho^2\big]^{-1}. \tag{2.55}$$

If we make use of the definitions of the density matrices (2.41) and (2.42), the trace converts to

$$\operatorname{tr}\rho_n^2(R,R',t) = \iint \delta(R-R') \int \rho_n(R,R'',t)\rho_n(R'',R',t)\,\mathrm{d}R''\,\mathrm{d}R'\,\mathrm{d}R \tag{2.56}$$

$$= \iint \rho_n(R,R'',t)\rho_n(R'',R,t)\,\mathrm{d}R''\,\mathrm{d}R \tag{2.57}$$

$$\overset{1.}{=} \iint \left|\rho_n(R,R'',t)\right|^2\,\mathrm{d}R''\,\mathrm{d}R \qquad \text{and} \tag{2.58}$$

$$\overset{2.}{=} \iiiint \psi(z,R,t)\psi^*(z,R'',t)\psi(z',R'',t)\psi^*(z',R,t)\,\mathrm{d}z'\,\mathrm{d}z\,\mathrm{d}R''\,\mathrm{d}R \tag{2.59}$$

$$= \iiiint \psi(z,R,t)\psi^*(z',R,t)\psi(z',R'',t)\psi^*(z,R'',t)\,\mathrm{d}z'\,\mathrm{d}z\,\mathrm{d}R''\,\mathrm{d}R \tag{2.60}$$

$$= \iint \rho_e(z,z',t)\rho_e(z',z,t)\,\mathrm{d}z'\,\mathrm{d}z \tag{2.61}$$

$$= \iint \left|\rho_e(z,z',t)\right|^2\,\mathrm{d}z'\,\mathrm{d}z \tag{2.62}$$

$$= \operatorname{tr}\rho_e^2(z,z',t). \tag{2.63}$$

The conclusion is that both traces are equal (which was already clear because of equal eigenvalues for both matrices).

The logarithm of K can be interpreted as an entropy. In fact, this quantity is sometimes referred to as *Stückelberg entropy*, having values between 0 and infinity. In [14], the von Neumann entropy is used instead, being defined as

$$S := -\operatorname{tr}\rho\ln\rho, \tag{2.64}$$

where ρ can be any of the two single-particle density matrices.

2.8 Splitting the Grid

As a full two-dimensional calculation is computationally quite expensive, one always tries to simplify the problem as much as possible, even in this dimensional aspect. If we look at our particular example of a two-dimensional system, it is immediately clear that for large electronic distances z (in both directions) the interaction between nuclei and electron almost vanishes, at least simplifies a lot. This observation leads to the idea of separating the two degrees of freedom. If we simply neglect the R-dependence of the interaction between nuclei and electron, there is no mixed term in the Hamiltonian anymore, and we can try to expand the wave-function into product states. These will then be propagated separately, i.e., in only one dimension, respectively, see section 2.9.

In other words, the interaction potential $V_{\mathrm{int}}(z,R)$ will change according to

$$V_{\mathrm{int}}(z,R) \xrightarrow{z\to\infty} \widetilde{V}_{\mathrm{int}}(z,R=\text{const.}), \tag{2.65}$$

by assuming that the nuclei can be treated as fixed in space for large z. Technically this means, we let R gradually acquire some constant value in the interaction potential for large electronic distances, $R \xrightarrow{z\to\infty}$ const.

A particular choice could be taking $R_0 = 0$, i.e., replacing the two nuclei by one point charge at $z = 0$ of strength -1 (in the case of H_2) for large z. Here we obviously do not lie because for $z \to \infty$ this is in fact the true behaviour. On the other hand, to take advantage out of this, we will have to apply this approximation at some finite z_0 already. As well one could pick the most probable value of R as R_0, making the choice "correct" for the major part of the wave function. Still this means we introduce a slight error, which is not big as long as z_0 is large enough. But as we switch to the approximated potential at $z = z_0$, we then have a step in our potential, because

$$\exists R : V_{\text{int}}(z = z_0, R) \neq \widetilde{V}_{\text{int}}(z = z_0, R = \text{const}). \tag{2.66}$$

Only for $R = R_0$, this step at $z = z_0$ will vanish by construction. That means we will have to adjust the correct two-dimensional soft core-potential in a way that this step at z_0 vanishes for all R. In other words, we have to find a function $D_n(z)$ with the following properties:

- $D_n(z)$: $[0, z_0] \to [1, 0]$
- n should be a parameter allowing to adjust for smoothness of match against size of the interval of significant change.

Then we can simply replace R by $R_0 + (R - R_0)\, D_n(z)$ and at $z = z_0$ the step is gone. The easiest approach to achieve this is a direct interpolation of nth degree,

$$D_n^{(1)}(z) = (1 - z/z_0)^n. \tag{2.67}$$

This way we enforce R to become R_0 while z approaches z_0, thus matching the two potentials for all R at $z = z_0$. The degree of the interpolation n determines two things:

1. The higher the degree, the earlier (in the sense of smaller z) the correction becomes substantial.
2. The higher the degree, the smoother the matching, because all derivatives up to $(n - 1)$th degree will be continuous at z_0.

Anyway, there is a little caveat: For degrees above $n = 1$ the change sets in quite substantial even for small z, see Fig. 2.1. It would be nicer to have a matching function that starts the matching procedure at $z = 0$ as smooth as it is supposed to end it at z_0. This leads us to the next more sophisticated approach,

$$D_n^{(2)}(z) = \left[\frac{1}{2} + \frac{1}{2}\cos\left(\pi\frac{z}{z_0}\right)\right]^n. \tag{2.68}$$

With this construction, the matching sets in in a much smoother way, see Fig. 2.2. Altogether, we should take at least $n = 2$ to get a continuous derivative of our potential, because this is the force the electron experiences. Secondly, a value of n being too large leads to quite an abrupt change of the potential, which is again not desired.

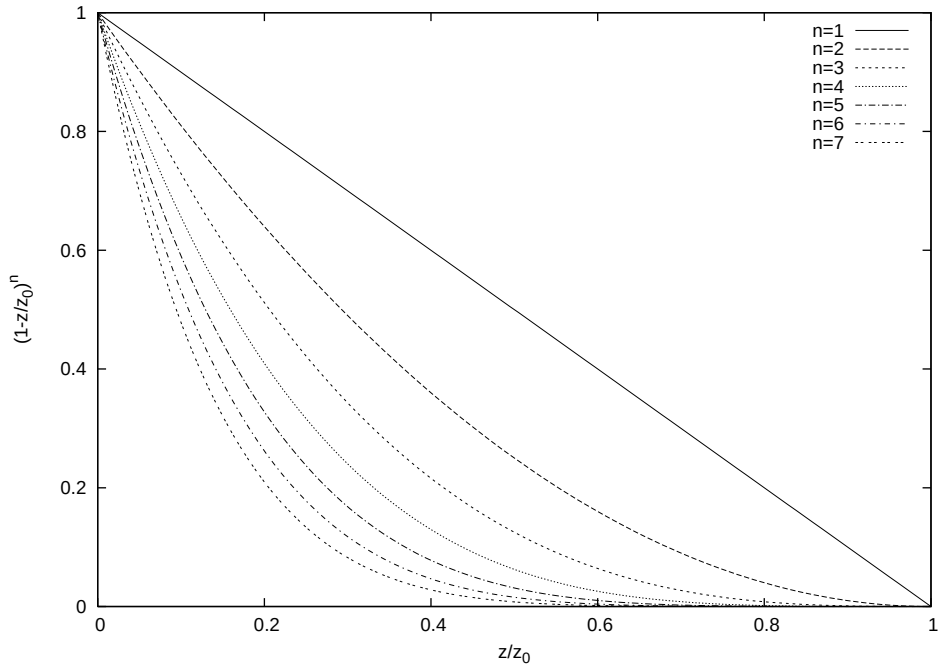

Figure 2.1: Polynomial interpolation between 1 and 0 for degrees $n = 1, 2, \ldots, 7$.

If we apply this "correction" to our soft core-potentials and take z_0 sufficiently large, the result is a smooth interaction potential that eventually changes into a one-dimensional (only z-dependent) potential for the outer part of the grid. This outer part is therefore defined by $z > z_0$. In this outer part, we are now able to decompose the wave-function into product states, propagating the two degrees of freedom separately, as there is no interaction anymore. The nuclei simply drift apart of each other due to their inherent Coulomb repulsion. It should be stressed, that only the interaction potential $V_{\text{int}}(z, R)$ is approximated towards constant R. The inter-nuclear potential is unchanged and the repulsion is fully modelled also in the outer region of the grid. The electron moves in the laser field plus a Coulomb field of two fixed nuclei.

2.9 Splitting the Wave Function

Having defined two different grids for the calculation, the next step is to define a procedure to shift the wave function across the line $z = z_0$ and to represent the wave function for the outer region $z > z_0$. As shown in section 2.7, the wave function can be easily expanded into a single sum of one-dimensional product states, using the canonical basis states as basis functions for the expansion. This is now used to decompose the wave function and make one-dimensional propagation possible. Fig.2.3 shows the principal construction of the grid: The 2D grid is the central basis of the computation (top panel). At both z-ends of the grid, the grid is extended into an outer region (central panel), which is *not* realized as a 2D grid but just sketched like that to simplify the understanding of the construction. Each time the front of the wave

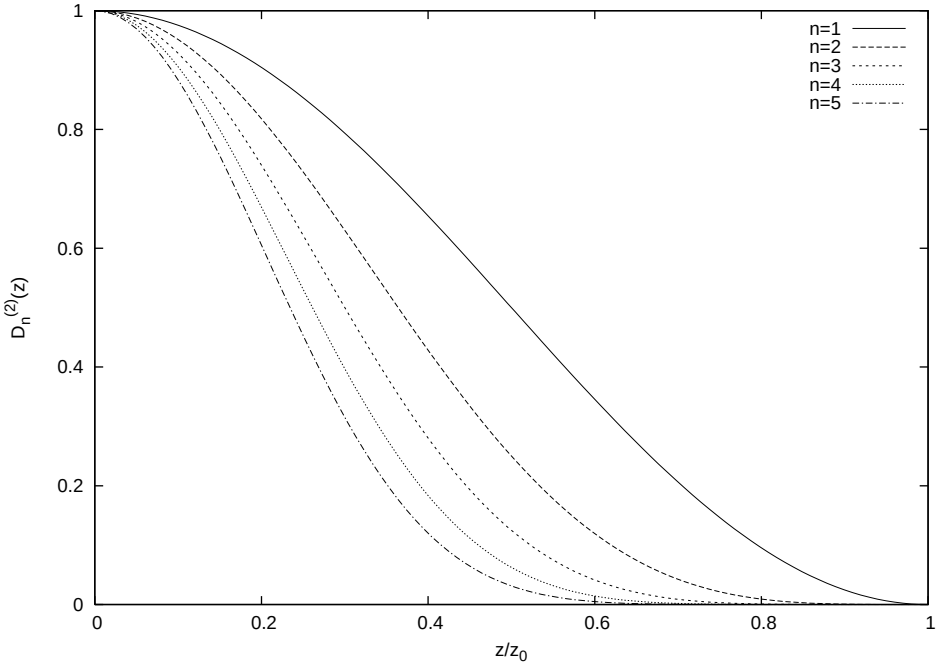

Figure 2.2: Sinusoidal interpolation between 1 and 0 for degrees $n = 1 \ldots 5$.

function is on the verge of hitting the end of the inner grid, the corresponding portion is transferred onto the outer part of the grid (lower panel). The same is valid for the counter direction: Probability moving inwards has to be prevented from colliding with the inner boundary of the outer grid and is thus transferred upwards in the same manner as described above. The part of the wave function to be transported onto another grid is smoothly masked out to avoid discontinuities at the borders of the overlap regions. The masking is implemented according to the description in section 2.5.

A few problems arise in doing this. In the following, only one of the two outer grids $z > z_0$ is considered, as everything is identically valid for the second one in the other direction of the coordinate axis.

- An overlap region has to be defined where probability can still move further, but already resides in a region where the respective other grid is present, such that transportation onto the other grid is possible.

- Within this overlap region, the potential has to be identical on both grids, i.e., already at the beginning of the overlap region, z and R have to be decoupled.

- Each time probability is shifted from the inner grid to the outer, a new decomposition of the wave function within this overlap region becomes necessary.

- Since proceeding like this implies more and more product expansions existing in parallel, even one-dimensional propagation at some point becomes inefficient.

All these items will be accounted for in the following subsection.

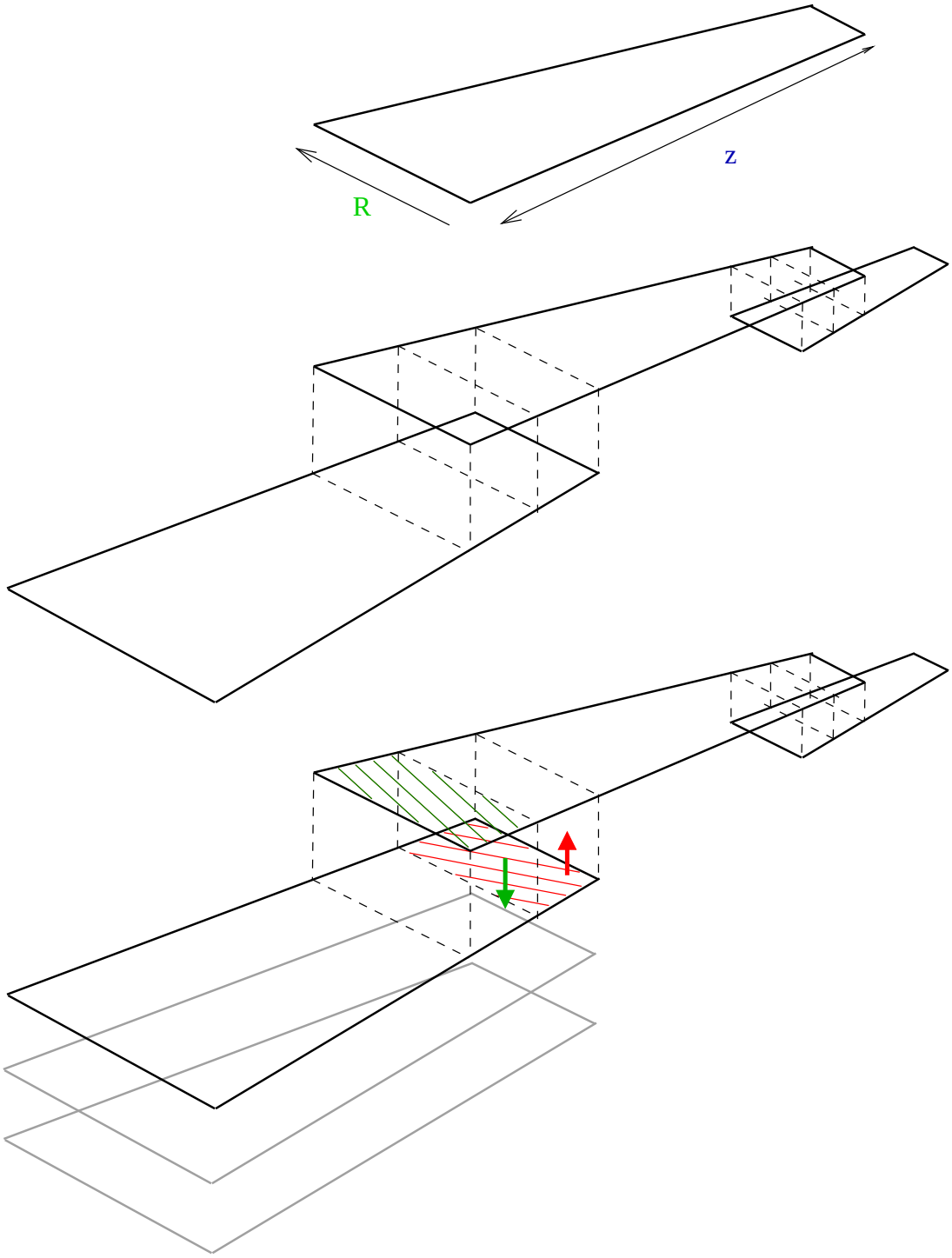

Figure 2.3: Sketch of the grid construction used in this work: A standard 2D grid is extended further in z direction. Data moving across the boundary is transferred up- and downwards, respectively. The wave function on the outer parts is expanded into a sum of canonical basis states. Since every time this happens a new decomposition is born, several "layers" will exist on the outer grid.

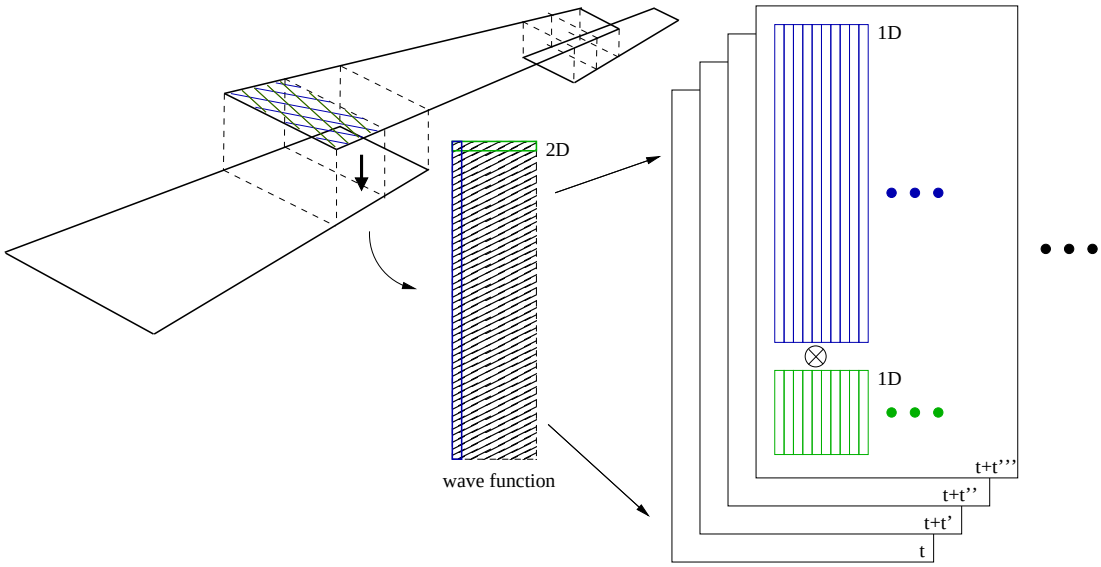

Figure 2.4: Sketch of the decomposition of the 2D wave function on the outer grid: The part of the wave function running towards a grid boundary is masked out and decomposed into canonical basis states. Those are propagated independently on a 1D grid. The coupling is removed on the outer grid. The sheets represent multiple expansions present at the same time, since every few time steps a new one has to be added.

2.9.1 Different Approaches to Splitting

Depending on the details of a particular calculation, different approaches might be appropriate. The principal technique is sketched in Fig. 2.4: The wave function residing in the overlap region is first masked out smoothly, then it is decomposed into canonical basis states. The number of expansion terms is usually limited according to a prescribed accuracy of the representation of the full 2D wave function. The sheets sketched in the picture represent the possibly necessary several instances of expansions.

Single-Layer Expansion It is of course possible to deal with only one single layer on the outer one-dimensional grid. This forces a new decomposition into a product expansion every time some probability is to be shifted to the outer grid. The whole wave function in the outer region has to be reconstructed as a two-dimensional object and coherently superimposed with the new part coming from the inner grid. This new outer wave function must now be decomposed into product states again. As this is computationally very expensive, one has to carefully investigate where this is the method of choice.

Multiple-Layer Expansion A more efficient and also easy to implement strategy is to simply add a new layer, i.e., a new product expansion, to the outer grid each time a shift of probability becomes necessary. As mentioned above, at some point this way of propagating the wave function becomes inefficient. The outer grid, containing hundreds of one-dimensional wave functions, will simply become larger than a straight-forward two-dimensional grid for the whole space. This clearly

has to be avoided. The easiest way to do this is to keep propagation time short. This way you will possibly never reach the point where too many expansions exist. However, of course this is not always possible. A combination of this approach and the previous one has to be implemented.

Restricted Multi-Layer Expansion For simulations that clearly exceed the maximum propagation time mentioned in the previous subsection, there is no way around melting all expansions on the outer grid together in one single expansion again, which has to happen at the latest when the maximum number of layers recommended has been reached. This is of course a computationally very expensive step. But having done this, we start all over again with one single layer on the outer grid and propagation becomes very efficient again. This can be done automatically and repeatedly as long as the simulation goes, no matter what the total simulation time may be. We will always stay in an efficient situation, because as soon as layers exceed the maximum allowed number, everything is wrapped onto a single one again.

2.9.2 A Simple Estimation of Computational Effort

To estimate the maximum number of layers or the maximum propagation time allowed for efficient propagation, we look at a very simple model. Only the number of grid points involved in the computation will be counted as a measure for the computational effort. The grid dimensions will be denoted by N_z and N_z' for the inner and outer grid regions in z direction, and by N_R in R direction. The number of simulation time steps will be denoted by T, the number of layers present at time t by M_t, where $t = 0, \ldots, T$. With T_{step} we denote the number of time-steps until a new expansion enters the outer grid, and $M := T/T_{\text{step}}$ is the total number of expansions asking for treatment. The number of product states within each expansion will be assumed constant for all expansions and both sides of the grid and denoted by N. For a real 2D grid this means the total number of grid points # involved[3] can be written as

$$\#(\text{2D}) = N_z N_R T + 2N_z' N_R T, \tag{2.69}$$

where the part of the outer regions is the last term

$$\boxed{\#(\text{2D}, \text{out}) = 2N_z' N_R T.} \tag{2.70}$$

Only this part of the grid is of interest, since the inner 2D part is identical for all different types of splitting methods mentioned above.

For a multi-layer grid, the number of grid points in the outer region is in any case

$$\#(\text{2D} + 2 \times \text{1D}, \text{out}) = 2N(N_z' + N_R) \sum_{t=0}^{T} M_t. \tag{2.71}$$

In some of the cases, the full outer grids have to be decomposed into product states again, which we will call a *collapse*, to reduce the number of layers to one. The number

[3] By this the size of the grid times the number of time steps they are utilised is meant.

of grid points involved in this procedure will always be

$$\#(2\mathrm{D}+2\times 1\mathrm{D},\mathrm{out},\mathrm{collapse}) = 2N_z' N_R \frac{T}{T^*}, \tag{2.72}$$

where T^* defines how often this happens. We now consider all three different types of techniques of how to deal with the outer part of the grid. This will have influence on the explicit expression of the sum $\sum_t M_t$ and the time T^*.

The first method uses only one single layer on the outer grid. If $M_t \equiv 1$ for all times, then $\sum_t M_t = T$, but additionally we have to re-expand the whole outer region each time a splitting takes place, and therefore $T^* = T_{\mathrm{step}}$, hence

$$\boxed{\#(2\mathrm{D}+2\times 1\mathrm{D},\mathrm{single},\mathrm{out}) = 2N(N_z'+N_R)T + 2N_z' N_R \frac{T}{T_{\mathrm{step}}}.} \tag{2.73}$$

If we consider unrestricted multi-layer expansion and thus allow a new layer each time a new expansion is necessary, no collapse will ever take place. Therefore this contribution is exactly zero. The sum of layers is easy to evaluate, since every T_{step} time-steps a new layer is added, up to a total number of T/T_{step}. This gives in total

$$\boxed{\#(2\mathrm{D}+2\times 1\mathrm{D},\mathrm{multi},\mathrm{out})} = 2N(N_z'+N_R)\sum_{t=0}^{T} M_t \tag{2.74}$$

$$= 2N(N_z'+N_R)T_{\mathrm{step}}\frac{M(M+1)}{2} \tag{2.75}$$

$$= \boxed{N(N_z'+N_R)T\left(\frac{T}{T_{\mathrm{step}}}+1\right),} \tag{2.76}$$

where $M = T/T_{\mathrm{step}}$ has been used. The sum was evaluated according to the fact that the number of layers will stay constant for T_{step} time-steps each time before it grows further. This situation is sketched in Fig. 2.5 in the central panel.

Comparing Eqs. (2.73) and (2.76), one beautifully sees how these two extreme cases diverge in their applications: The single-layer approach contains a part proportional to $N_z' N_R$, whereas the multi-layer approach is only proportional to the sum of both grid extensions. This shows that huge z-expansions will increase the number of grid points dramatically in the case of single-layer propagation due to the re-expansion of the whole outer grid every T_{step} time steps. On the other hand, the multi-layer approach contains a term proportional to T^2, whereas the single-layer expression is proportional to T linearly. This reflects what was already obvious, namely that for long propagation times, i.e., for large T, the multi-layer approach without limitation will surely fail because too many layers add up over time.

Application of a limiting time T_{max} to collapse the outer grid every T_{max} time steps will be considered finally, which is sketched in the lower panel of Fig. 2.5. The evaluation of the sum $\sum_t M_t$ is similar to the previous case of one flight of stairs, multiplied by the number of staircases T/T_{max}, and $T^* = T_{\mathrm{max}}$ by construction. This gives

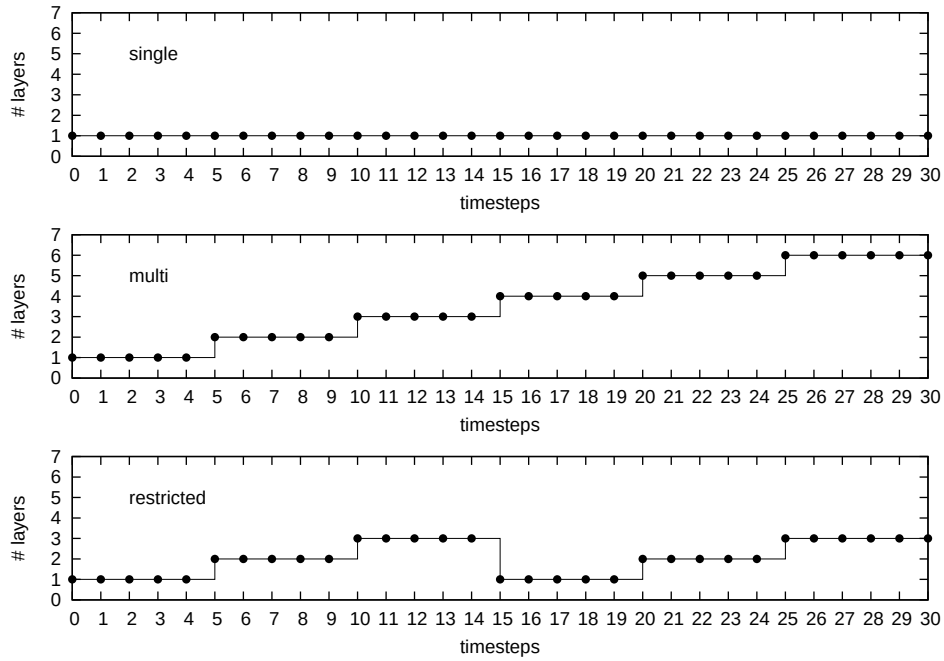

Figure 2.5: Sketch of the number of expansion layers on the outer grids for the different methods discussed within the text. For the single-layer approach (upper panel), the number of layers stays constantly one for all times. In the unrestricted multi-layer case, every T_{step} time steps, a new layer will be introduced (centre panel). If the maximum number of layers is restricted (lower panel), it will collapse to one every $T_{\max}$ time steps. In this example, $T_{\text{step}} = 5$ and $T_{\max} = 3T_{\text{step}} = 15$.

method	**propagation**	**collapse**
general	$2N(N_z' + N_R)\sum_t M_t$	$2N_z' N_R \frac{T}{T^*}$
single	$2N(N_z' + N_R)T$	$2N_z' N_R \frac{T}{T_{\text{step}}}$
multi	$N(N_z' + N_R)T\left(\frac{T}{T_{\text{step}}} + 1\right)$	
restricted	$N(N_z' + N_R)T\left(\frac{T_{\max}}{T_{\text{step}}} + 1\right)$	$2N_z' N_R \frac{T}{T_{\max}}$

Table 2.1: Estimation of the number of grid points involved in the computation in general and for three different splitting techniques, split up into contributions from the propagation of the wave function and from the collapse of the accumulated expansions into a single one.

$$\begin{aligned}\boxed{\#(2\mathrm{D}+2\times 1\mathrm{D},\mathrm{restricted},\mathrm{out})} &= 2N(N_z'+N_R)\frac{T}{T_{\max}}T_{\mathrm{step}}\frac{M_{\max}(M_{\max}+1)}{2}\\ &\quad + 2N_z'N_R\frac{T}{T_{\max}}\\ &= \boxed{N(N_z'+N_R)T\left(\frac{T_{\max}}{T_{\mathrm{step}}}+1\right)+2N_z'N_R\frac{T}{T_{\max}}.}\end{aligned} \tag{2.77}$$

All results have been collected in Table 2.1 for an overview. Apparently, we did not yet decide for a definite value of $T_{\max}$ as this value determines whether the method is advantageous over the other two or not. If $T_{\max} = T_{\mathrm{step}}$, the restricted method obviously coincides with the single-layer method. This is clear because then we would collapse every T_{step} time steps. For $T_{\max} = T$, we resemble the multi-layer case without restriction. (The single product term $2N_z'N_R$ stemming from the collapse contribution can safely be ignored since the ansatz did not take into account, that at the end of the propagation there is no collapse necessary.[4]) As always, the truth lies somewhere in between.

The question is: How can we estimate a sensible value for a limiting number of expansion layers? The highest limit should be given at least by the number of grid points that would be involved in a true 2D calculation, since this would be the alternative approach and from this point on the more efficient one. This number is given by Eq. (2.70). We restrict the number of layers to a maximum of $M_{\max} = T_{\max}/T_{\mathrm{step}}$, where $T_{\max}$ defines the time from where on no further layers are added, but the outer region is collapsed into one layer. From there on the procedure starts from the beginning until $T_{\max}$ is reached a second time, and so forth. The time $T_{\max}$ is calculated by equating Eqs. (2.70) and (2.76), which yields

$$T_{\max} = \left(\frac{2N_z'N_R}{N(N_z'+N_R)}-1\right)T_{\mathrm{step}}. \tag{2.78}$$

Usually, we can consider 1 small against the fraction, which gives us an idea of $T_{\max}$: The ratio of $T_{\max}$ and T_{step} is given by the ratio of the grid points of a 2D outer grid and half of the grid points of a 1D outer grid, which is a reasonable result. Yet if we plug this result in Eq. (2.77), we get

$$\begin{aligned}\#(2\mathrm{D}+2\times 1\mathrm{D},\mathrm{restricted},\mathrm{out}) &= N(N_z'+N_R)T\left(\frac{T_{\max}}{T_{\mathrm{step}}}+1\right)+2N_z'N_R\frac{T}{T_{\max}}\\ &= 2N_z'N_RT + 2N_z'N_R\frac{T}{T_{\mathrm{step}}}\left(\frac{2N_z'N_R}{N(N_z'+N_R)}-1\right)^{-1}\\ &\approx 2N_z'N_RT + N(N_z'+N_R)\frac{T}{T_{\mathrm{step}}},\end{aligned} \tag{2.79}$$

where we have slightly approximated in the second term ignoring the 1 over the fraction. Interestingly, via $T_{\max}$ the contributions have changed character, namely the one

[4] Of course, there is a collapse necessary at the end of the simulation, if the 2D wave function is desired. But this is the case for *all* methods involving expansions on the outer grid.

stemming from the propagation itself is now proportional to the product of the grid dimensions, whereas the contribution from collapsing the outer grid is only proportional to their sum. However, the result is not satisfactory since the product term (having most impact on the total number) is by a factor T_{step} worse than in the case of single-layer propagation. Obviously, this approach was not strict enough, and $T_{\max}$ has to be much smaller than given in Eq. (2.78) for the restricted method to be efficient. Equating directly with the expression for single-layer propagation does not yield a simple expression for $T_{\max}$, therefore we go one step further and insert typical values for the calculations done in this work. Estimation of orders of magnitude for the different contributions shall suffice. This gives $N_z' N_R = \mathcal{O}(10^6)$ for the product, $N_z' + N_R = \mathcal{O}(10^3)$ for the sum of the grid points, $T = \mathcal{O}(10^4)$ for the number of time steps and $T_{\text{step}} = \mathcal{O}(10^2)$. The number of expansion terms N is always very low and can be estimated by an upper bound of $N = \mathcal{O}(10)$. Usually it is below 10. Now, the single-layer approach gives a number of grid points of $\mathcal{O}(10^8)$. For comparison, the true-2D approach gives $\mathcal{O}(10^{10})$ grid points. This is good news. The restricted approach gives $10^6 T_{\max} + 10^{10}/T_{\max}$. Obviously, for $T_{\max} = \mathcal{O}(10^2)$, we can keep up with the single-layer approach. This is the same order as T_{step}, which was actually the lower bound of $T_{\max}$. This means we have to choose the exact value really carefully to gain speed over the single-layer approach. Going back to the notation as in Eq. (2.78), expressing $T_{\max}$ as a multiple of T_{step}, namely $T_{\max} = nT_{\text{step}}$, we have $n = \mathcal{O}(1)$. This is much smaller than the estimation via Eq. (2.78), which would yield $n = \mathcal{O}(10^2)$.

Concluding, we definitely found a method to reduce computational effort compared to the case of a simple 2D grid. A coarse estimation gives us a reduction of grid points of two orders of magnitude. Obviously, the multi-layer approach is not suitable as well for $\mathcal{O}(10^4)$ time steps and more. In this case it already reaches the same order of grid points as the 2D case. The number of layers on the outer grid has to be kept small. Whether this number is one (single-layer approach) or slightly larger (restricted multi-layer approach), strongly depends on the detailed number values of a concrete calculation. Since it is also important, *what* is done on the grids, namely propagation via FFT in 1D opposed to matrix decomposition in 2D, in practice there will be more aspects to consider.

Chapter 3

The Hydrogen Molecule

In this main chapter of the thesis a model H_2 system will be introduced and numerically simulated and investigated with the methods described within the previous chapter. First, a basic understanding of above-threshold ionisation (ATI) of atoms and molecules in strong fields is given. Then, the concept of channel closings within strong-field ionisation of atoms in terms of number of photons absorbed by the ejected electron will be presented. This situation will then be transported to small dimers, especially H_2, which is treated in this thesis. Numerical simulations carried out on the model H_2 system will show characteristic channel-closing effects known from atoms, resulting from a change of laser intensity of the ionising laser field. Additionally, the vibrational energy scale of the dimer allows access to channel closing effects without changing the laser intensity. This is the major result presented within this work and has led to the publication of two articles [1, 2].

3.1 Above-Threshold Ionisation

3.1.1 Ionisation regimes

When ionising an atom through means of an intense laser field, depending on frequency and strength of the laser, different ionisation regimes exist. In the so-called *multi-photon regime*, which applies to low intensities and high frequencies on the scale of the binding potential of the atom, the only way out of the potential is the absorption of many photons from the laser field. If the intensity is high enough, the laser electric field is usually well described classically. Coulomb potential and electric field amplitude compete against each other with respect to the highest occupied atomic level. The Coulomb potential is bent, a (now finite) barrier builds up to one side of the potential, and if the laser suppresses the barrier below energy of the highest occupied atomic level, immediate ionisation takes place. This process is called *over-the-barrier ionisation*. For intensities just not high enough to completely suppress the ionisation barrier, there is still a chance for the electron to ionise, namely via *tunnel ionisation*. The probability of this effect to take place additionally strongly depends on the laser frequency. Since the barrier is lowered periodically twice within every laser cycle, each time on opposite sides, there is only a chance to tunnel out if the tunnelling time, i.e., the time necessary to tunnel out, is short enough. In other words, the time interval, during which the barrier

is low enough, must be long enough. Obviously, this time is inversely proportional to the laser frequency. To quantify the regime of ionisation, one refers to the often-quoted, so-called Keldysh-parameter [16, 17] $\gamma = \omega_\mathrm{L}/\omega_t$, where ω_L is the laser frequency, and $\omega_t = E/\sqrt{2I_\mathrm{p}}$ is the tunnelling frequency, depending on the maximum electric field amplitude E and the ionisation potential of the atom I_p. Assuming intensities low enough to prohibit over-the-barrier ionisation, for $\gamma \gg 1$, the laser oscillates too fast to allow for tunnel ionisation. Hence this characterises the multi-photon regime. On the other hand, if the tunnelling frequency clearly exceeds the laser frequency, i.e., $\gamma \ll 1$, tunnelling ionisation is favoured. In between these to extreme cases, all mixtures of both processes take place, with respective probability.

In the multi-photon regime, one would think in absorption of photons. In the case of tunnel ionisation, the better picture is a bent potential and a tunnel barrier. In other words, the Keldysh parameter describes the adiabaticity of the system: In the limiting case of almost zero laser frequency, the electron wave packet will tunnel through a barrier of almost constant width, which is solely defined by the laser field strength and the ionisation potential. If the laser oscillates rapidly instead, nothing like a tunnelling barrier builds up, but the potential changes dramatically back and forth before the wave packet could move significantly. This is the opposite of adiabatic motion. Yet, the electron can absorb photons and gain energy, eventually leaving the potential.

Of course, as is always the case, the intermediate situation is the most interesting one, since no crude approximations can be done emphasising only one aspect of the two alternatives. This is where numerical simulations are the best method to access the behaviour of the system, because a treatment as accurate as possible is necessary to understand the detailed and complicated dynamics. In the context of this work, we reside almost exactly in the middle of both situations, the Keldysh parameter being always between $\gamma \approx 1.81$ and $\gamma \approx 1.34$ for laser intensities between $8.132 \times 10^{13}\mathrm{W/cm^2}$ and $1.464 \times 10^{14}\mathrm{W/cm^2}$.

3.1.2 ATI peaks in kinetic energy spectra of photo electrons

From experiment it is known [18, 19] that ionising electrons can absorb by far more photons from the laser field than are actually needed to escape the binding potential of the atom, if the laser intensity is high enough. This effect is known as above-threshold ionisation. The following summary of ATI phenomena and explanations is based on [20].

In the kinetic-energy spectra of the ionised electrons, one finds sharp peaks underneath a certain envelope, all separated by the photon energy of the laser. In experiment, however, the clear peak structure is not always resolved due to so-called volume effects, i.e., the spacio-temporal intensity profile of the laser focus. In particular, it depends on the pulse length and the laser intensity. ATI is observed in the intensity regime 10^{12} W/cm^2 to 10^{16} W/cm^2.

A classical model is capable of describing the major characteristics of an ATI spectrum already. We assume that an electron moving in z direction tunnels out of the potential barrier at time t_0 and starts its orbit at $z = 0$ with an initial velocity of $\dot{z}(t_0) = 0$. As for strong fields the oscillation amplitude of the ejected electron exceeds

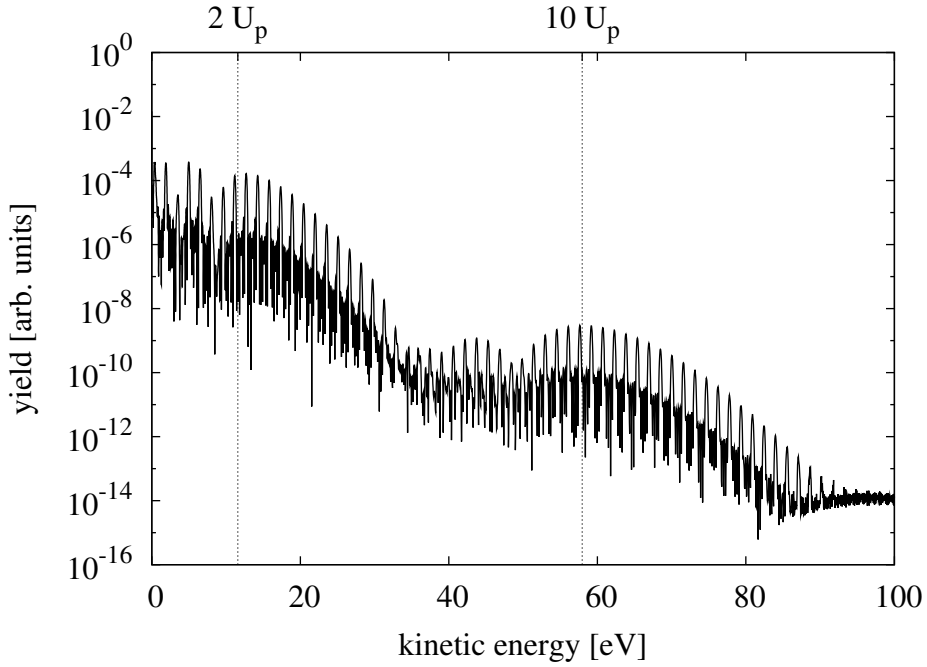

Figure 3.1: Typical atomic ATI spectrum showing the structure predicted by the three-step model. Direct electrons reach up to energies of 2 U_p, then the yield drops significantly. A plateau structure extends up to 10 U_p, which is classically the maximum energy of re-scattered electrons. There, a second and final cutoff resides.

the atomic or molecular extensions by far[1], we will ignore the Coulomb potential for a while. If the electron does not interact with the ion in any significant way, we speak of *direct* electrons. However, it may happen that the laser field drives the electron back to the ion core, where it may re-scatter. In the following, we will consider the motion of an electron within a linearly polarized, monochromatic laser field $E(t) = E_0 \sin(\omega t)$. The Newton equation of motion of such an electron is

$$\ddot{z}(t) = -E_0 \sin(\omega t). \tag{3.1}$$

Solving this equation with respect to above conditions upon initial position and velocity, we get

$$\dot{z}(t) = \alpha\omega \cos(\omega t) - \alpha\omega \cos(\omega t_0), \tag{3.2}$$
$$z(t) = \alpha \sin(\omega t) - \alpha \sin(\omega t_0) - \alpha\omega(t - t_0)\cos(\omega t_0), \tag{3.3}$$

where $\alpha = E_0/\omega^2$ is the classical oscillation amplitude. Obviously, the constant drift term $\alpha\omega\cos(\omega t_0)$ in the expression for the velocity depends in magnitude and direction on the ionisation time t_0. For long pulses, this corresponds to the final velocity of the electron after the end of the laser pulse. The maximum amounts to $\alpha\omega$, giving a maximum kinetic energy of $E_{\mathrm{kin}} = E_0^2/(2\omega^2)$. The time-dependent kinetic energy of the electron in the laser field is given by

$$E_{\mathrm{kin}}(t) = \frac{\alpha^2\omega^2}{2}[\cos^2(\omega t) + \cos^2(\omega t_0) - 2\cos(\omega t)\cos(\omega t_0)]. \tag{3.4}$$

Averaged over one laser cycle, the cross-term vanishes and we get

$$\langle E_{\mathrm{kin}}(t)\rangle_T = U_{\mathrm{p}} + 2U_{\mathrm{p}}\cos^2(\omega t_0), \tag{3.5}$$

with $U_{\mathrm{p}} = E_0^2/(4\omega^2)$ the *ponderomotive potential*, because this first term corresponds to the average kinetic energy due to oscillation. The second term, having a maximum of $2U_{\mathrm{p}}$ (depending on ionisation time t_0), is the drift energy of the electron corresponding to the drift velocity from above. For long pulses, it corresponds to the final energy of the electron. So far, these are pure classical considerations and we do not allow influence of the ionic potential. Still, this classical limit of $2U_{\mathrm{p}}$ for direct electrons is clearly visible in ATI spectra as a strong cutoff. See Fig. 3.1 for a typical ATI spectrum which stems from an atomic calculation. The yield drops significantly around $2U_{\mathrm{p}}$. For a quantum-mechanical treatment of the direct electrons, in the context of the strong-field approximation, the Keldysh-Faisal-Reiss (KFR) amplitudes have been developed [16, 21, 22, 23, 24]. Application of the saddle-point method yields a representation of the KFR amplitudes involving a coherent superposition of contributing terms, wrapped in a sum containing an energy-conserving delta function. This energy-conservation condition yields exactly the ATI condition

$$E_{\mathrm{kin}} = n\omega_{\mathrm{L}} - U_{\mathrm{p}} - I_{\mathrm{p}}, \tag{3.6}$$

[1] For lasers of 800 nm wavelength, an electric field strengh of about 10^{-2} a.u. already leads to excursions of the photoelectron of about ten Bohrs.

stemming from the interference of contributions from different laser periods. This already gives a hint, that ultra-short laser pulses will not produce the most pronounced ATI spectra.

The first cutoff is followed by the re-scattering plateau, i.e., the intensity within the next spectral region is more or less constant on a logarithmic scale. It stretches out up to approximately 10 U_p [25, 26, 27], which is the classical limit of kinetic energy for electrons re-scattering once with their parent ion, to be shown next. For this purpose, we consider its trajectory (3.3). Re-scattering at time $t_1 > t_0$ is now defined by $z(t_1) = 0$. On such a revisit, different things may happen [28]:

1. Through recombination, the electron may emit all its energy (including I_p) as one single photon, contributing to high-harmonic radiation in the plateau region.

2. Inelastic re-scattering may lead to excitation or even ionisation of the ion, which is a process mainly responsible for non-sequential double-ionisation.

3. Elastic re-scattering may lead to acquisition of more drift energy, which results in ATI peaks within the re-scattering plateau of the spectrum beyond the 2 U_p limit.

This last effect is now described in more detail. The return energy of the electron after its journey in the laser field is

$$E_\mathrm{return} = \frac{1}{2}[\dot{z}(t_1) - \dot{z}(t_0)]^2. \tag{3.7}$$

The maximum of this expression with respect to t_0, where $z(t_1) = 0$ is fulfilled, amounts to $E_\mathrm{return}^\mathrm{max} = 3.17\ U_\mathrm{p}$ [28]. In the extreme case, the electron will now re-scatter in the opposite direction, changing its momentum by sign only. This would give the final energy

$$E_\mathrm{scatt} = \frac{1}{2}[2\dot{z}(t_1) - \dot{z}(t_0)]^2, \tag{3.8}$$

which, maximised under the same conditions as above, will give $E_\mathrm{scatt}^\mathrm{max} = 10.007\ U_\mathrm{p}$ [25]. For this to happen, the electron has to escape shortly after a field maximum. It will then return to the ion close to a zero of the field. Re-scattering at this instant can therefore lead to a further acceleration of the electron via the laser field, if backscattered in the right direction. Then, higher kinetic energies are found in the ATI spectrum. An easy understanding of this procedure is to write the condition $z(t_1) = 0$ as

$$f(t_1) = f(t_0) + (t_1 - t_0)f'(t_0), \quad f(t) = \int_{t_0}^{t} \dot{z}(\tau)\mathrm{d}\tau. \tag{3.9}$$

This describes a tangent on f at t_0 that crosses f at t_1. Since this function f is the integrated velocity and hence a sinusoidal function proportional to the electric field[2], we see that a tangent at a time t_0 shortly after a maximum will indeed give a return time t_1 close to a field minimum. The less steep the tangent, the later the return, and the more further returns are possible. To a given final energy E_scatt of the electron,

[2]The electron velocity is phase-shifted with respect to the electric field by $\pi/2$.

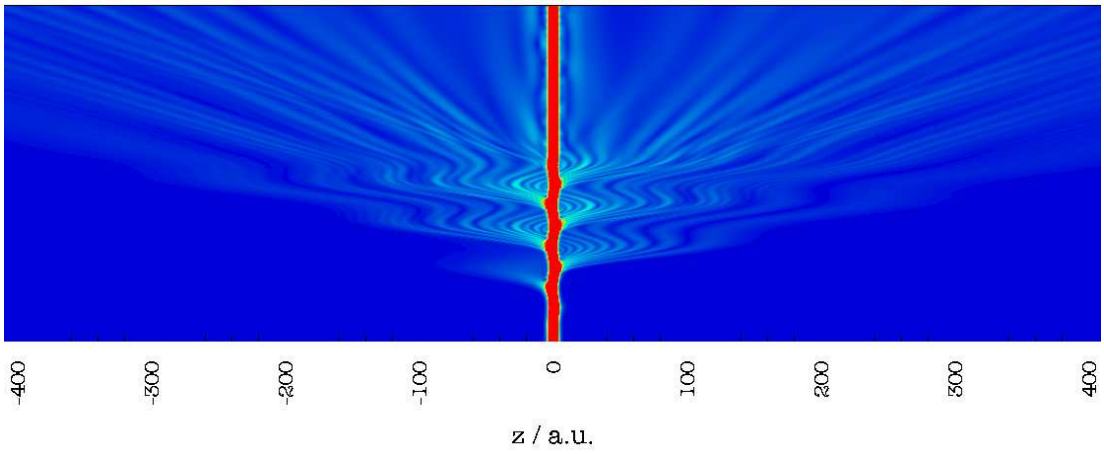

Figure 3.2: Qualitative plot for the electron density of ionising D_2 evolving with time from bottom to top. The laser intensity is $1.204 \times 10^{14}\mathrm{W/cm^2}$ ($U_\mathrm{p} = 4.63\ \omega$), the propagation time is five optical cycles plus three cycles without laser field.

there are always two start times t_0 and hence two trajectories, one shorter and one longer. If the electron does not re-scatter on its first revisit, but later, the orbit is long, but the maximum energy is then less. The highest energy of 10.007 U_p is only possible if the electron re-scatters at its first revisit. Also the re-scattering electron can be described quantum mechanically. The trajectories become complex then, because due to tunnelling under the restriction of energy conservation, a real solution does not exist. It is the interference of these complex quantum orbits that leads to enhancements within the re-scattering plateau of the ATI spectrum for certain laser intensities, as is described in the next section.

The re-scattering process (and thus the yield within the re-scattering plateau) clearly depends on the probability of the electron wave packet to re-collide with its parent ion, which can be diminished by using circularly polarised laser fields (introducing non-straight motion) [29] or extremely high intensities where the magnetic field component of the laser field introduces a drift in propagation direction of the laser field [30] strong enough to let the electron mainly miss its parent ion. This again is compensated for the case of antisymmetric states [31]. Also, extremely long trajectories, stemming from strong, slowly-varying fields, let the ionised wave packed spread in space to a large amount, such that the overlap with its parent ion at return time is fairly small. All these additional effects do not have to be considered within the present work, since all laser pulses are linearly polarised and weak enough to be able to completely ignore the magnetic-field component of the laser.

However, to produce a significant portion of re-scattered electrons, the laser pulse needs to have a certain length in terms of laser cycles. In our case, pulse lengths of five cycles prove sufficient to produce ATI orders of fifty and more. See Fig. 3.2 for a plot of electron density evolving with time. Clearly, one recognises ionisation with different energies (slopes of the trajectories), re-scattering at the ionic core and interference of electrons of different kinetic energy. The longer the pulse, the more detailed the ATI spectrum will be, since more and also not so pronounced re-scattering events will

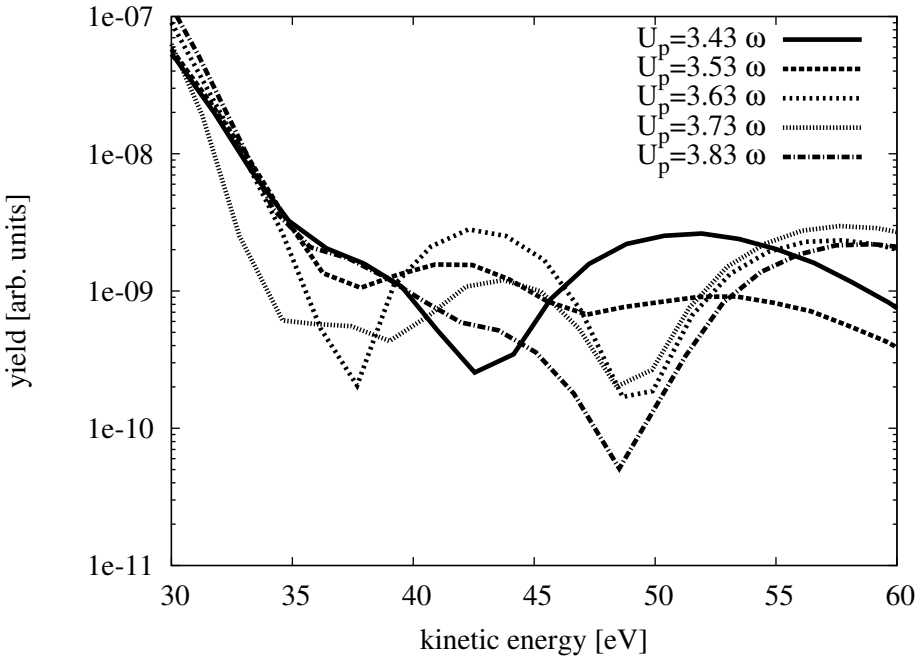

Figure 3.3: Envelopes of kinetic-energy spectra of ATI-electrons of a 1D hydrogen atom described by Eq. 3.15. The laser intensity varies from $8.91 \times 10^{13}\mathrm{W/cm^2}$ to $9.96 \times 10^{13}\mathrm{W/cm^2}$. The pronounced enhancement within the re-scattering plateau of the spectrum between 37 eV and 48 eV is clearly visible.

occur. But long pulses lead to long propagation times, and electrons having escaped early within the pulse will propagate outwards very fast. Therefore, large computational grids are needed, if high-order ATI peaks are of interest. It is those that will first hit the boundary of the grid and hence get lost (if masked out) or reflected (and distort the data) if not taken care of.

3.2 Channel Closing Effects in ATI Spectra

Above-threshold ionisation of atoms or molecules by intense laser fields stands for the absorption of more photons than needed to overcome the ionisation threshold. A simple analysis of classical electron trajectories shows that electrons re-scattering once from the core after the initial ionisation step attain final energies up to 10 U_p, while direct (un-scattered) electrons have a maximum energy of 2 U_p, as explained in the previous section. U_p denotes the ponderomotive potential.

A striking phenomenon arises when high-order above-threshold ionisation is studied with respect to its dependence on intensity. For the re-scattering plateau between 2 U_p and 10 U_p, it was found in experiment [32] and calculations [33, 34], that a slight change in laser intensity can lead to order-of-magnitude changes in yield for groups of peaks within the plateau. Explanations were found in terms of multi-photon resonances with Rydberg states [33] and within the framework of quantum paths [35, 36, 37].

The spectral enhancements can be related to channel closings that occur when the (ponderomotively shifted) lowest ATI peak coincides with an effective threshold [35]. See Fig. 3.3 for a calculation. Scanning through a range of laser intensities, for $U_\mathrm{p} = 3.63\ \omega$ the big hump between 37 eV and 48 eV is highest compared to neighbouring laser intensities, differing only by $0.1\ \omega$.

The minimum energy of a free electron in the presence of a laser field is equal to the ponderomotive potential $U_\mathrm{p} = E^2/(4\omega_\mathrm{L}^2) \sim I$, which is the quiver energy of the free oscillating electron. Here, I denotes the intensity of the laser field. Therefore, the laser field modifies the ionisation threshold. In non-resonant n-photon ionisation of an atom, the electron carries the kinetic energy

$$E_\mathrm{kin} = n\,\omega - I_\mathrm{p} - U_\mathrm{p}, \tag{3.10}$$

with integer n. The ionisation potential I_p, in our case of a 2D hydrogen molecule and a laser wavelength of 800 nm, amounts to $I_\mathrm{p} = 10\ \omega$. The system is described by the Hamiltonian given in Eq. 3.12.

The minimum number s of photons needed to free a bound electron is therefore defined through $s = \mathrm{ceil}[(I_\mathrm{p} + U_\mathrm{p})/\omega]$. Raising U_p via the laser intensity and therefore shifting the ionisation threshold to higher photon numbers leads to the disappearance of the first ATI peak in the spectrum. As this happens, a certain s'-photon-channel is closed, which leads to an increased probability of finding the electron near the core [33], since its drift velocity is nearly zero. This situation is favourable for re-scattering and certain groups of peaks within the re-scattering plateau of the ATI spectrum are enhanced. Unfortunately, due to the long-range Coulomb potential, the precise intensity at which this effect takes place cannot be predicted via application of Eq. (3.10) alone [38, 39, 37].

The process is sketched in Fig. 3.4. The red line denotes the ponderomotively shifted (effective) ionisation threshold and is therefore the theoretically predicted start of the ATI spectrum. The tips of the arrows starting at this red line mark the theoretically predicted positions of the ATI peaks. Obviously, if the effective barrier is raised, at some point the first peak will vanish as the corresponding ionisation channel will close.

In [37], the enhancement effect appearing within the re-scattering plateau when raising the laser intensity is explained as constructive interference of long quantum-orbits. An ejected electron is driven in the laser field for several (sometimes many) optical cycles before the system fully ionises. During this time, it may re-scatter with the core many times, although this is not very likely to happen. This motion is calculated via the formalism of complex quantum paths [36] (see also references [15-17] therein), as mentioned in the previous section, where the real part of the quantum path corresponds closely to the classical electron trajectory. Quantum paths belonging to the same final energy of the electron appear in pairs of one long and one short orbit, i.e., they differ in travelling time. For lower energies, more pairs exist, contributing from earlier start times. This explains the general yield drop for high-energy ATI electrons beyond the re-scattering plateau. The maximum energy of $10.007\ U_\mathrm{p}$ can only be reached for electrons re-scattering at their first revisit at the ion core, as was explained in the previous section. The mechanism is, in a reduced form, known as the *simple-man model*. The condition for constructive interference of the long quantum orbits can be shown to be

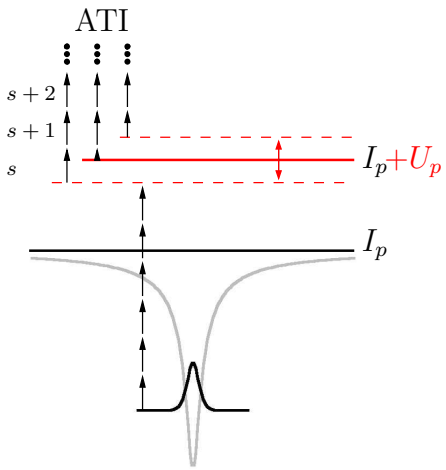

Figure 3.4: Atomic Channel Closing due to varying laser intensity: The ionisation barrier I_p is ponderomotively shifted to $I_\mathrm{p} + U_\mathrm{p}$ via changing the laser intensity. This effective barrier defines the beginning of the continuum and hence the beginning of the ATI kinetic-energy spectrum. Obviously, raising U_p can close ionisation channels as is the case for the s-photon-channel in the picture.

an energy of $I_\mathrm{p} + U_\mathrm{p} = n_c\omega$ for even/odd n_c in the case of an s-state/p-state. If the condition is not met, due to strong wave-packet spreading and hence less re-scattering-probability, the long orbits do not contribute significantly to ionisation with energies within the re-scattering plateau. Two types of enhancements are identified in [37], appearing at even and odd channel closings, respectively. The latter type needs much more quantum orbits to evolve, i.e., much longer pulses of about 50 cycles, therefore they are not expected to be observed within this work. The former type for even channel closings needs about 20-40 orbits corresponding to about 4-8 optical cycles, which is well within the scope of this work. It was however not possible to visualise a clear dependence on the pulse-length within the calculations for this work. Probably, all pulse lenghts considered were not long enough to enter the realm of the second type of channel closing.

Another interpretation of the above-mentioned spectral enhancements is that of threshold phenomena [40, 41], i.e., they are related to threshold anomalies of collision theory when the respective multi-photon reaction channel closes, see [42, 43, 44] (above-threshold detachment of negative ions). Also in this last cited work, a dependence on the orbital angular momentum of the bound electron is found.

Another idea is a that of pure resonances, where field-induced Rydberg states show multi-photon resonances for certain intensities of the laser [45]. The existence of such laser-generated quasi-bound states is questionable in three dimensions though.

Experimentally, this topic was investigated via ATI of argon [46, 47, 48, 38, 29] (where it is particularly pronounced), krypton [29] and xenon [32, 29]. In krypton, the effect is rather small for current experiments, which is accredited to small scattering cross-sections for electrons of the energies in question [29].

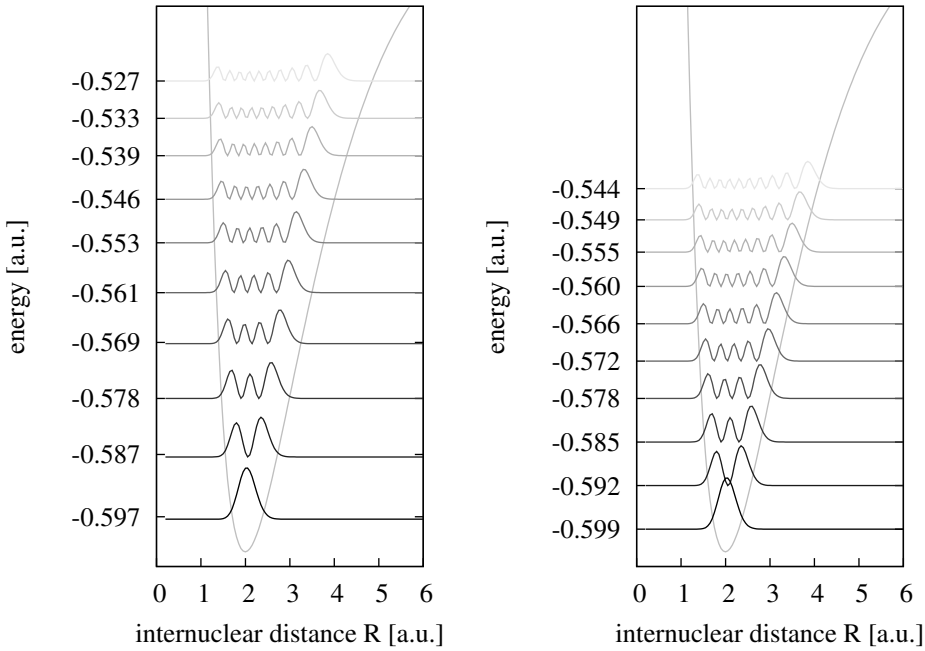

Figure 3.5: Vibrational states $v = 0 \ldots 9$ for $H_2{}^+$ (left panel) and $D_2{}^+$ (right panel) inside the Born-Oppenheimer potential energy surface (PES) for the electronic ground state as calculated. These are exact numerical results and no sketches. The numerically exact vibrational states reside at the correct energies within a correct PES. This already shows the huge difference in density of states that will be exploited in the context of molecular channel closings. The vibrational energies and their separation can also be found in Tab. A.1 in the Appendix.

3.3 Molecular Channel Closing Effects

So far all published work on this effect has been related to *atoms* in laser fields. We found that the vibrational motion of *molecules* can have a striking effect on ATI channel closings. In this work, hydrogen and deuterium molecules are investigated and compared with atoms. Since these simple linear molecules provide a nuclear degree of freedom, an additional energy scale is involved in the dynamics. We show that due to the coupling between electron motion and nuclear motion, *intrinsic* channel-closing effects can be observed: ATI electron spectra decomposed into contributions belonging to different vibrational states of the remaining ion reveal channel-closing effects upon variation of the vibrational quantum number while the laser intensity remains fixed. This is to be contrasted with atoms where the laser intensity (or laser frequency) needs to be varied in order to observe channel closings.

3.3.1 Theoretical Background

In the case of molecules, electrons and nuclei are coupled by their Coulomb interaction so that vibrationally excited states of the ion are occupied after a strong-field ionisation

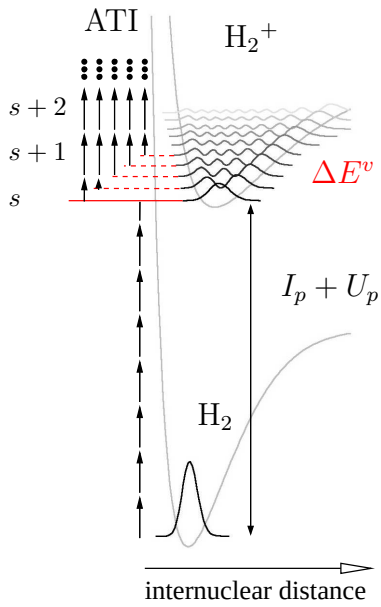

Figure 3.6: Molecular Channel Closing due to different vibrational states of the created ion: For constant laser intensity, H_2 is singly ionised, producing an in general vibrationally excited H_2^+ ion. The ionisation barrier I_p is ponderomotively shifted by U_p, as is the case for atoms, and additionally raised by the vibrational energy ΔE^v of the respective vibrational level, which is transferred from the electron to the ion. Obviously, highly excited ions can lead to a channel closing for the corresponding ionised electron, as is the case for the s-photon-channel in the picture.

process. This amounts to the assumption that Eq. (3.10) is changed to

$$E_\mathrm{kin} = n\,\omega - I_\mathrm{p} - U_\mathrm{p} - \Delta E^v \tag{3.11}$$

for a given vibrational state with quantum number v. Here, $\Delta E^v = E^v - E^0$ is the difference in vibrational energy between the vibrationally excited state in question and the vibrational ground state of the ion. See Fig. 3.5 for a sketch of the vibrational levels of H_2^+ and D_2^+. These states have been computed via imaginary time propagation (see Sec. 2.2) within the one-dimensional BO-potential energy surface of H_2^+ and D_2^+, respectively, also shown in Fig. 3.5. The results for the vibrational energy levels from these calculations can be found in Tab. A.1 in the Appendix.

In this molecular case, it should be noted that I_p is the adiabatic ionisation potential, i.e., the difference between the ground-state energies of molecule and ion, including the motion of the nuclei. The process is sketched in Fig. 3.6. The laser intensity is kept fixed, but the vibrational states of the corresponding ions provide a second energy scale coupled to the electronic motion. This means the effective ionisation potential of a photo electron is defined by the laser intensity and additionally the vibrational state of the corresponding ion. Highly excited ions will therefore close the lower ionisation channels.

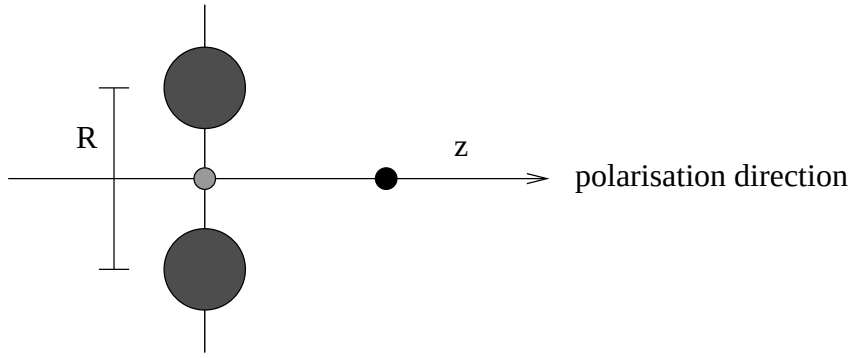

Figure 3.7: Particle setup for the model molecule: The active electron (black dot) moves along the laser polarisation direction (z-axis), while the protons (big grey dots) vibrate orthogonally to this. The coordinate R represents the proton separation. The second electron (bright grey dot) drawn in between the two protons is inactive within this model and does not couple to the laser field nor interact directly with the active electron. It is represented as a screening charge only, staying in the electronic ground state for all times.

3.3.2 Numerical model

We model the H_2 (or D_2) molecule as composed of a single active electron interacting with the core which is allowed to vibrate. This is justified by the fact that no qualitative influence of electron-electron correlation on ATI spectra has been found so far. Both degrees of freedom (electron coordinate and inter-nuclear distance) are treated only in one dimension, since for strong, short laser pulses, the electron is essentially driven along the laser field and the timescale for rotational motion of the whole molecule is much longer than the ultrashort pulse durations considered here.

The alignment of the molecular axis was chosen orthogonal to the laser polarisation direction. This removes the dipole coupling between the ground and first excited state of the ion [49, 50] and allows the ion to be vibrationally excited to very high v without dissociation through bond softening. This results from the fact that the electronic ground state of $H_2{}^+$ is composed as a symmetric linear combination of two $1s$ atomic orbitals and therefore a $1s\sigma_g$ state, hence *gerade*. The first exited molecular state is the antisymmetric linear combination of these two atomic orbitals, leading to a $2p\sigma_u$ state, i.e., it is *ungerade*. Now obviously, a laser dipole in direction of the molecular axis is an ungerade function of the space coordinate along this axis. Therefore, $\langle 2p\sigma_u|z|1s\sigma_g\rangle \neq 0$ in general. If the molecular axis is perpendicular to the laser dipole instead, the overlap integral between gerade and ungerade will vanish, $\langle 2p\sigma_u|x|1s\sigma_g\rangle = 0$. Hence, almost no probability is transferred to the dissociating $2p\sigma_u$ state and the electronic ground state is populated with highly excited vibrational states instead. A sketch of the particle setup is given in Fig. 3.7.

This setup leads to the Hamiltonian

$$\begin{aligned}\widehat{H}(t) = &-\frac{1}{2}\left(\frac{1}{\mu_\mathrm{n}}\frac{\mathrm{d}^2}{\mathrm{d}R^2}+\frac{1}{\mu_\mathrm{e}}\frac{\mathrm{d}^2}{\mathrm{d}z^2}\right)\\ &+V_\mathrm{n}(R)+V_\mathrm{int}(z,R)+E(t)z,\end{aligned} \tag{3.12}$$

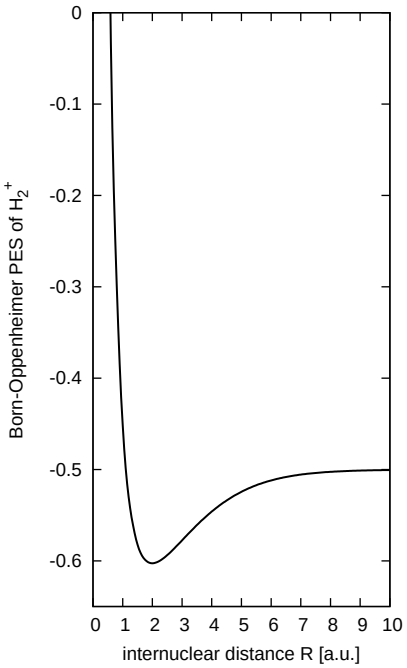

Figure 3.8: Ground state potential energy surface of $H_2{}^+$. It is identical for $D_2{}^+$.

where the operator $E(t)z$ with $E(t) = F(t)F_0 \sin(\omega t)$ describes the interaction of the active electron with the electric field of a linearly polarised laser pulse in length gauge. F_0 is the maximum field amplitude and $F(t)$ defines the pulse shape. The electron coordinate and inter-nuclear distance are denoted by z and R; μ_e and μ_n denote the reduced masses of the active electron and of the two nuclei, respectively. The repelling nuclei are screened by the second (inactive) electron, which we assume to remain always in the energetically lowest possible state. The inter-nuclear potential is thus taken to be the exact Born-Oppenheimer ground-state potential of the molecular ion,

$$V_\mathrm{n}(R) = V_\mathrm{BO}^{\mathrm{H_2}^+}(R), \tag{3.13}$$

shown in Fig. 3.8, which is of course identical for $D_2{}^+$. The electron-ion interaction is modelled via the soft-core potential

$$V_\mathrm{int}(z,R) = -\frac{1}{\sqrt{z^2+\sigma^2(R)}}, \tag{3.14}$$

shown in Fig. 3.10, upper plot. This choice expresses that since the electron moves perpendicular to the nuclei, there is only one single Coulomb well, whose strength is dependent on the inter-nuclear separation and the screening. The parameter $\sigma(R)$ (see Fig. 3.9) is adjusted such that the Born-Oppenheimer ground-state potential of the model Hamiltonian matches the exact Born-Oppenheimer ground-state potential of H_2 given in [51]. The shape of the parameter curve for $\sigma(R)$ is perfectly translated into the interaction potential. In the limit of large R, σ tends towards $\sqrt{2}$, such that σ^2 gives the correct soft-core parameter for separated hydrogen atoms. The full potential

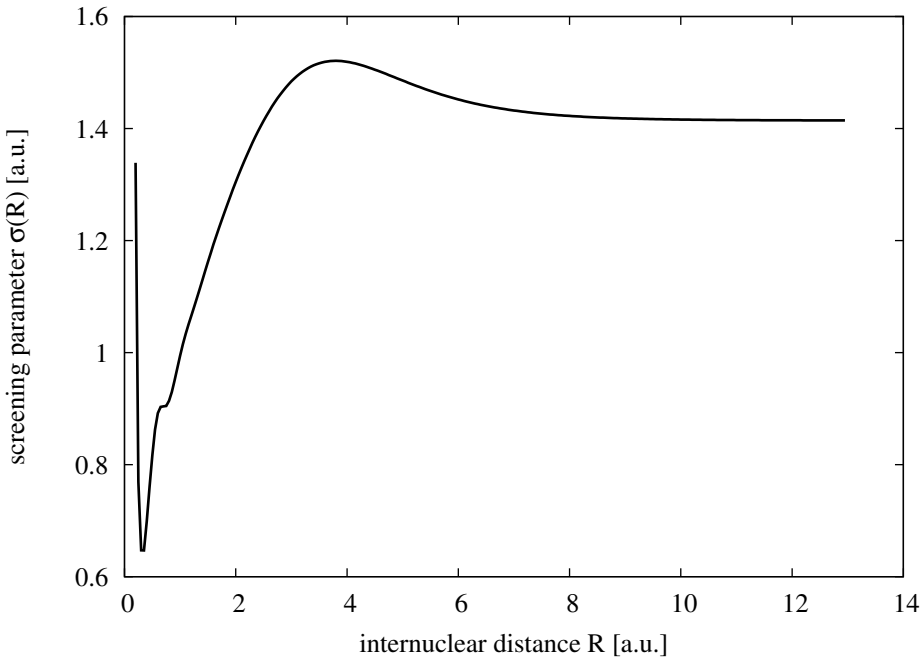

Figure 3.9: The screening length $\sigma(R)$ appearing in the electro-nuclear interaction potential $V_{\text{int}}(z, R)$. It is fitted such that the Born-Oppenheimer ground-state potential of the model Hamiltonian for each R exactly matches the Born-Oppenheimer ground state potential of H_2 and D_2.

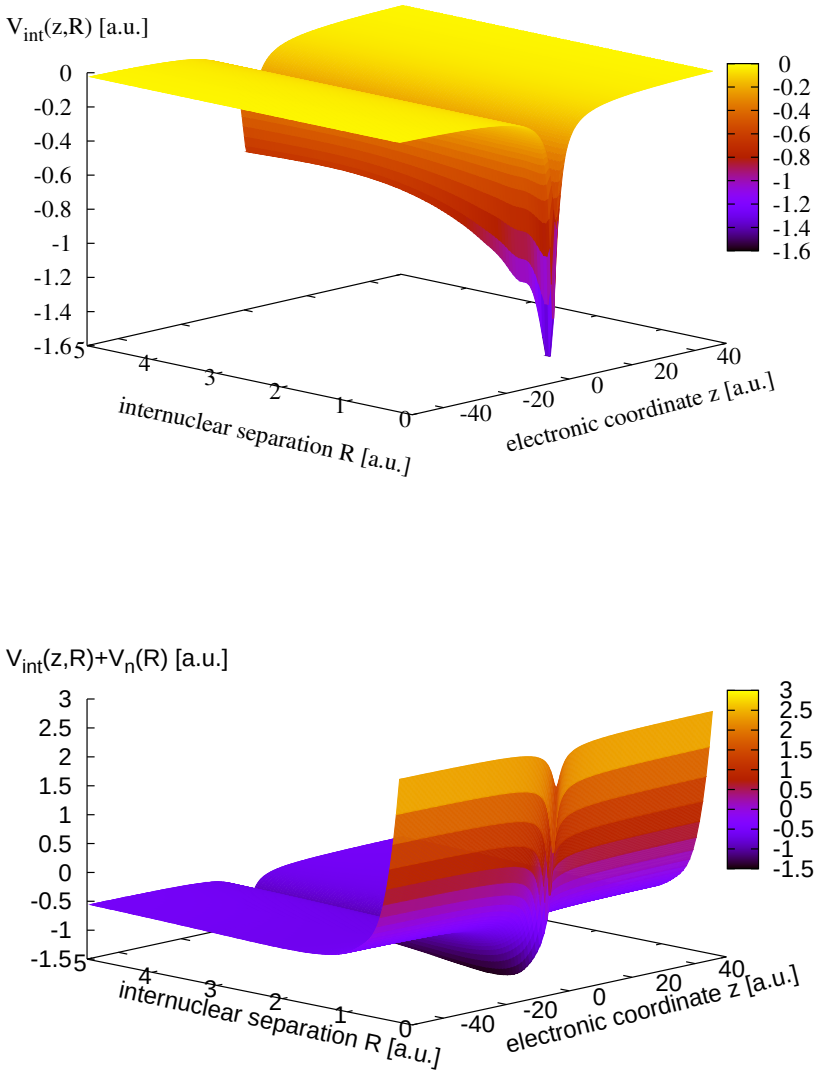

Figure 3.10: Interaction potential between active electron and model H_2^+/D_2^+, without (upper panel) and with (lower panel) nuclear repulsion included.

$V_{\text{int}}(z,R) + V_n(R)$ is shown in Fig. 3.10, lower plot. Through the combination of both components, it exhibits an absolute minimum at $R = 1.2$ a.u. for $z = 0$. The average binding length is 1.45 a.u. (1.43 a.u.) for H_2 (D_2). The ground states of both systems H_2 and D_2 are shown in Fig. 3.11.

In interpreting the fit, it helps to imagine a 2D Coulomb potential. A fixed soft-core parameter would describe the offset with which one would have to fly by the Coulomb centre. The potential along the path gives exactly the soft-core potential. If the soft-core parameter is varying with R, the line path simply shifts closer to or further away from the Coulomb centre. The soft-core parameter for the correct ground-state energy of a hydrogen atom is exactly 2, matching perfectly with the σ-fit.

A similar fitting procedure has been used previously to reproduce the Born-Oppenheimer potential of $H_2{}^+$ in a 1D model [52].

Obviously, this model allows only for single ionisation of the molecule. There is no dissociation channel included, and the second electron is completely passive in its ground state. No interaction between the two electrons in taken into account and hence no energy is transferred between the electrons. This is surely a severe simplification, yet it was the only numerically feasible one and still shows interesting and important features stemming from the coupling between electronic and nuclear motion.

For comparison, we also carry out calculations for a 1D atom. The atomic Hamiltonian reads

$$\widehat{H}_{\text{atom}}(t) = -\frac{1}{2\mu_e}\frac{\mathrm{d}^2}{\mathrm{d}z^2} + V_{\text{int}}(z) + E(t)z, \tag{3.15}$$

where the Coulomb interaction between electron and nucleus was modelled as a simple soft-core potential,

$$V_{\text{int}}(z) = \frac{1}{\sqrt{z^2 + a}}. \tag{3.16}$$

The soft-core parameter was adjusted to $a = 1.4863$, such that the ionisation potential I_{p} of the atom equals the one for H_2.

To simulate the system constructed above, the 2D Time-Dependent Schrödinger Equation

$$i\frac{\partial}{\partial t}\Psi(z,R,t) = \widehat{H}(z,R,t)\Psi(z,R,t) \tag{3.17}$$

is solved numerically. The 2D wave function $\Psi(z,R,t)$ is propagated via the split-operator method combined with 2D Fourier transformations, as is explained in Section 2.2. The two-dimensional grid (z-spacing 0.36 a.u., R-spacing 0.05 a.u.) extends in R-direction from 0.2 a.u. to 12.95 a.u., in electronic direction from -276.3 a.u. to 276.3 a.u., corresponding to 256 and 1536 grid points, respectively. In the electronic dimension, the grid is further extended up to $|z| = 2522.7$ a.u. to allow for the possibility of large electronic excursions and to obtain high-resolution energy spectra for the ATI electrons. This is done via splitting the grid and wave function [15], see sections 2.8 and 2.9: in the overlap region between inner and outer grid, we decompose the 2D wave function $\Psi_{\text{out}}(z,R,t)$ repeatedly into a single sum of product states,

$$\Psi_{\text{out}}(z,R,t) = \sum_j \xi_j(z,t)\zeta_j(R,t), \tag{3.18}$$

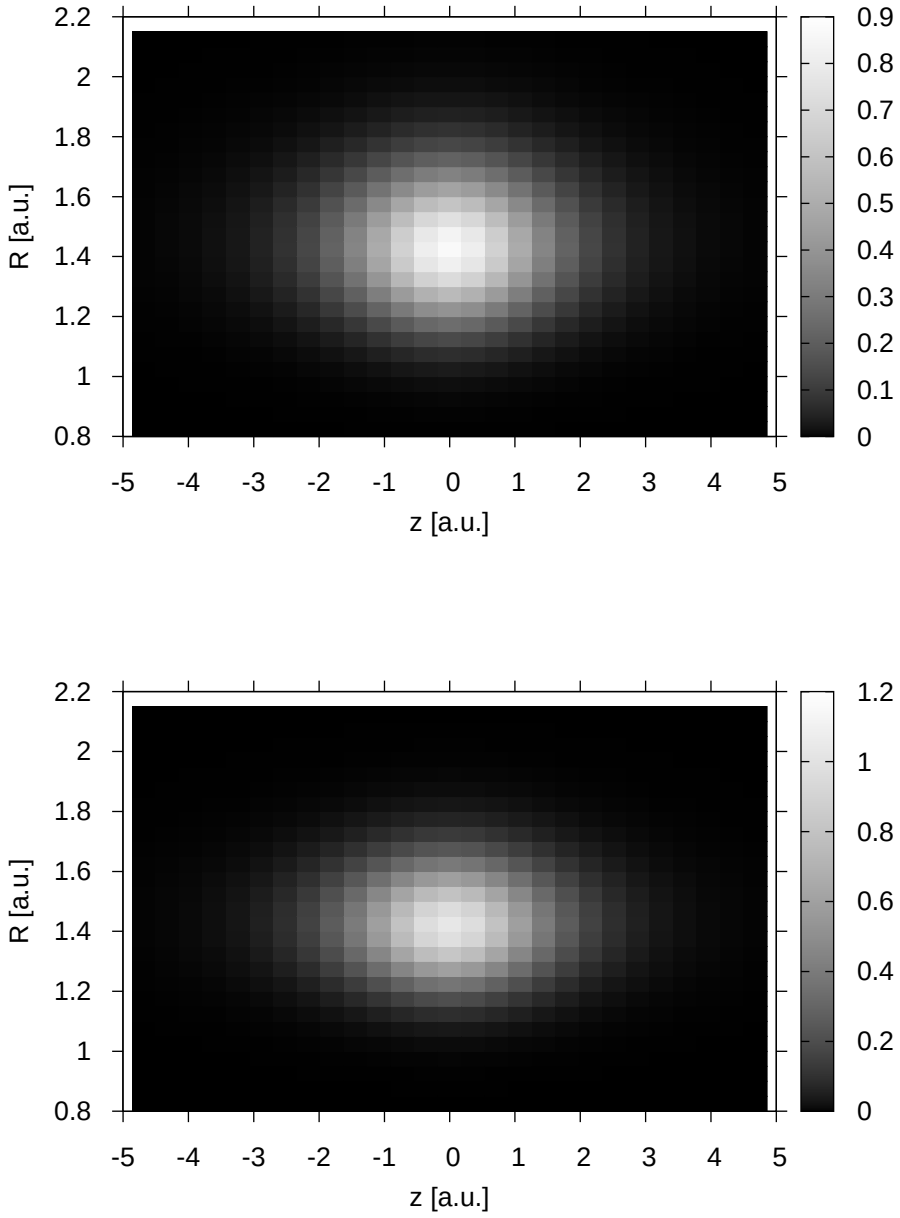

Figure 3.11: Numerically calculated ground-state wave functions of the model H_2 (upper plot) and D_2 (lower plot) molecule. The wave function was calculated via the imaginary time propagation technique explained in Section 2.2. The ground-state energies come out as $E_0^{H_2} = -1.164536$ a.u. and $E_0^{D_2} = -1.167439$ a.u., respectively.

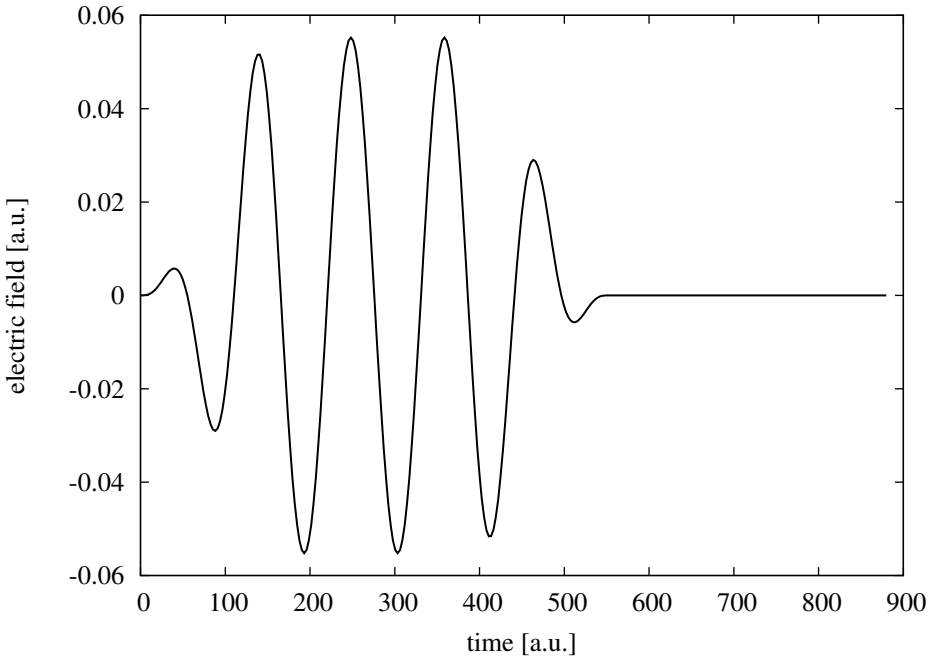

Figure 3.12: Pulse shape used within the calculations: It extends over five optical cycles, while ramped on and off with a $\sin^2$-shaped ramp extending over 1.5 cycles. Three cycles with zero electric field are appended to let outgoing photoelectrons move into regions of small Coulomb potential. The time integral over the electric field vanishes exactly by construction.

where $\xi_j(z,t)$ and $\zeta_j(R,t)$ are the canonical basis states or natural orbitals. We chose the number of expansion terms such that all terms add up to a probability of at least 0.999. No more than four terms were needed in each expansion.

In the outer part of the 2D grid, the coupling between the two degrees of freedom is neglected: the interaction potential $V_{\text{int}}(z,R)$ is replaced by the R-independent potential $V_{\text{out}}(z) = V_{\text{int}}(z, R = 2)$. This allows us to apply 1D propagations separately to the functions $\xi_j(z,t)$ and $\zeta_j(R,t)$, and grid extensions up to several thousands atomic units become feasible. The potential is gradually changed between $|z| = 10 \ldots 161$ a.u. from V_{int} to V_{out} to avoid discontinuities of the Hamiltonian.

For the atomic calculation, a 1D grid with no grid splitting was applied. We used the same electronic grid spacing and applied the same propagation scheme.

The pulse shape $F(t)$ is chosen such that the temporal pulse integral vanishes. The five-cycle pulses used in this work are ramped on and off following a $\sin^2$ envelope over 1.5 cycles and have a mid plateau with constant intensity that extends over two cycles. Three cycles without laser field are added to let the ejected electrons move further away from the Coulomb potential of the core. The pulse is shown in Fig. 3.12. We have checked that finally no significant Coulomb energy is carried by the ATI electrons considered in this work. For small electronic energies usually corresponding to electrons close to the nuclear core, see Chapter 4 for an advanced technique to avoid Coulomb shifts of ATI peaks through application of the Wigner Distribution Function.

The laser wavelength is 800 nm, hence $\omega = 0.05695$ a.u., so that we have $I_\mathrm{p} = 10.0\,\omega$ for all three systems considered. The system is regarded as ionised for $|z| > 30$ a.u. The precise choice of this value is not important for the investigation of the channel-closing effects since the corresponding results shown in this work involve electrons driven at least 500 a.u. from the ion at the end of the simulation. It only means that the part of the computational grid used for analysis corresponds to electrons at least 30 a.u. away from the nuclear core. In the last part of this work, dealing with Coulomb shifts of kinetic energy spectra, also near electrons play a role.

The time step was chosen as $\delta t = 0.0276$ a.u. which corresponds to 4000 time steps per laser cycle.

3.3.3 Results

The kinetic-energy spectra of ATI electrons are analysed into contributions corresponding to different vibrational states v of the remaining ion. This is done via projection of the ionised part Ψ_ion (i.e., where $|z| > 30$ a.u., see above) of the wave function at the end of the simulation onto the different vibrational states χ_v of the ion,

$$\phi_v(z) = \int \chi_v^*(R)\,\Psi_\mathrm{ion}(z, R, t_\mathrm{end})\,\mathrm{d}R. \tag{3.19}$$

The modulus squared, $|\widetilde{\phi}_v(p_z)|^2$, of the Fourier transform then gives the momentum power spectrum. This is then further rescaled from momentum to energy by weighting the respective contributions for each momentum $p = \pm\sqrt{2mE}$ with

$$\left|\frac{\mathrm{d}p}{\mathrm{d}E}\right| = \sqrt{\frac{m}{2E}}, \tag{3.20}$$

since the momentum distribution $\widetilde{f}(p)$ and the energy distribution $f(E)$ are related by

$$\widetilde{f}(p)\mathrm{d}p = f(E)\mathrm{d}E = \widetilde{f}(p(E))\left|\frac{\mathrm{d}p}{\mathrm{d}E}\right|\mathrm{d}E, \tag{3.21}$$

where the function $f(E)$ contains only the positive or only the negative momenta. In this way we obtain one ATI spectrum for each vibrational state. In this work, Ψ_ion is chosen such that it contains only the right-going part of the final wave function.

According to Eq. (3.11), the ATI peaks in these spectra are shifted by ΔE^v. Scanning through different v and thus varying ΔE^v can therefore lead to channel closings. Since ΔE^v can easily exceed the photon energy within the first few vibrational states (for the $H_2{}^+$ ion and $\lambda = 800$ nm, $\Delta E^7 \approx 1.0\,\omega$ and for the $D_2{}^+$ ion, $\Delta E^9 \approx 0.96\,\omega$), a channel closing will almost certainly be observed within the first nine vibrational states, no matter where exactly the first ATI peak is located.[3] So instead of scanning through different laser intensities, in the case of molecules one can also "scan" through different vibrational states of the remaining ion. With growing quantum number v the vibrational energy gets larger, so at some v, the lowest-possible channel is closed, and we expect the corresponding energy spectrum to show the characteristic channel-closing

[3] Of course, depending on the exact situation, it can be an even-n or an odd-n channel-closing, which are not equally well observable.

features known from atoms. The difference to atoms is that the energy is scanned in discrete steps of hard-wired, non-equidistant size. We compare ionisation of H_2 and D_2. In the case of $D_2{}^+$ ions, the closer-lying vibrational states allow for a less coarse scanning in energy already for low vibrational states, and we expect a clearer resolution of the observed features as compared to $H_2{}^+$.

Intensity-Dependent Channel Closings

Strong-field single ionisation by a laser field of suitable intensity leads to a channel closing according to Eqs. (3.10) and (3.11). In Fig. 3.13, ATI electron spectra are shown for ionisation of the three model systems under investigation: atom, molecular hydrogen and molecular deuterium (top to bottom). In the latter two cases, projections onto the $v = 4$ vibrational state of the molecular ion are taken. In each case, two different intensities are plotted, with 0.4 ω difference in U_p. The two corresponding curves are vertically shifted with respect to each other to enhance visibility. For each species, the upper curve (lower intensity) shows a dip in the re-scattering plateau (located before the final big hump), while the lower curve shows the maximum yield in the re-scattering plateau within the intensity range under investigation. Clearly, the enhancement effect known from atoms (upper panel) can be identified for the case of molecules as well. The full molecular spectra (the sum over contributions from all v, shown in Fig. 3.14) do not as clearly show the effect, because the channel-closing intensity depends on the vibrational state. In the projections on individual vibrational states, Fig. 3.13, the effect is clearly visible. However, depending on the distribution of vibrational states, in general there will be one major contribution to the total spectrum by one specific v, which is then responsible for a noticeable enhancement even in the complete spectrum. A hint of this is visible in Fig. 3.14.

Applying Eqs. (3.10) and (3.11), the channel closing is expected at intensities 7.89×10^{13} W/cm^2 ($n = 13$) or 1.05×10^{14} W/cm^2 ($n = 14$) for the atom, 8.82×10^{13} W/cm^2 for H_2 and 9.19×10^{13} W/cm^2 for D_2 (ionic state $v = 4$ and $n = 14$ in both cases). As known from earlier publications, this does not exactly match the observation, i.e., the concept of energy conservation alone cannot explain the effect quantitatively. Due to the different vibrational energies in hydrogen and deuterium, according to Eq. (3.11) it is expected that in case of D_2 more laser intensity is needed for the channel closing to take place. For $v = 4$, the difference in ΔE^4 amounts to 0.17 ω, which would have to be compensated by a correspondingly higher U_p. In fact, the maximum enhancement for D_2 is found at a higher intensity with a value of U_p higher by 0.1 ω. (Note that U_p was sampled in steps of 0.1 ω.)

Molecular Channel Closings

In Fig. 3.15, envelopes of ATI spectra are plotted for molecular hydrogen and molecular deuterium. Several different projections on vibrational states of the ion are shown, such that in both cases approximately the same range of vibrational energy is covered, namely about one laser photon energy. The laser intensity is fixed at 9.435×10^{13} W/cm^2, and the variation in vibrational energy ΔE^v plays the role of the changing laser intensity in the case of Fig. 3.13. According to Eq. (3.11), again a channel closing takes place. The resulting effect is visible in both H_2 and D_2. Yet it is masked

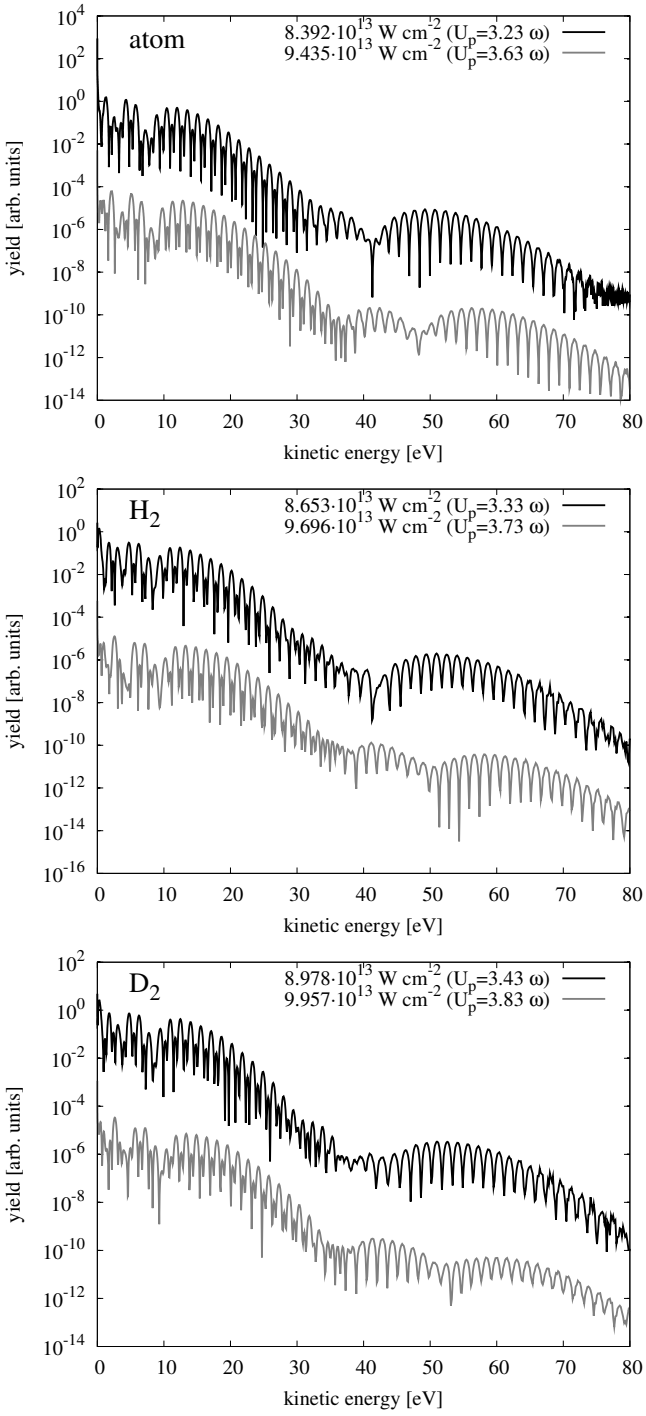

Figure 3.13: Kinetic-energy spectra of (right-going) ATI electrons in the case of the 1D atom (upper panel), H_2 (central panel), and D_2 (lower panel). For the molecular cases, the $v = 4$ projection is shown. Two different laser intensities are plotted in each case to visualise the intensity-dependent enhancement of the re-scattering plateau. In each panel, one of the two spectra has been vertically shifted by a factor of 5×10^4 to improve readability.

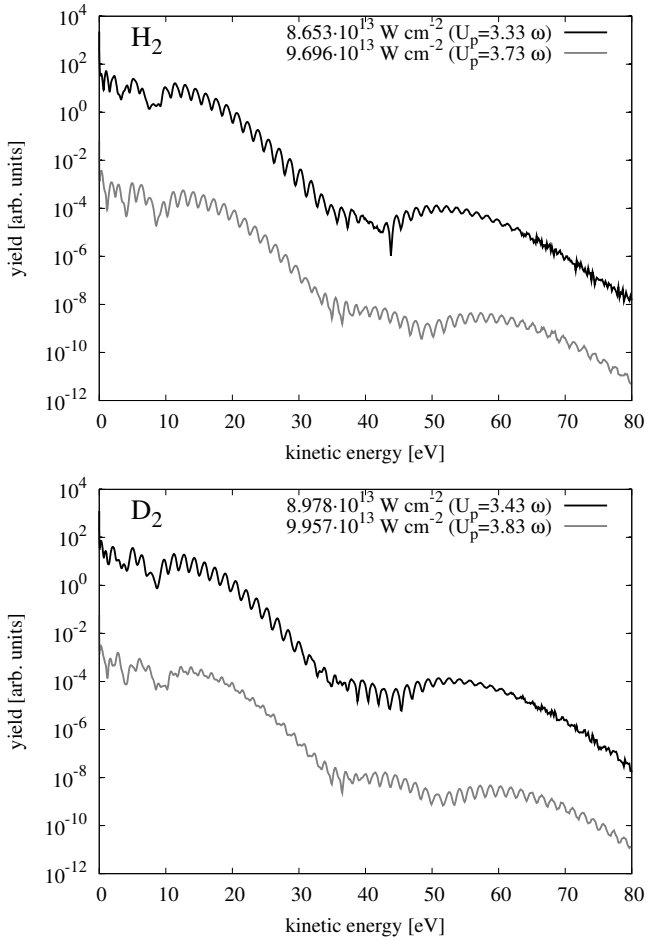

Figure 3.14: Kinetic-energy spectra of (right-going) ATI electrons in the H_2 (upper panel) and D_2 (lower panel). In both cases, the full spectrum (integrated over all vibrational levels) is shown. Two different laser intensities are plotted in each case to visualise the intensity-dependent enhancement of the re-scattering plateau. In each panel, one of the two spectra has been vertically shifted by a factor of 5×10^4 to improve readability.

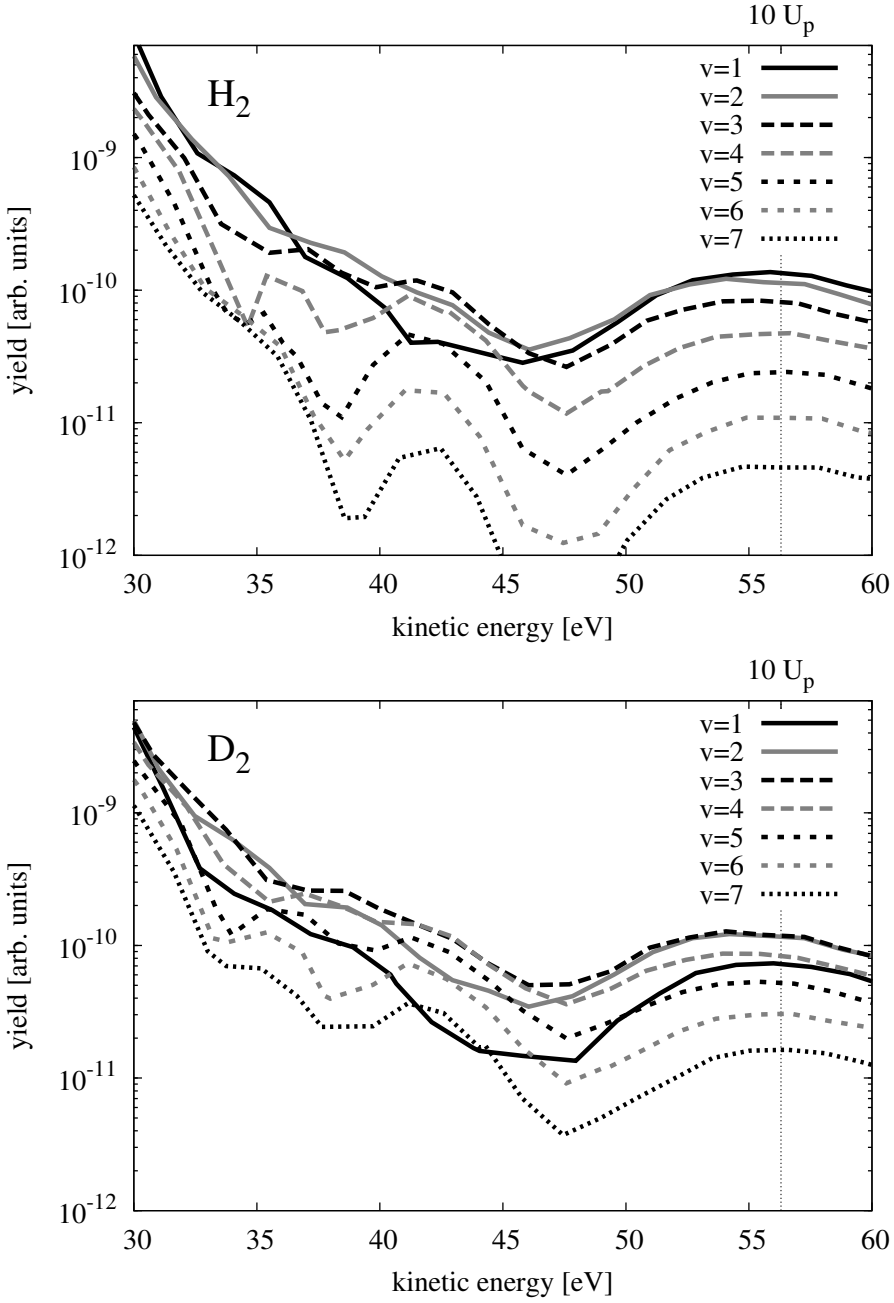

Figure 3.15: Envelopes of kinetic-energy spectra of (right-going) ATI electrons in the case of H_2 (upper panel), and D_2 (lower panel). The laser intensity is 9.435×10^{13} W/cm^2 ($U_p = 3.63\ \omega$). Projections on several different vibrational states of the remaining ion are plotted to show the intrinsic channel-closing effect. Plotted are absolute spectra without any normalisation, therefore the trend of Fig. 3.16 is reflected, but quantitatively masked by the general trend of different occupations of the different vibrational states.

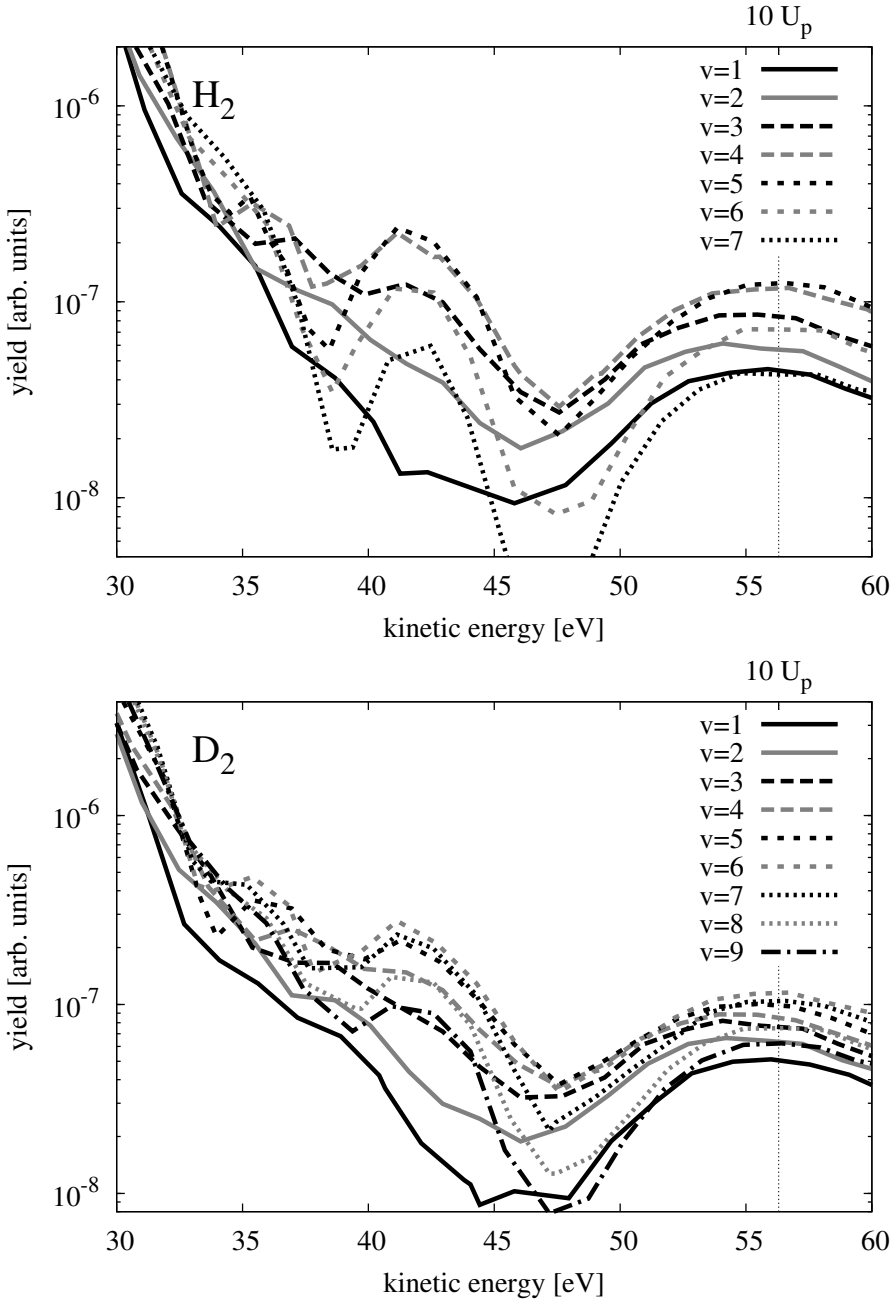

Figure 3.16: Envelopes of kinetic-energy spectra of (right-going) ATI electrons in the case of H_2 (upper panel), and D_2 (lower panel). The laser intensity is 9.435×10^{13} W/cm^2 ($U_p = 3.63\ \omega$). Projections on several different vibrational states of the remaining ion are plotted to show the intrinsic channel-closing effect. Each spectrum has been divided by the total yield of the respective vibrational state to clearly isolate the channel-closing effect from the v-dependence of the total yield.

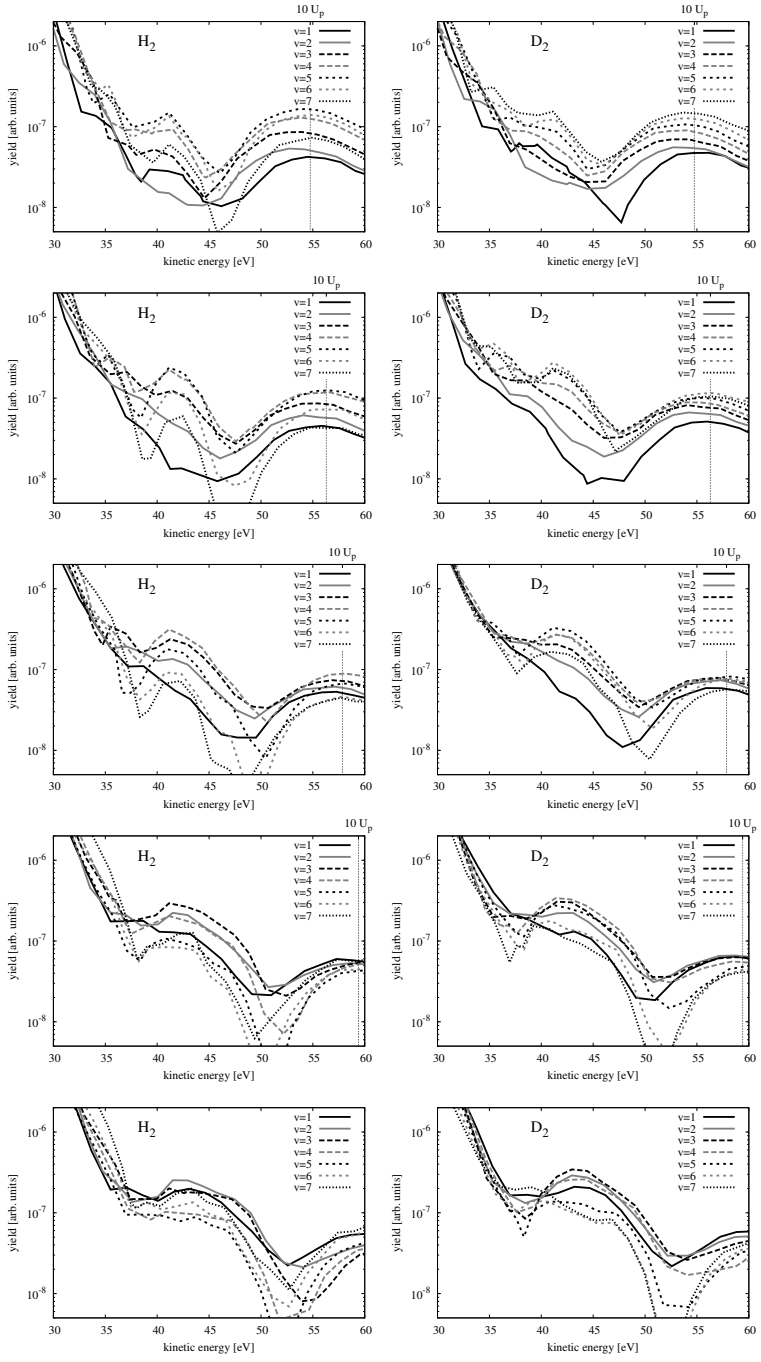

Figure 3.17: Envelopes of kinetic-energy spectra of (right-going) ATI electrons in the case of H_2 (left column), and D_2 (right column). The laser intensity is grows from $U_p = 3.53\ \omega$ (top row) to $U_p = 3.93\ \omega$ (bottom row). Projections on vibrational states 1 to 7 of the remaining ion are plotted to show the intrinsic channel-closing effect. Each spectrum has been divided by the total yield of the respective vibrational state to clearly isolate the channel-closing effect from the v-dependence of the total yield.

by a general trend prescribed by the vibrational state distribution. For example, in the top-left panel of Fig. 3.18, which shows the total distribution of vibrational states for the same laser intensity as in Figures 3.15 and 3.16, the population decreases quickly as a function of v around $v = 4$.

To avoid confusion of the channel-closing effect with changes due to higher or lower total occupation of vibrational states, the spectra have been normalised, i.e., divided by the total yield of the respective vibrational state. The result is shown in Fig. 3.16. For the case of H_2, it is obvious from Fig. 3.16 (upper panel) that the highest yield is found for the $v = 4$ and $v = 5$ projections, i.e, the channel closing occurs somewhere between these two vibrational energies. For D_2, the highest yield is clearly reached for $v = 6$, maybe a little later, as the $v = 7$ curve is still quite close by. This fits perfectly the relative comparison in energy conservation, since $\Delta E^4_{H_2{}^+} = 0.64\ \omega$ and $\Delta E^5_{H_2{}^+} = 0.78\ \omega$, whilst $\Delta E^6_{D_2{}^+} = 0.68\ \omega$ and $\Delta E^7_{D_2{}^+} = 0.78\ \omega$. A coarse estimation, supported by both examples, would suggest that the vibrational energy needed for an exact closing is about $0.7\ \omega$.

To support the findings, the same plots were made for different laser intensities ranging from $U_p = 3.53\ \omega$ to $U_p = 3.93\ \omega$ (top to bottom) in Fig. 3.17. The left column shows the results for H_2, the right column those for D_2. The second row of the figure shows exactly the situation of Fig. 3.16. One clearly sees for both cases of H_2 and D_2 that with growing laser intensity (top to bottom) the highest yield is reached for lower and lower vibrational states of the ion. This matches perfectly the expected trend due to energy conservation. In the case of D_2 it is especially beautiful, since for each $0.1\ \omega$-step in U_p the maximum is reached exactly one v earlier. This matches perfectly the spacings of the vibrational states 1 to 7 in $D_2{}^+$, given by $0.12\ \omega$, $0.12\ \omega$, $0.11\ \omega$, $0.11\ \omega$, $0.10\ \omega$, and $0.10\ \omega$ respectively.

In any case, H_2 and D_2 exhibit a clear difference in the behaviour of the plateau enhancement, namely with changing v, it happens much more slowly in the D_2 case as compared to H_2, again supporting the connection to the concept of energy conservation. Yet the application of Eq. (3.11) predicts the channel closing at $\Delta E^v \approx 0.37\ \omega$, which does obviously not quantitatively match the observation. Vibrational energies and their separations are also given in Tab. A.1 in the Appendix. There, also the theoretically predicted channel closings for $n = 14$ in terms of U_p are shown.

Correlation Effects

In Fig. 3.18, the population of vibrational states $v = 0$ to $v = 9$ is plotted for the cases of H_2 (left column) and D_2 (right column) after ionisation with a laser intensity of 9.435×10^{13} W/cm^2. From top to bottom, different energy windows have been applied to the corresponding ATI electrons. The two upper panels show the total vibrational distribution of the produced ions for all right-going electrons. In the lower four panels, yields within restricted electron energy windows are shown. Here, the bars show unnormalised distributions, i.e., the underlying ATI spectra have not been normalised. In the background of the topmost panels, for comparison the Franck-Condon distributions are shown in grey for both cases. They correspond to a "vertical" transition between molecule and ion, i.e., it is assumed that the nuclear configuration does not change while the molecule is ionising. The nuclear H_2 wave packet is transferred onto

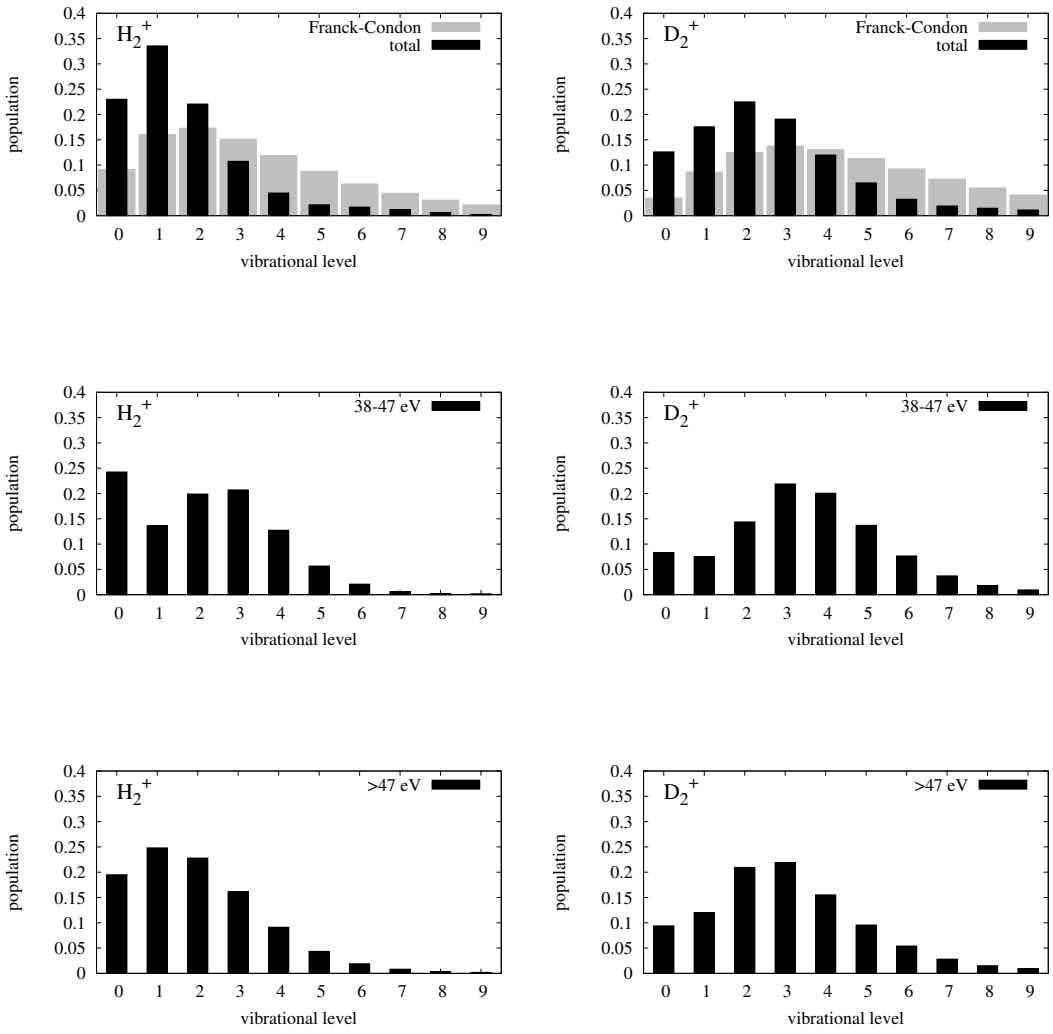

Figure 3.18: Occupation of vibrational states of $H_2{}^+$ (left column) and $D_2{}^+$ (right column) after single ionisation of the respective molecule with laser intensity 9.435×10^{13} W/cm^2 ($U_\mathrm{p} = 3.63\ \omega$). Three cases are shown: including all ATI electrons (upper two panels), including only electrons with kinetic energies between 38 and 47 eV (two central panels), and including only electrons with more than 47 eV (lower two panels). The uppermost panels show in grey the Franck-Condon distribution for comparison.

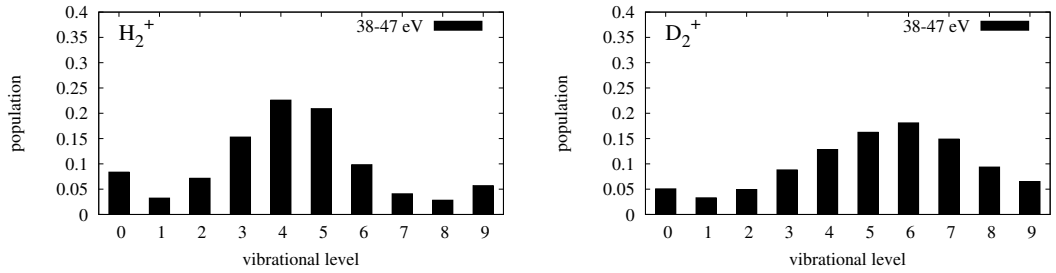

Figure 3.19: Occupation of vibrational states of $H_2{}^+$ (left panel) and $D_2{}^+$ (right panel) after single ionisation of the respective molecule with laser intensity 9.435×10^{13} W/cm^2 ($U_\mathrm{p} = 3.63\ \omega$) including ATI electrons with kinetic energies between 38 and 47 eV. The bars show normalised distributions, i.e, the full spectrum was divided by the total yield of the respective vibrational states (i.e. these distributions belong to the envelopes shown in Fig. 3.16).

the $H_2{}^+$ PES immediately, without changing shape. This leads to a significant population of vibrationally excited states, since the nuclear H_2 ground-state wave packet is no stationary state of the ionic PES. The Franck-Condon factors represent the overlap of the H_2 ground-state nuclear wave function with the vibrational states of $H_2{}^+$, $\int\langle\chi_v^{H_2{}^+}(R)|\Psi_0^{H_2}(z,R)\rangle\mathrm{d}z$.

If one restricts the spectra to ATI electrons with kinetic energy in a certain interval, e.g. between 38 eV and 47 eV in the middle panel of Fig. 3.18, the distribution of vibrational states is very different from the total distribution. It is significantly warmer, i.e., the maximum and average are shifted towards higher v, especially for the case of $D_2{}^+$. Since the chosen energy window matches the re-scattering plateau of the ATI spectrum, the distributions show that for re-scattered electrons higher vibrational excitation of the corresponding ion is favoured. In the lower two panels, ATI electrons with energies above 47 eV are chosen. The corresponding distribution of vibrational states changes again. The distributions resemble more the total distributions shown in the uppermost panel.

For comparison, the bars of Fig. 3.19 correspond to the spectra of Fig. 3.16 and therefore belong to normalised spectra, i.e., the yield for each vibrational state has been divided by the total yield of the vibrational state. In other words, if the yield falling within the chosen electron energy window followed the same dependence on v as the total yield (upper panel of Fig. 3.18), then this normalised distribution would be constant. Instead, one clearly sees a preference of highly excited vibrational states, exactly matching the observation of maximum enhancement within Fig. 3.16 as expected.

For the present laser intensity, the windowed electrons (which lie in the re-scattering plateau) give comparatively hot vibrational distributions, while the lower vibrational states are mainly found as partners of *direct* electrons. Generally speaking, a strong correlation between the kinetic energy of the ATI electrons and the vibrational state of

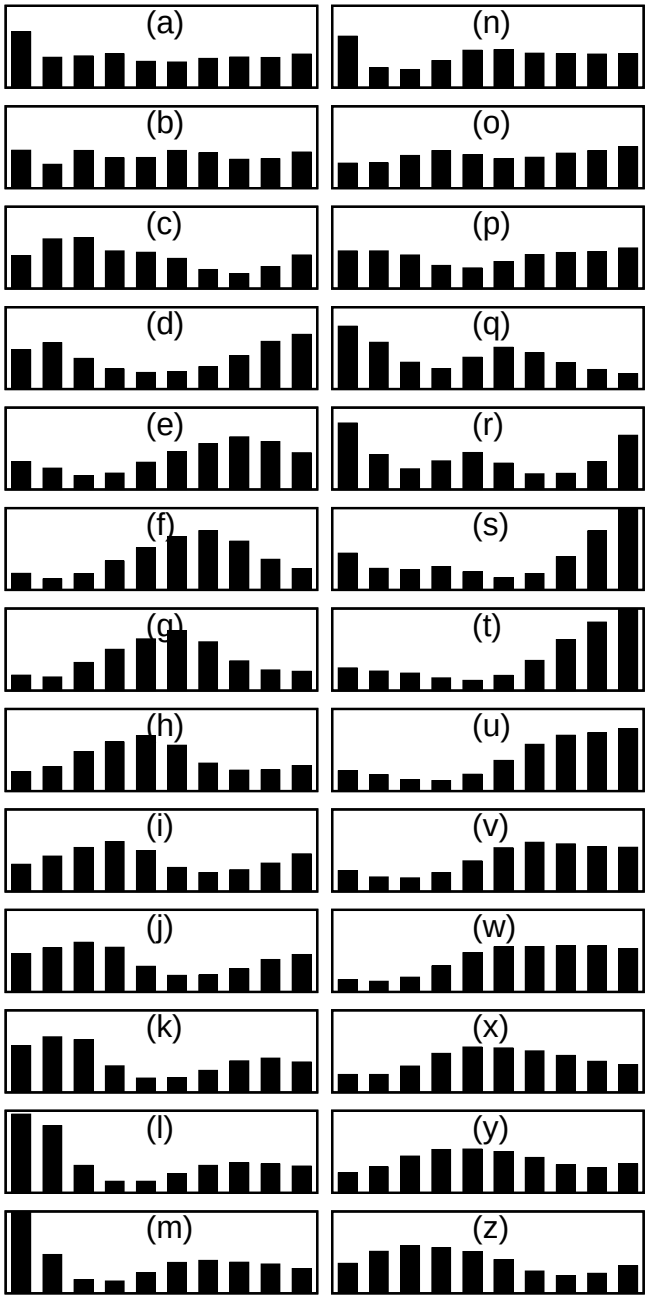

Figure 3.20: Normalised distribution of vibrational states 0 to 9 (black bars from left to right), of $D_2{}^+$ within energy window corresponding to the respective enhancement region within the re-scattering plateau; laser intensities growing alphabetically, reaching from $U_p = 3.13\ \omega$ to $U_p = 5.63\ \omega$ in steps of $0.1\ \omega$.

the corresponding ion is obvious from these results.

Again, this behaviour is counter-checked for different laser intensities, plotted in Fig. 3.20 for D_2^+. The figure is extremely simplified to just sketch the general trend of the distribution. It is identical to the plots of Fig. 3.19, where the D_2^+ plot can be found in Fig. 3.20 at position (f) in the left column. We will use this plot corresponding to a laser intensity of $U_p = 3.63\ \omega$ as a starting point for further discussions.

Obviously, changing laser intensity leads to a shift of the maximum within the distribution. For lower intensities (a)-(e), the maximum "leaves" the plot, i.e., it is shifted to higher vibrational states, while a "new" maximum seems to enter the plot from the left. The concept of energy conservation explains this qualitatively, since a lower U_p can be compensated by a higher vibrational energy. Hence, the same structures appear at higher ΔE^v. This is in perfect agreement with what is seen in Fig. 3.17, where for lower laser intensity the highest yield is observed for higher-lying vibrational states.

The energy conservation formula (3.11) would also suggest that the maxima be separated by a vibrational energy of exactly 1.0 ω. Unfortunately, in D_2^+, $\Delta E^9 = 0.96\ \omega$. Therefore only the extreme case of the two maxima residing exactly at the two borders of the plot in $v = 0$ and $v = 9$ should be visible. For the two lowest laser intensities (a) and (b), there is obviously not enough structure within the re-scattering plateau to produce a distribution of vibrational states significantly different from the general trend.

For higher intensities as compared to plot (f), all the way down to the bottom of the left column, the maximum shifts gracefully to the left. However, a second, rather low/small maximum seems to enter the scene from the right already at (i),(j). This is not expected since only $0.3 - 0.4\ \omega$ of ponderomotive energy have been added. Chances are that this small maximum is related to an odd channel closing, i.e., $n = 15$. However, comparing with the results in [37], the effect for even channel closings should appear slightly *below* the energy given by energy conservation alone. A systematic shift would be acceptable, so this is not the problem. But then, the odd channel closings are found to lie *exactly* at the predicted energies. This would mean a separation in energy *larger* than 1 ω between an even closing and a following one of higher order. This is obviously not the case. An explanation cannot be given.

As we continue with the right column of the plot, the structure seems to almost completely vanish. It is only in plot (q) of the right column that we again clearly identify a pronounced maximum. Compared to the starting point (f), U_p was raised by 1.1 ω up to this point. And indeed, the maximum is at quite the same position. Shifting to the left, it almost immediately washes out. A huge maximum seems to enter the scene from the right in (s) and (t), yet it does not form a pronounced shape when fully inside the plot. Also, the position of the maximum is shifted to the left compared to the expectation, since plot (z) at the bottom of the right column is exactly 2.0 ω away from our starting point (f). Hence we should see a maximum at the same position. This is not the case.

Obviously, the situation is not that easy: Energy conservation does somehow match the observation, but cannot fully explain what is found. Maxima exhibit different heights, appear shifted and/or washed out, relative separations do not match the energy conservation. However, one has to stress that the observation window was more or less arbitrarily positioned around the enhancement region within the re-scattering plateau

for each plot. This region changes shape quite significantly while raising the laser intensity. There is no prescription of how to exactly position the observation window to get the correct results.

3.3.4 Conclusions

Our calculations show that spectral enhancements observed at certain laser intensities in strong-field ionisation of atoms can also be found in strong-field ionisation of molecules. The vibrational motion of the nuclei in the cases of H_2 and D_2 can play the role of applying different laser intensities in the atomic case. Energy conservation serves as a simple explanation of the observed channel-closing effect, yet cannot completely determine at which laser intensity (or vibrational quantum number) it will take place. The difference between H_2 and D_2 is well explained by the different spacing of the vibrational levels. Furthermore, strong correlations between the nuclear motion and the kinetic energy of the ATI electrons are found. These correlations are revealed by the vibrational distributions of the ions for specific energy intervals of the ATI electrons. We have observed spectral enhancements despite the rather short pulse duration. It is expected that longer pulses will lead to even more pronounced effects. On the experimental side, to observe the predicted effect, coincidence measurements will be necessary. The distribution of vibrational states in the $H_2{}^+$ ion after strong-field ionisation of H_2 has been successfully measured already [49], but it still seems difficult to make such a measurement selectively for electrons of given kinetic energies.

3.4 Molecular Correlation

As was shown in the previous section, after photoionisation of H_2 oder D_2, photoelectron and ion are correlated with each other. In Section 2.7, a measure for the correlation between these two degrees of freedom,

$$K = \left[\operatorname{tr} \rho^2\right]^{-1}, \tag{3.22}$$

was introduced, with ρ being one of the two single-particle density matrices of the wave function. Basically, K expresses the number of significant terms in the product expansion of the wave function.

Of course, this measure can be applied to any wave function, and to parts of a wave function as well. Since application to a large area of the grid would simply give one number K, describing to total correlation between electron and ion, not much is learned. So far, we could observe a correlation between kinetic energy of the photoelectron and vibrational state of the ion. Since K will work for any matrix, it can of course also be applied to the momentum-space wave function. This seems more natural, since the electron momenta p_z correspond to the kinetic energy of the electron, and the vibrational states will still be well represented by their momentum distribution in p_R. The correlation K will be calculated for all values p_R within a small window of p_z, sliding over the complete momentum spectrum of the electron. This will yield a plot of "local correlation" (local in p_z) within the momentum space wave function. Of course, the window size is crucial, since it determines, how local the correlation is. As taking

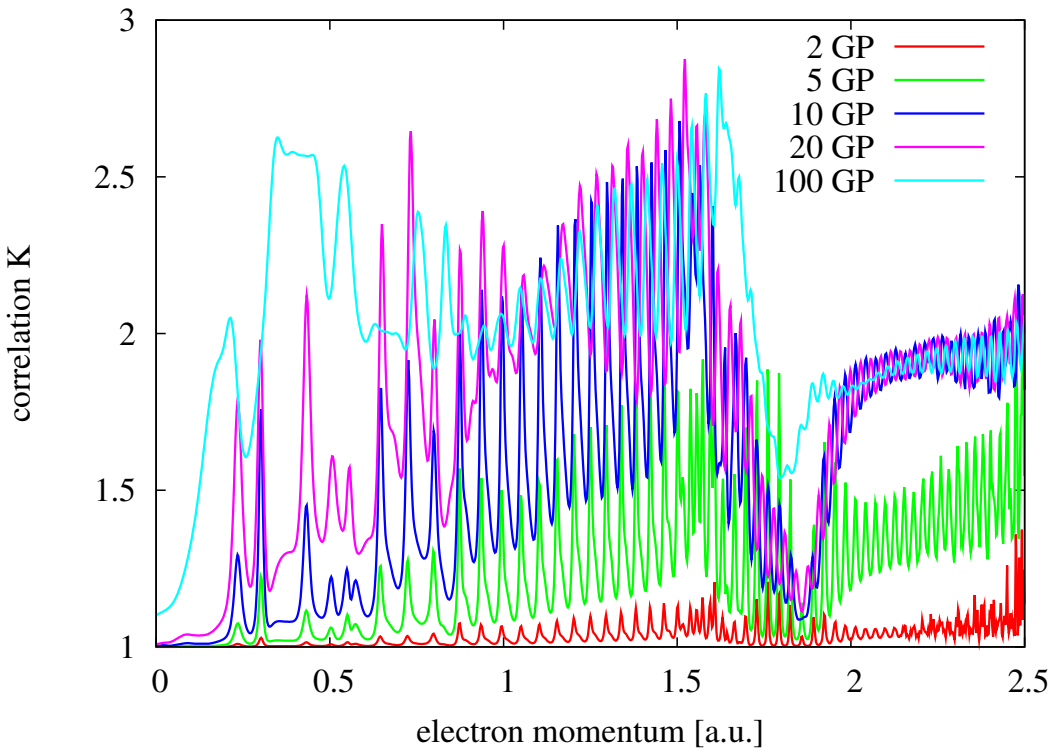

Figure 3.21: Correlation K between electronic and nuclear momentum for photoelectrons ($U_\mathrm{p} = 3.63\ \omega$) more than 30 a.u. away from the core. The plot shows different window sizes of the sliding window scanning along the electron momentum. The sizes are given in grid points within the plot.

the full spectrum as one big piece was found as not interesting, so would be a window size of one grid point. This would always give a K value of 1: There would be no matrix to decompose, hence there is but one "product of states", with the electronic state being simply the unit scalar. Fig. 3.21 shows a plot of K for different window sizes of 2, 5, 10, 20 and 100 grid points in width, where one grid point corresponds to about 10^{-3} a.u. of momentum. The plot was drawn such that the middle of the window gives the point of observation and the window was shifted by one grid point only in each step. The intensity in this case corresponds to $U_\mathrm{p} = 3.63\ \omega$. Obviously, the window size has influence on the plot, but still all curves share many features. The general trend is very similar for the plots of 10 and 20 grid points (and also up to 50, not shown here), and also the peak structure appears for all window sizes, however becoming less for the largest windows. The peak spacing corresponds to the photon energy. This is not surprising, since this structure is contained within the electron spectrum. The steep descent at about 1.8 a.u. is common for almost all window sizes as well. This will now be further investigated in comparing the change in correlation K with the course of the momentum spectrum. See Fig. 3.22 for four different laser intensities corresponding to $U_\mathrm{p} = 3.13\ \omega$, $3.93\ \omega$, $4.73\ \omega$ and $5.43\ \omega$. The K-plot is compared to the full momentum spectrum of the electron. The window size was fixed at ten grid points, since this seems to give the richest collection of features, i.e., clear peak structure and huge level changes. Is is clearly visible that in all four cases, the K rate drops at the end of each spectral hump. Low K does however not mean that the (momentum space) wave function contains only few vibrational states. It only means that it contains not many product terms in the expansion of canonical basis states within the scanning window. In the ideal case of a constant distribution of nuclear momenta within the scanning window, K would be unity. The same applies to the situation where for all nuclear momenta an identical distribution of electron momenta occurs. This is because in these two cases a product expansion would consist of only one term. K takes large values at those momenta where the ATI peaks reside, i.e., where (for high-order ATI) re-scattered electrons are responsible for the spectral yield. Since inelastic scattering between electron and ionic core should produce strong correlations between the two, it seems counter-intuitive why strong correlation should be found at ATI peaks, which correspond mainly to elastic scattering. Modulo this rapid oscillation following the ATI structure of the spectrum, there is a general trend of K rising steadily up to the end of the first big hump of the spectrum, dropping immediately afterwards. This drop repeats at every end of a spectral hump, after a short rise stretching out over the complete hump. Hence, correlation is always a bit larger within those clearly separated humps, corresponding to different re-scattering events. Up to now, not much more can be said about the meaning of this rise and fall of spectral correlation. However, it will be shown in the following chapter, that this fact finds its counterpart in a peculiar behaviour of the Wigner spectra investigated in the next chapter. If there is really a definite connection between these two findings remains up to now an open question.

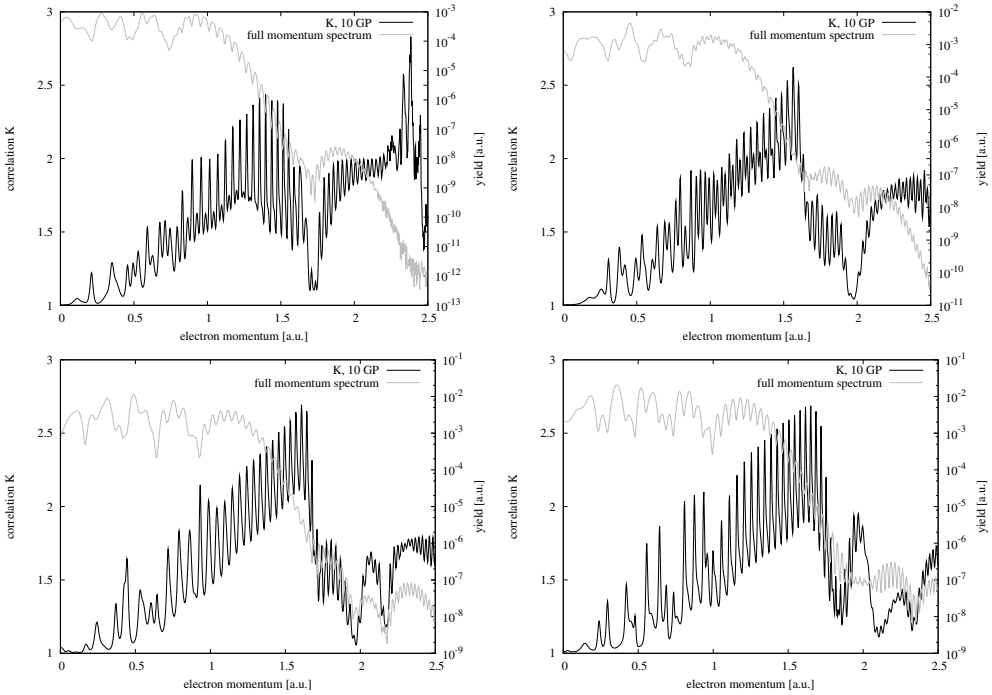

Figure 3.22: Comparison between correlation K of electronic and nuclear momentum (black) and the full electronic momentum spectrum (grey) of the ionised electron. The four plots show four different laser intensities corresponding to $U_\mathrm{p} = 3.13\ \omega$, $3.93\ \omega$, $4.73\ \omega$, and $5.43\ \omega$ from left to right, top to bottom.

Chapter 4

Coulomb Correction of Kinetic Energy Spectra

4.1 The Wigner Distribution Function (WDF)

In 1932, Eugene Paul Wigner introduced [53] his celebrated distribution function as an attempt to map a quantum state into the quantum-equivalent of classical phase space. It is defined as

$$W(x,p) := \frac{1}{\pi}\int_{-\infty}^{\infty} \psi^*(x+y)\psi(x-y)e^{2ipy}\mathrm{d}y. \tag{4.1}$$

This specific choice leads to the following properties:

1. it is real for all x and p,
2. integrated over p, it gives the probability distribution of x, and vice versa,
3. correct behavior under Galilei transformations,
4. correct behavior under time reversal,
5. transition probabilities can also be written as

$$\left|\int \psi^*(x)\phi(x)\mathrm{d}x\right|^2 = 2\pi\iint W_\psi(x,p)W_\phi(x,p)\mathrm{d}x\mathrm{d}p, \tag{4.2}$$

6. in the force-free case the equation of motion is the classical one.

In fact, Wigner showed that the average of an observable $\widehat{A}(\widehat{p},\widehat{q})$, quantum mechanically usually written as

$$\langle\widehat{A}\rangle = \mathrm{tr}(\widehat{A}\widehat{\rho}), \tag{4.3}$$

where $\widehat{\rho}$ is the density matrix operator, can also be written in an analogous way to classical physics as

$$\langle\widehat{A}\rangle = \int_{-\infty}^{\infty}\mathrm{d}q\int_{-\infty}^{\infty}\mathrm{d}p\ A(q,p)\widetilde{W}(q,p), \tag{4.4}$$

where $\widetilde{W}(q,p)$ is the most general WDF and given by

$$\widetilde{W}(q,p) = \frac{1}{\pi}\int_{-\infty}^{\infty} \langle q-y|\widehat{\rho}|q+y\rangle e^{2ipy}, \tag{4.5}$$

and $A(q,p)$ is the classical function corresponding to the operator $\widehat{A}(q,p)$. If the system is in a pure state, this expression reduces to Eq. (4.1). Still this is not the only form of $P(q,p)$ one could think of. Yet it is the only one fulfilling all properties listed above. This is also beautifully explained in his initial work cited above.

As a consequence of the Heisenberg uncertainty principle, it is of course not possible to exactly determine position and momentum of a quantum particle simultaneously. The WDF reflects this fact by its local negativity. Hence it is not exactly a probability distribution. However, it can be proven that if integrated over phase space volumes of the order of 1, it will always be non-negative.[1] This also holds for convolutions with a *smooth* kernel (in contrast to a step function) of the corresponding size. The most famous approach in this sense is due to Husimi [54], who smoothed the WDF with a Gaussian, for which $\Delta q \Delta p \geq 1/2$. This in fact leads to a non-negative distribution function. However, it does not have the last property 6 listed above.

4.2 Application: Spatially Resolved Electron Energy

Technically speaking, the WDF is the Fourier transform of the "autoconvolution" of the wave function,

$$W(x,\phi) = \int C_x(y) e^{i\phi y} \mathrm{d}y = \mathcal{F}[C](x,\phi), \tag{4.6}$$

with

$$C_x(y) = \psi^*(x+y)\psi(x-y), \tag{4.7}$$

projecting on $\phi = 2p$, being two times the momentum of x. It more or less reflects the properties of a local Fourier transform, i.e., one gets a spatially resolved momentum distribution. It is this fact that allows us to compensate for Coulomb defects within kinetic-energy spectra of photoelectrons: Simple Fourier analysis of a wave function partially residing in regions of non-constant negative potential always leads to a systematic over-estimation of kinetic energy. The electrons would still have to climb the hill until they finally reach a detector, losing energy on their way.

The simplest approach to overcome this situation is to propagate the wave function further on, up to times when most of the electrons are already at distances of almost vanishing Coulomb potential. Not only does this mean long propagation times, but it also forces the use of large grids, since the fast electrons already far out of the Coulomb well still propagate further into the continuum and might get lost if reaching the grid boundary.

Since the Coulomb potential as a function of x is known, it is possible to correct momentum contributions according to their position in space by letting

$$E_{\mathrm{kin}} \rightsquigarrow E_{\mathrm{kin}} + V(x), \quad \text{or,} \quad p \rightsquigarrow \sqrt{p^2 + 2V(x)}. \tag{4.8}$$

[1] In general, it has to be of the order of $\hbar^f$, f being the number of degrees of freedom of the system.

For each electron position x, the Wigner function $W(x,p)$ is calculated. Each time, all kinetic momenta are corrected according to the prescription above, adding the x-dependent Coulomb term. In summing all contributions belonging to the same effective momentum, the coordinate x is integrated out. This integration is a non-coherent summation and therefore in principle an approximation. This should be kept in mind, although the results look very reasonable and meet the expectations.

With this we take into account that the electron will lose "all" its remaining Coulomb energy $V(x)$ before hitting a real-world detector. This gives us the opportunity of calculating kinetic-energy spectra very early, although this means that a significant portion of the wave function still resides in regions of non-negligible Coulomb potential. There is still a problem connected with early momentum measurements, which will be addressed later.

4.3 Numerical Implementation

The most efficient way of computing the WDF numerically is via the Fast Fourier Transform (FFT). Hence, for each space coordinate x, the autocorrelation function $C_x(y)$ is computed for all relative shifts y. Then, an FFT algorithm is applied to compute the Wigner Distribution Function at position x. This is repeated for all coordinates x. However, there are two slight caveats:

1. Obviously, the Fourier transform contained in the definition of the WDF, see Eq. (4.1), projects on the momentum state with twice the momentum p. This has to be taken care of when plotting the data. However, no information is lost, since the discrete correlation function $C_x(y)$ is computed over all possible relative shifts of ψ with respect to itself, positive and negative. This means double array length of $C_x(y)$ as compared to ψ and thus double momentum resolution.

2. Due to the fact that the Fourier transform contained in Eq. (4.1) is executed with respect to y, reaching from negative to positive relative shifts of up to full array length, the transformation array $C_x(y)$ does not start at $y = 0$, but is symmetrically extended around $y = 0$ as the centre coordinate, i.e., $y \in [-y_0, y_0]$. Therefore, each Fourier component will gather a phase $\exp(iy_0\phi)$ that will have to be compensated for before further applications of the WDF can be carried out. See Fig. 4.1 for a sketch: The FFT routine assumes zero phases (and hence $y = 0$) at the beginning of the array. And this is how it projects the arrays onto exponentials. A shift in one domain always leads to a phase factor in the other domain. This is an intrinsic property of the Fourier transformation:

$$\begin{aligned}
\mathcal{F}[f(x+\mathrm{d}x)](p) &= \int f(x+\mathrm{d}x)\exp(-ipx)\mathrm{d}x \\
&= \int f(y)\exp[-ip(y-\mathrm{d}x)]\mathrm{d}y \\
&= \exp(ip\mathrm{d}x)\int f(y)\exp(-ipy)\mathrm{d}y \\
&= \mathcal{F}[f(x)](p)\ \exp(ip\mathrm{d}x).
\end{aligned} \tag{4.9}$$

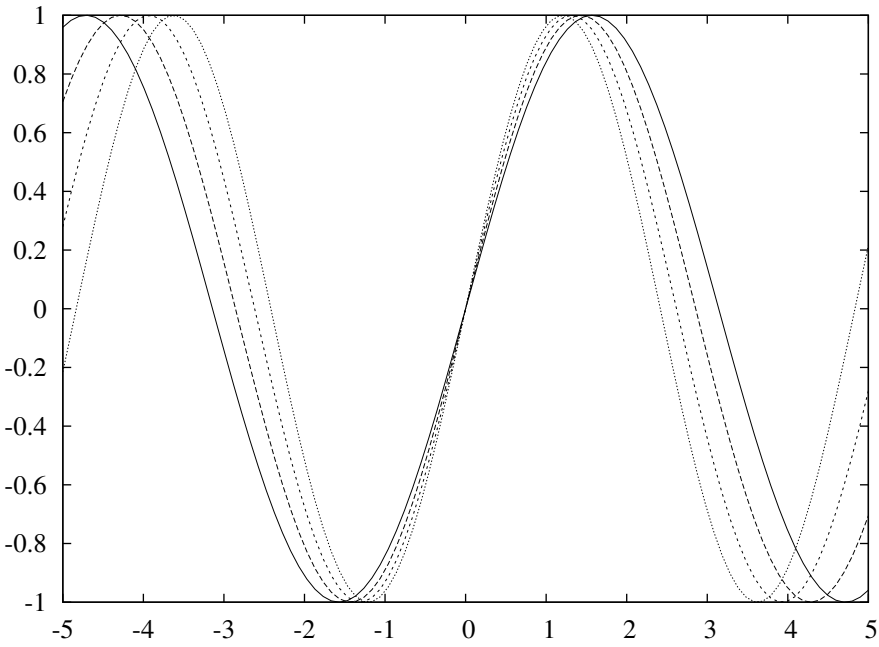

Figure 4.1: Sinusoidal waves coinciding at zero will gather a relative phase on their way. Assuming zero relative phase at the beginning of a computational array, the FFT is able so assign a position in space to the function being analysed in frequencies. If the array does not start at zero coordinate, the Fourier components will carry a phase which has to be corrected.

If smoothing the WDF is considered, one should not underestimate the computational effort and memory requirements for this procedure! Since a numerically feasible convolution is only possible via application of the Convolution Theorem, i.e., via multiplication in reciprocal space instead of convolving function and kernel explicitly, it is necessary to store the full WDF in memory. Depending on the grid sizes necessary to collect all interesting data at once, a huge amount of memory might be required. If computational time does not play a role, it is of course possible to store only a slab of the WDF in memory extending over the spacial width of the convolution kernel. The convolution has then to be executed explicitly.

4.4 Results

In Fig. 4.2, low-kinetic-energy spectra of ATI electrons for the 1D hydrogen atom described by the hamiltonian (3.15) are shown. The laser intensity corresponds to $U_\mathrm{p} = 3.63\ \omega$ and the pulse length was 9 optical cycles. The pulse shape corresponds to that utilised for the molecular calculations, i.e., it shows a 1.5-cycles $\sin^2$-shaped ramp at the beginning and at the end.

The upper panel presents spectra calculated via simple Fourier transform, the lower panel shows Coulomb corrected Wigner spectra. The different curves correspond to different observation times after the laser pulse, going from zero to ten optical cycles,

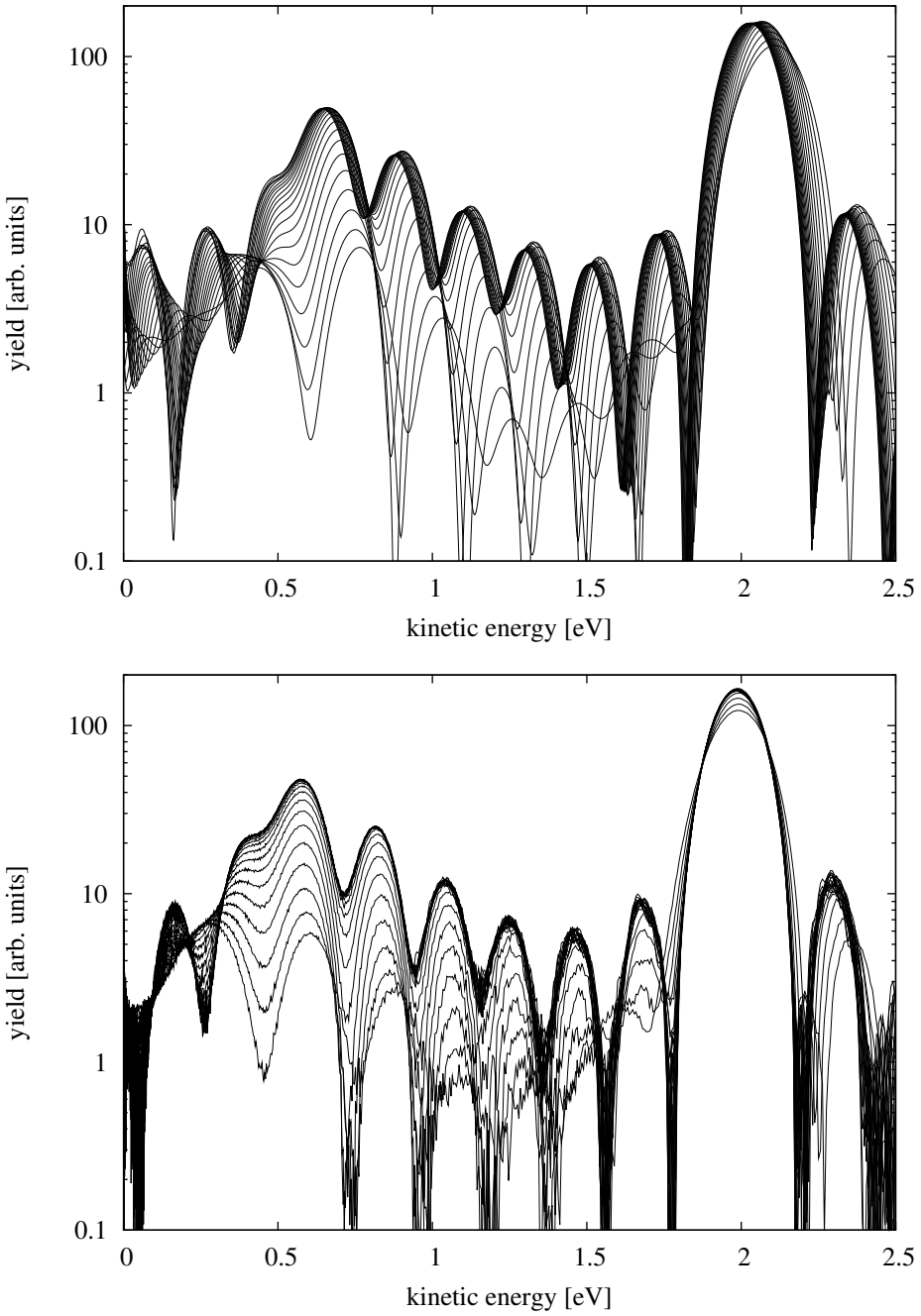

Figure 4.2: Kinetic-energy spectra of (right-going) ATI electrons in the case of the 1D hydrogen atom for a laser intensity corresponding to $U_\mathrm{p} = 3.63\ \omega$. The spectra have been calculated via Fourier transform (upper panel) and Wigner Distribution Function plus Coulomb correction (lower panel) and correspond to electrons between 30 and 5500 a.u. away from the core. Plots are shown for observation times between zero and ten optical cycles after the laser pulse, in multiples of half-cycles (from bottom up).

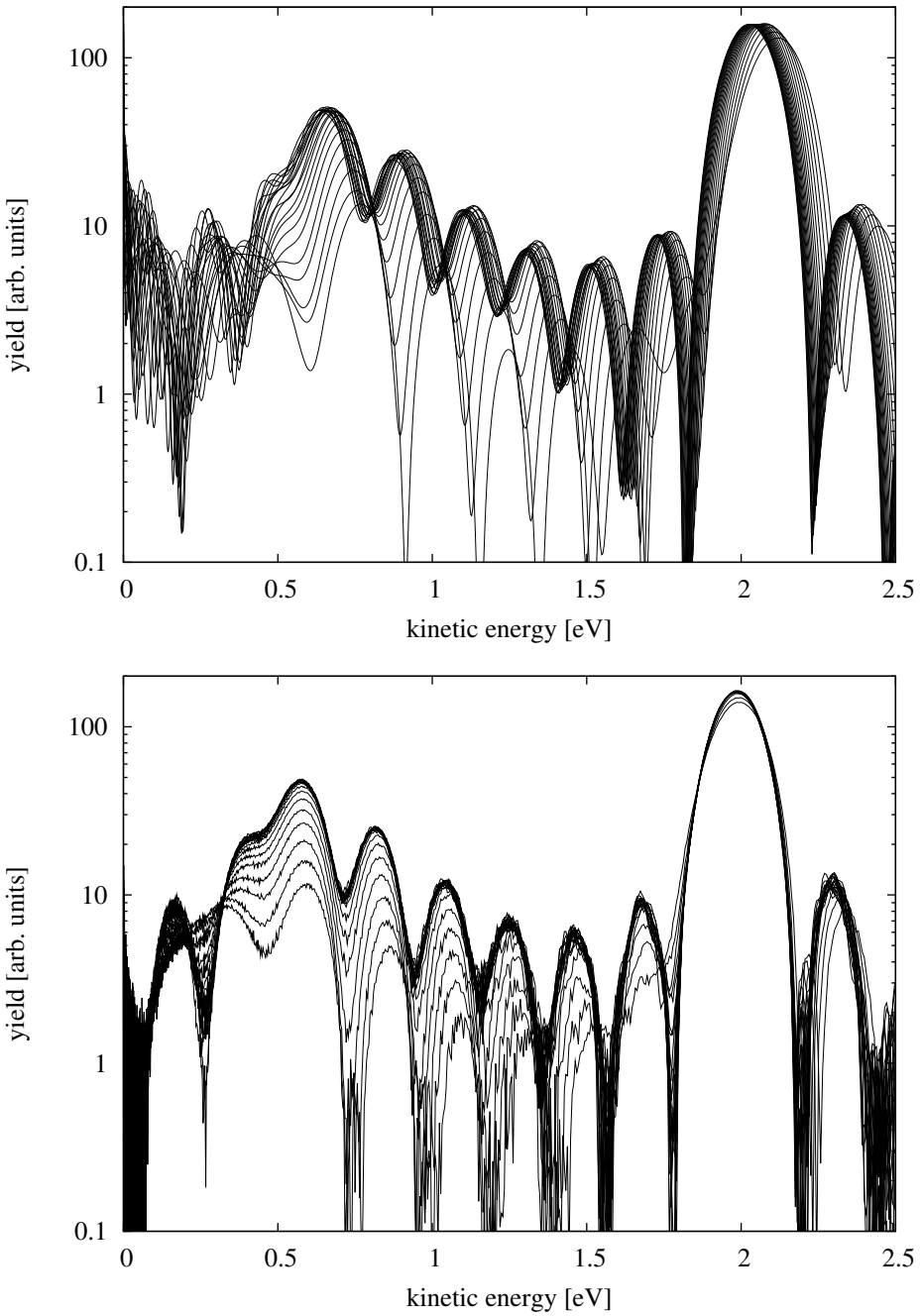

Figure 4.3: Same as Fig. 4.2 for an observation interval from 0 to 5500 a.u.

in multiples of half-cycles. In both cases, one clearly sees how all peaks grow, i.e., more electrons enter the observation area with time. But in the case of the Fourier spectra, the peaks additionally shift to lower energies, because while moving outwards, the electrons lose Coulomb energy. This shift is strongest for electrons with low energy, corresponding to the fact that they mainly reside close to the nucleus. With increasing time, the peaks seem to converge towards a somewhat final position and height. Yet they still contain lots of Coulomb energy they did not get rid of within the time of observation.

This is contrasted by the Wigner spectra, that take the Coulomb energy of the electrons into account and therefore show peaks of constant position over time. As in the case of the Fourier spectra, the peaks grow due to additional electrons entering the scene. Convergence is obvious as well, but slightly faster for the very low-energy peaks and much faster for the main 2 eV-ATI peak. As a feature, it is very obvious that the position of the Fourier peaks is by far off the correct energy, which is found for the Wigner peaks. Even the first strong ATI peak at around 2 eV should lie below 2 eV but is found slightly above 2 eV in the Fourier case even ten optical cycles after the end of the laser pulse. Of course, this effect vanishes rapidly for peaks of higher order, since the corresponding electrons are much faster and therefore will reach low Coulomb potential much earlier, which has been confirmed and can be seen in Fig. 4.4 for spectra taken immediately after the end of the laser pulse.

As was expected, it is possible to calculate kinetic energy spectra of photoelectrons far earlier (in terms of propagation time) than is the case for simple Fourier transformation if the WDF method is applied. Also, the result is far more accurate for regions of space where the Coulomb potential is significantly non-vanishing. Since usually in this area mostly slow electrons are found, a clear shift of the lowest few ATI peaks can be identified when comparing both methods. However, due to the fact that electrons very close at the nuclear core behave much more according to their quantum nature as those already far away from the centre of force, the WDF acquires negative values within this region of phase space. When adding up all the momentum components of the spatially resolved and Coulomb-corrected spectra, this "interference" appears as a zig-zag on top of otherwise smooth energy spectral curves. Since this is not desirable and also the whole technique does not make sense under these circumstances, one should restrict oneself to regions of space where the electrons are clearly ionised already and far enough away from the core to behave more or less like a classically moving charge.

When doing this, one will encounter another problem connected to propagation time: In our example, we chose 30 a.u. as the beginning of the area of examination. All electrons still closer at the nuclear core, but with energies high enough to escape into the continuum, will eventually enter the examination region with time, as was mentioned above. This can be seen in Fig. 4.3, where the same plots as in Fig. 4.2 are shown, but for electron distances between 0 and 5500 a.u., i.e., taking also electrons into account that reside between 0 and 30 a.u. away from the core. Obviously, the peaks are higher already for the earliest curves and also they converge faster. But as a payoff, the distortion is stronger due to more contributions from electrons extremely close to the nuclei. Therefore, if the lowest few ATI peaks within the spectrum are of interest for a certain observation, one has to check convergence of the peaks in question before stopping the simulation. However, already from very low ATI orders on, the

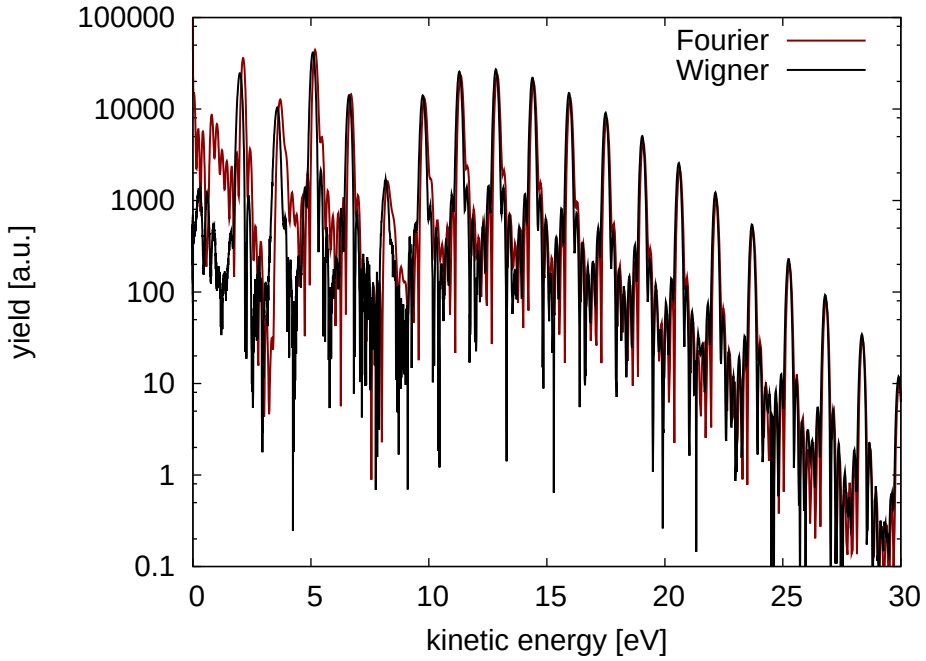

Figure 4.4: Kinetic-energy spectra of (right-going) ATI electrons in the case of the 1D hydrogen atom for a laser intensity corresponding to $U_\mathrm{p} = 3.63\ \omega$. The spectra have been calculated via Fourier transform (grey) and Wigner Distribution Function plus Coulomb correction (black) and correspond to electrons between 30 and 5500 a.u. away from the core. Plots are shown for an observation time directly after the laser pulse.

peaks converge rapidly.

In Fig. 4.5, the energy range around the re-scattering plateau is shown for four different observation times of zero, two, four and six optical cycles after end of the laser pulse. Again we compare the Fourier spectra (upper panel) with the Coulomb-corrected Wigner spectra (lower panel). In the right two thirds of the plot, the big hump of the re-scattering plateau that was investigated in the previous chapter is identified. It is exactly in front of this big hump that the Wigner spectra behave unfortunate. They show strong distortions of fast oscillations similar to the distortions close to the very low energy peaks. As they vanish with time, it might be that they have in fact the same origin and are Wigner artifacts resulting from non-classical particle motion. There might be a connection to the findings of the strong drop of correlation of electrons and nuclei within this energy region. The correlation is low also at the very beginning of the spectrum, where the WDF shows the same behaviour.

To summarise, the method of Coulomb-correcting kinetic-energy spectra applying the WDF yields accurate spectra at early times at the cost of higher computational effort as compared to simple Fourier analysis. Since for low-energy peaks, usually involving electrons close at the core and thus being significantly Coulomb-shifted, the Fourier-method makes large errors and over-estimates electron momenta, the WDF method should be the only method applied to obtain trustworthy results. For high-order ATI, the Coulomb potential usually does not play a role and the Fourier method can safely be applied, which is much faster in computation and also does not show artifacts close to the re-scattering plateau.

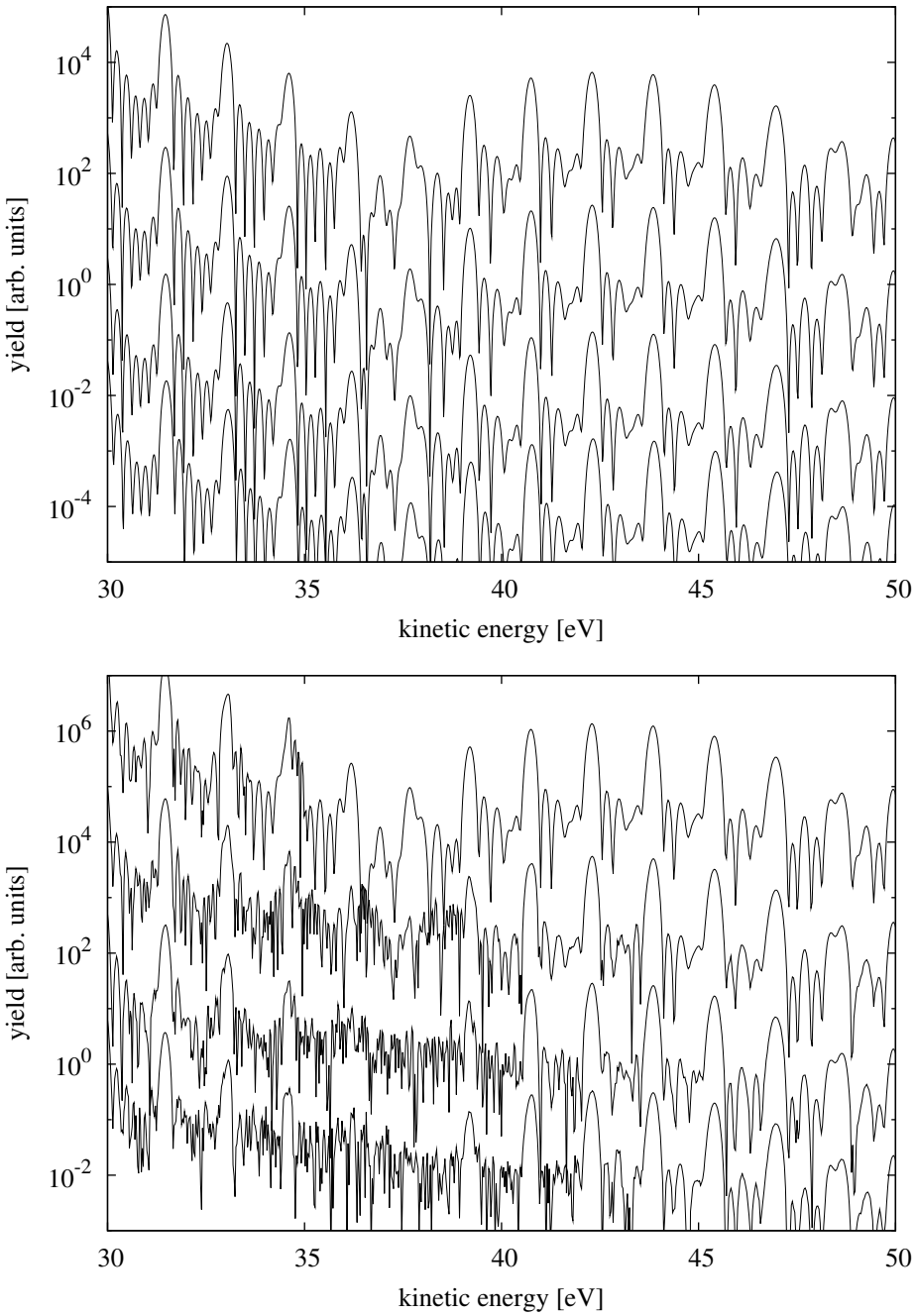

Figure 4.5: Kinetic-energy spectra of (right-going) ATI electrons in the case of the 1D hydrogen atom for a laser intensity corresponding to $U_\mathrm{p} = 3.63\ \omega$. The spectra have been calculated via Fourier transform (upper panel) and Wigner Distribution Function plus Coulomb correction (lower panel) and correspond to electrons between 30 and 5500 a.u. away from the core. Plots are shown for observation times of zero, two, four and six optical cycles after the laser pulse from bottom to top.

Appendix A

Numerical Data in Detail

A.1 Laser Intensitiy and Ponderomotive Potential

The following table gives a conversion between laser intensity in 10^{14} W/cm^2 and ponderomotive energy in units of $\omega = 0.0569542$ a.u., corresponding to a laser wavelength of $\lambda = 800$nm.

U_p/ω	3.13	3.23	3.33	3.43	3.53	3.63
Int./(10^{14} W/cm^2)	0.8132	0.8392	0.8653	0.8914	0.9174	0.9435
U_p/ω	3.73	3.83	3.93	4.03	4.13	4.23
Int./(10^{14} W/cm^2)	0.9696	0.9957	1.0213	1.0474	1.0710	1.0998
U_p/ω	4.33	4.43	4.53	4.63	4.73	4.83
Int./(10^{14} W/cm^2)	1.1240	1.1518	1.1780	1.2038	1.2298	1.2558
U_p/ω	4.93	5.03	5.13	5.23	5.33	5.43
Int./(10^{14} W/cm^2)	1.2818	1.3079	1.3338	1.3598	1.3858	1.4118
U_p/ω	5.53	5.63				
Int./(10^{14} W/cm^2)	1.4379	1.4638				

A.2 Vibrational Energies of H_2^+ and D_2^+

The following tables give the vibrational energies obtained via the calculation of the different vibrational states of H_2^+ and D_2^+, respectively. The ground-state energies of the model H_2 and D_2 systems are

$$E_0^{H_2} = -1.1645 \text{ a.u.}, \qquad E_0^{D_2} = -1.1674 \text{ a.u.},$$

the ionisation potentials of both systems amount to

$$I_\mathrm{p}^{H_2} = -0.5671 \text{ a.u.}, \qquad I_\mathrm{p}^{D_2} = -0.5685 \text{ a.u..}$$

H_2^+						
v	E_v (a.u.)	ΔE^v (ω)	ΔE^v (a.u.)	ΔE (a.u.)	ΔE (ω)	$U_\mathrm{p}/\omega = 14 - (I_\mathrm{p} + \Delta E^v)/\omega$
0	-0.5974	0.0000	0.0000			4.00
1	-0.5874	0.1751	0.0100	0.00998	0.1751	3.82
2	-0.5780	0.3402	0.0194	0.00941	0.1651	3.66
3	-0.5692	0.4956	0.0282	0.00886	0.1554	3.50
4	-0.5608	0.6414	0.0366	0.00831	0.1459	3.36
5	-0.5531	0.7779	0.0443	0.00778	0.1365	3.22
6	-0.5458	0.9051	0.0516	0.00725	0.1272	3.09
7	-0.5391	1.0232	0.0583	0.00673	0.1181	2.98
8	-0.5329	1.1323	0.0645	0.00622	0.1091	2.87
9	-0.5271	1.2325	0.0703	0.00571	0.1002	2.77

D_2^+						
v	E_v (a.u.)	ΔE^v (ω)	ΔE^v (a.u.)	ΔE (a.u.)	ΔE (ω)	$U_\mathrm{p}/\omega = 14 - (I_\mathrm{p} + \Delta E^v)/\omega$
0	-0.5989	0.0000	0.0000			4.00
1	-0.5917	0.1259	0.0072	0.00718	0.1259	3.87
2	-0.5849	0.2468	0.0141	0.00689	0.1208	3.75
3	-0.5782	0.3627	0.0207	0.00661	0.1159	3.64
4	-0.5719	0.4738	0.0270	0.00634	0.1112	3.53
5	-0.5659	0.5802	0.0331	0.00606	0.1063	3.42
6	-0.5601	0.6817	0.0389	0.00579	0.1016	3.32
7	-0.5545	0.7786	0.0444	0.00552	0.0968	3.22
8	-0.5493	0.8707	0.0496	0.00525	0.0921	3.13
9	-0.5443	0.9583	0.0546	0.00499	0.0876	3.04

Table A.1: H_2^+ (upper table) and D_2^+ (lower table): Vibrational energies for $v = 0, \ldots 9$, offset to E_0, offset to next-higher energy, and predicted channel closings. Here, ω is the laser frequency corresponding to 800 nm wavelength. For the channel closings, a photon number of $n = 14$ has been assumed in order to obtain the channel-closing intensities around $10^{14}\,\mathrm{W/cm^2}$ ($U_\mathrm{p} = 3.85\,\omega$).

Bibliography

[1] S. Pieper and M. Lein, Phys. Rev. A **77**, 041403(R) (2008).

[2] S. Pieper and M. Lein, J. Mod. Opt. **55**, 2631 (2008).

[3] Wikipedia, Born-Oppenheimer Approximation — Wikipedia, The Free Encyclopedia, 2007, [Online; accessed 21-February-2007].

[4] F. Seyl, Ph.D. thesis, Georg-August-Universität Göttingen, 1996.

[5] P. Ehrenfest, Ann. d. Physik **356**, 327 (1916).

[6] P. Bucksbaum, A. Zavriyev, H. Muller, and D. Schumacher, Phys. Rev. Lett. **64**, 1883 (1990).

[7] G. Jolicard and O. Atabek, Phys. Rev. A **46**, 5845 (1992).

[8] A. D. Bandrauk and M. L. Sink, J. Chem. Phys. **74**, 1110 (1981).

[9] Y. B. Zel'dovich, Sov. Phys. JETP **24**, 1006 (1967).

[10] H. P. Breuer and M. Holthaus, Z. Phys. D **11**, 1 (1989).

[11] A. Bandrauk and H. Shen, Chem. Phys. Lett. **176**, 428 (1991).

[12] P.-O. Löwdin, Phys. Rev. **97**, 1474 (1955).

[13] H. Everett, Rev. Mod. Phys. **29**, 454 (1957).

[14] R. Paskauskas and L. You, Phys. Rev. A **64**, 042310 (2001).

[15] R. Grobe, S. L. Haan, and J. H. Eberly, Comp. Phys. Comm. **117**, 200 (1999).

[16] L. V. Keldysh, Sov. Phys. JETP **20**, 1307 (1965).

[17] V. S. Popov, Phys. Usp. **47**, 885 (2004).

[18] P. Agostini *et al.*, Phys. Rev. Lett. **42**, 1127 (1979).

[19] J. H. Eberly, J. Javanainen, and K. Rzążewski, Phys. Rep. **204**, 331 (1991).

[20] W. Becker *et al.*, Adv. At. Mol. Opt. Phys. **48**, 35 (2002).

[21] A. Perelmov, V. Popov, and M. Tetent'ev, Sov. Phys. JETP **23**, 924 (1966).

[22] A. Perelmov, V. Popov, and M. Tetent'ev, Sov. Phys. JETP **24**, 207 (1966).

[23] F. Faisal, J. Phys. B **6**, L89 (1973).

[24] H. Reiss, Phys. Rev. A **22**, 1786 (1980).

[25] G. G. Paulus *et al.*, Phys. Rev. Lett. **72**, 2851 (1994).

[26] G. G. Paulus, W. Becker, W. Nicklich, and H. Walther, J. Phys. B **27**, L703 (1994).

[27] G. G. Paulus, W. Becker, and H. Walther, Phys. Rev. A **52**, 4043 (1995).

[28] P. Corkum, Phys. Rev. Lett. **71**, 1994 (1993).

[29] F. Grasbon *et al.*, Phys. Rev. Lett. **91**, 173003 (2003).

[30] N. Kylstra *et al.*, Phys. Rev. Lett. **85**, 1835 (2000).

[31] R. Fischer, M. Lein, and C. H. Keitel, J. Mod. Opt. **54**, 1911 (2007).

[32] P. Hansch, M. A. Walker, and L. D. Van Woerkom, Phys. Rev. A **55**, R2535 (1997).

[33] H. G. Muller and F. C. Kooiman, Phys. Rev. Lett. **81**, 1207 (1998).

[34] H. G. Muller, Phys. Rev. A **60**, 1341 (1999).

[35] R. Kopold and W. Becker, J. Phys. B **32**, L419 (1999).

[36] R. Kopold, W. Becker, and M. Kleber, Opt. Commun. **179**, 39 (2000).

[37] D. B. Milošević *et al.*, Phys. Rev. A **76**, 053410 (2007).

[38] G. G. Paulus *et al.*, Phys. Rev. A **64**, 021401(R) (2001).

[39] R. Kopold, W. Becker, M. Kleber, and G. G. Paulus, J. Phys. B **35**, 217 (2002).

[40] E. P. Wigner, Phys. Rev. **73**, 1002 (1948).

[41] L. D. Landau and M. Lifshitz, *Quantum Mechanics* (Pergamon Press, Oxford, 1977), sec. 147.

[42] F. H. M. Faisal and P. Scanzano, Phys. Rev. Lett. **68**, 2909 (1992).

[43] K. Krajewska, I. I. Fabrikant, and A. F. Starace, Phys. Rev. A **74**, 053407 (2006).

[44] N. L. Manakov and M. V. Frolov, JETP Lett. **83**, 536 (2006).

[45] J. Wassaf, V. Véniard, R. Taïeb, and A. Maquet, Phys. Rev. Lett. **90**, 013003 (2003).

[46] M. P. Hertlein, P. H. Bucksbaum, and H. G. Muller, J. Phys. B **30**, L197 (1997).

[47] M. J. Nandor, M. A. Walker, L. D. Van Woerkom, and H. G. Muller, Phys. Rev. A **60**, R1771 (1999).

[48] E. Cormier *et al.*, J. Phys. B **34**, L9 (2000).

[49] X. Urbain *et al.*, Phys. Rev. Lett. **92**, 163004 (2004).

[50] K. Mishima, K. Nagaya, M. Hayashi, and S. Lin, Phys. Rev. A **70**, 063414 (2004).

[51] W. Kołos, K. Szalewicz, and H. J. Monkhorst, J. Chem. Phys. **84**, 3278 (1985).

[52] B. Feuerstein and U. Thumm, Phys. Rev. A **67**, 043405 (2003).

[53] E. Wigner, Phys. Rev. **40**, 749 (1932).

[54] K. Husimi, Proc. Phys. Math. Soc. Japan **22**, 264 (1940).

Erklärung

Hiermit versichere ich, dass ich die vorliegende Dissertation selbständig und ohne unerlaubte Hilfe angefertigt und andere als die in der Dissertation angegebenen Hilfsmittel nicht benutzt habe. Alle Stellen, die wörtlich oder sinngemäß aus veröffentlichten oder unveröffentlichten Schriften entnommen sind, habe ich als solche kenntlich gemacht. Kein Teil dieser Arbeit ist in einem anderen Promotions- oder Habilitationsverfahren verwendet worden.

Stefan Pieper